

BOSTON UNIVERSITY GENEVA  
PHYSICS PROGRAM

CERN INTERNSHIPS  
2014

---

COLLECTION OF THE FINAL PAPERS



---

**FORWARD****BY AUGUSTO CECCUCCI**

---

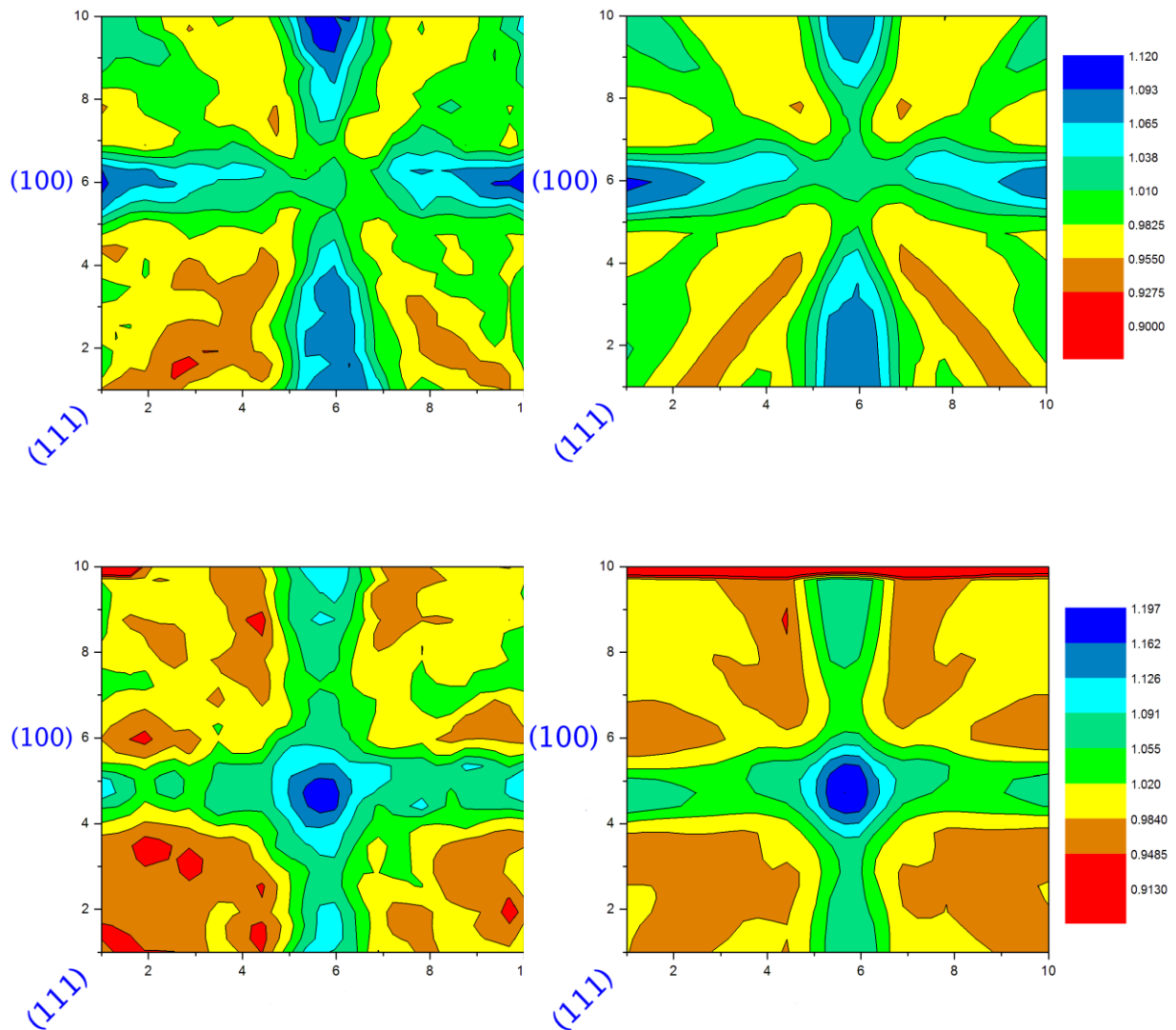
Fifteen very bright and motivated undergraduate students spent a semester in Geneva attending the Boston University Geneva Physics Program. They attended classes at Geneva University and had the opportunity to do a research internship at CERN. The students have summarized their results in the final papers collected in this booklet. Subjects spanned from Particle to Atomic Physics, tools included a broad range of instruments, from hardware setup to analysis frameworks. All students showed relentless enthusiasm and it is a great pleasure to present their work here.





# Emission Channeling: Lattice Impurity Location and Evolution in 3C-SiC

By Nick Charron



Material sciences exist at the forefront of technology in the modern world. As innovators and engineers strive to maximize efficiency, increase outputs, and reduce costs, scientists and technicians must hunt for materials to meet ever growing technological standards. Above all, it is important to understand the fundamental properties of new materials, and to weigh the costs and benefits of their applications in the real world. With the help of solid-state physics and crystalline analysis, researchers can investigate the characteristics of novel materials.

Among the many different properties of crystal lattices, it is often important to understand how foreign atoms and impurities behave in the lattice. This includes their stable sites of residence, evolution with temperature changes, and their effect on the material's emergent properties (conductivity, magnetization, dielectric properties, etc.). After all, it is well known that a simple doping of certain materials with impurity atoms drastically changes the conductivity of the material (a fact to which we owe all of modern electronics). There are many ways of measuring the behavior of impurities in a lattice. However, the effect of *Channeling* offers solid-state physicists a new and sensitive technique for measurements.

Johannes Stark initially discovered channeling in the early 20th century, but the popularity and excitement of wave mechanics coupled with the results of Bragg and other defining quantum experimentalists largely overshadowed the effect. The effect, in its simplest form, describes the propagation of charged particles through a

crystal lattice; namely, charged particles, when electromagnetically guided by the ionic potential of the lattice, will propagate almost unhindered along certain symmetrical crystal directions but will be blocked almost completely along other directions. The former phenomenon is called *channeling*, while the latter is known as *blocking*. The first of the experiments in the 1960's (during the so called "rebirth of channeling") to explore the effect employed a technique known as ion beam channeling, in which a beam of charged particles is fired at a crystal target at varying angles to determine the directions of channeling and blocking. Some time after these experiments, the technique of emission channeling became popular in the analysis of crystal structure and material sciences, especially with sensitive  $\beta$ -emission experiments. The same physical effect is used, but instead of directly channeling ions through the lattice, an ion implantation technique is used: the lattice can be impregnated with radioactive atoms, who will decay and emit radiation that will be either channeled or blocked as it leaves the impurity site. In this way, one can gather an emission pattern using a position-sensitive electron/alpha pad detector and an angular scan of the crystal sample along different orientations.

The benefit of using emission channeling is that each dopant site generates a unique emission pattern based on its location in the lattice and the fraction of the dopant atoms that occupy it.. In addition, emission channeling requires a much lower fluence of ions, which helps to minimize implantation damage and allows for sensitive measurements for large background sensitive  $\beta$ -emission experiments. By examining a doped sample at different temperatures, one can develop a mechanism

that describes the impurity fraction and location evolution as a function of temperature.

While at CERN I was tasked with the analysis of emission channeling patterns for face-centered cubic silicon carbide (3C-SiC). This material has many promising applications as a wide band gap semiconductor (2.36 eV); a consequence of its structural integrity at high operating temperatures. For example, Silicon carbide logic circuits have been shown to operate well near 550° C, which is a significant improvement over normal silicon circuits that break down around 350° C. Such benefits allow engineers to simplify schematics, eliminate cumbersome cooling apparatuses, and achieve an overall compact design. Yet, it is very important to know how foreign impurities behave in the lattice: It is well known that certain impurities (metals in particular) in wide-gap semiconductors can create “deep-level traps” in the band gap that negatively affect conductivity.

In order to explore the behavior of these impurities CERN’s ISOLDE facility used emission channeling to study 3C-SiC doped with radioactive iron ( $^{59}\text{Fe}$ , beta decay,  $\lambda=44.5$  d). Using the on-line beam setup at ISOLDE, the emission channeling team employed a series of *annealings* (heating followed by cooling for measurements) from room temperature up to 900 °C. A silicon pad detector was used to pick up the angular distribution of emitted electrons and generate a two-dimensional experimental emission pattern (pictured on the cover). By comparing each experimental emission pattern with a library of ideal emission patterns from Monte-Carlo simulations, I could determine the best fit for 1-site, 2-site, and 3-site occupations. By comparing the fits from different temperatures, I could track the

evolution of occupation fractions and displacements from ideal sites for the iron atoms. According to research done in the past few years by emission channeling experiments at the ISOLDE laboratory, the four mostly likely sites of impurity occupation were found to be the *substitutional* silicon and carbon sites (SA and SB respectively), where a dopant atom takes the place of a lattice atom, and the *interstitial* silicon and carbon sites (TA and TB respectively), where a dopant atom exists between the rows of the lattice elements. It was determined in 2013 that the SA and TB positions gave the highest fractional occupations using two-site fits, but the sum of these fractions did not add up to the total fraction of all substitutional and interstitial fractions combined ( $SA + SB + TA + TB$ ). This implied there was a *third* site, either TA or SB, that the dopants were occupying; therefore, my job was to carry out the necessary third site fits, examining both TA and SB, for all directions and temperatures.

After months of analysis, and upon the consideration of several theoretical models, my coworker and I were able to draw some conclusions: First, the signal of the third site is weaker compared to the first two, meaning it has a lower fractional occupation. This low fraction was seen at nearly all temperatures, even where we expected to see the occupation rise. Therefore, the choice of TA over SB, or vice versa, had no real effect on the visual “accuracy” of our fits; that is, the picture given by the two-site fits from 2013 would appear to have only little differences between the visual pattern produced by a three-site fit. Second, we would expect only SB as a third site at higher temperatures. This is because there is a high thermal energy barrier that the dopants have to overcome in order to settle in the SB sites, yet they

tend to remain in such positions because they are very stable. Finally, we saw that both SA and SB sites move closer to their ideal theoretical positions as temperature increases, while TB and TA tend to disperse.

Under these observations, we decided that the third site was mostly likely SB, given its energy restrictions and the lack of any “transition temperature” which would have shown a clear jump from TA to SB sites. When comparing fractions from multiple directions, the numbers must add up; for example, if we see a total substitutional and interstitial fraction along the  $\langle 111 \rangle$  crystal direction of 50%, then the fractions from our three site fits should add up to 50% (with an acceptable amount of error). When we did such comparisons, we found that our three-site model (SA, TB, and SB) matched the total fractions quite well for multiple directions. Our observation that the substitutional impurities (SA and SB) moved closer to their ideal sites as temperature increased should be well supported by molecular energy and stability considerations. Because of such results, we can conclude that a three-site occupation of SA, TB, and SB offers a possible description on iron impurities in the 3C-SiC lattice.

The analysis was both extensive and eliminative, as there were many possible sites for the impurity atoms to occupy. In addition, by nature of the cubic lattice, there existed several symmetries along certain directions. It was necessary to check every direction and eliminate all but two for the results of the three site fits. This was a daunting task, as the three-site fits take *much* more time than the two-site fits. The results were often very difficult to resolve, especially along certain critical directions, because the signal of our third site was so low and the lattice can

appear more “crowded”. Only after careful averaging and comparison were we able to make some sense of the three-site fits.

Upon reflection of my time here at CERN, I have learned many important skills and ideas. First, I have learned the importance of large scale data preservation and organization: with sometimes up to 52,000 separate fits per temperature, for nine temperatures and four different directions, it became crucial to keep neat and organized records of progress. Second, I have gained valuable understanding in what it’s like to do experimental research. The process is never quick nor easy, and the results are not always what one wants to see. Yet, it becomes important to accept your research and try to make sense of results using physical intuition and an objective view. Lastly, I can now truly appreciate the value of teamwork and progress. The many scientists at CERN – Long time PhDs, graduate students, or undergraduates like myself – must work together in a collaborative and supportive way to produce results and expand the frontiers of science. While the greatest scientific discoveries and achievements of the past century are usually attributable to a single face or name, none of these achievements would have been possible without the collaborative efforts of scientists around the world. I have certainly enjoyed my stay at CERN, and I can now walk on toward my next endeavors with the confidence I have gained.





# Study for a high precision measurement of the difference of $B_s^0$ and $B^0$ lifetimes

Undergraduate Research Project  
Boston University Geneva Physics Program

Supervised by:  
Dr. Diego Tonelli  
Dr. Angelo Di Canto

Julia Cline  
Julia.R.Cline@williams.edu

June 30, 2014

Our goal is to measure the difference in lifetimes of the  $B^0$  and  $B_s^0$  mesons. We use simulations of two semileptonic decays into common final states,  $B^0 \rightarrow$

$D^-(\rightarrow K^+K^-\pi^-)\mu^+\nu$  and  $B_s^0 \rightarrow D_s^-(\rightarrow K^+K^-\pi^-)\mu^+\nu$ . To suppress systematic uncertainties, we measure the ratio of observed lifetime distributions. We reconstruct the visible part of the decays and correct for the momentum carried by the neutrino. We investigate the peaking background due to other B mesons and other intermediate resonances. Finally, we develop a preliminary method to eliminate peaking backgrounds.

## 1 INTRODUCTION

This report is the result of four months of part-time research at CERN for the Boston University Geneva Physics Program. I worked for the LHCb experiment, a collaboration of physicists dedicated to measuring rare decays of particles containing bottom and charm quarks.

The overall goal of the project is to establish a method to measure the difference in lifetimes of the  $B^0$  and  $B_s^0$  mesons to high precision. We use two semileptonic decays into common final states,  $B^0 \rightarrow D^-(\rightarrow K^+K^-\pi^-)\mu^+\nu$  and  $B_s^0 \rightarrow D_s^-(\rightarrow K^+K^-\pi^-)\mu^+\nu$ . In order to suppress systematic uncertainties, we measure the slope of the ratio of observed decay time distributions. The method of calculating the slope of the ratio has been used successfully in previous experiments where the decay was fully reconstructed. We apply this method to semileptonic decays of the B meson, which presents a trickier case because of the undetected neutrino. We chose semileptonic decays because the large size of available samples allows a statistical resolution at the few per mil level.

Specifically, this project aims to investigate different sources of peaking background in the observed decays. All analysis is done in the ROOT environment.

## 2 METHOD

### 2.1 SIMULATION

All analysis is based on Monte-Carlo simulations. Monte-Carlo simulation is a computer simulation of complex interactions in high-energy particle collisions. We used MC10 samples of  $B^0$ ,  $B_s^0$ , and  $B^+$ . The data sets can be found at [https://twiki.cern.ch/twiki/bin/view/LHCbPhysics/AfsData Sets](https://twiki.cern.ch/twiki/bin/view/LHCbPhysics/AfsDataSets).

### 2.2 RECONSTRUCTION OF DECAY TIME

The lifetime of a particle is defined as the average proper decay time. To measure the lifetime of a particle, one can fit the distribution of proper decay times of the particle.

The decay time of the B meson is calculated as:

$$t = \frac{M_B \cdot \vec{d}_B \cdot \vec{p}_B}{|\vec{p}_B|^2}$$

where  $M_B$  is the mass,  $\vec{d}_B$  is the measured flight distance, and  $-\vec{p}_B$  is the measured momentum. Note that in our units, the speed of light is 1.

## 3 CORRECTION FOR MISSING NEUTRINO

In order to fully calculate the lifetime of the B meson, one needs to know the full kinematics of all final-state particles. In this experiment, the kaons,  $K^+K^-$ , pion,  $\pi^-$ , and muon,  $\mu^+$ , are all observed, but the neutrino,  $\nu$ , is not. Thus the reconstructed momentum of the B meson is not equal to its true value. As the decay time of the B meson is dependent on its momentum, the decay time is not equal to the true decay time.

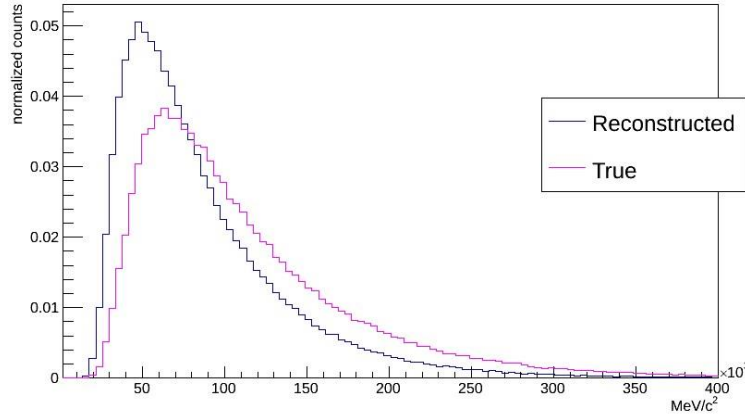


**Figure 1:** Difference between the reconstructed and true  $B^0$  momentum distributions.

### 3.1 K-FACTOR CORRECTION

The k-factor method attempts to account for the momentum of the missing neutrino. The k-factor  $k$  is calculated using Monte-Carlo simulation of the decay and is defined as:

$$k = \frac{p_B^{rec}}{p_B^{true}} = \frac{p^{rec}(KK\pi\mu)}{p^{true}(KK\pi\mu\nu)}$$

where  $p_B^{rec}$  and  $p_B^{true}$  are the reconstructed and true momentums of the  $B$  meson, respectively. Using the k-factor, the decay time can be corrected as:

$$t = t^{rec} \cdot k$$

where  $t^{rec}$  is the reconstructed time and  $t$  is the corrected time.

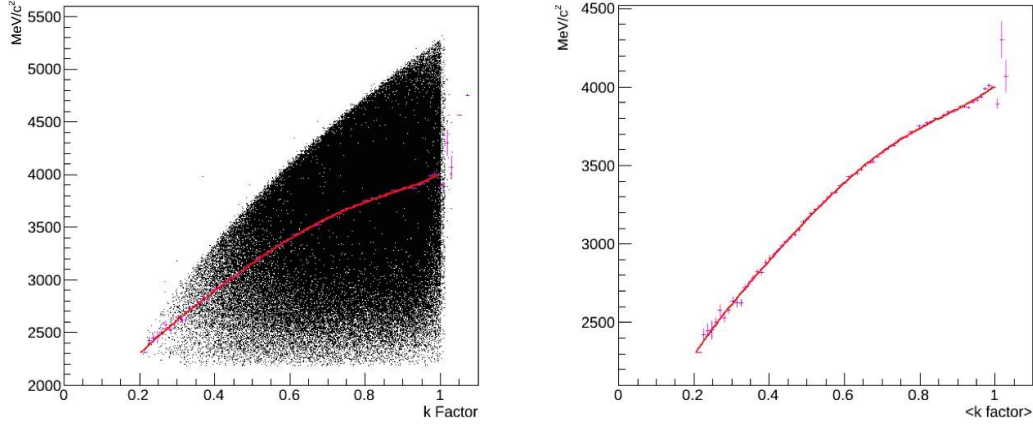


**Figure 2:** Left, scatter plot of the  $k$ -factor against the reconstructed  $B^0$  mass. Right, reconstructed  $B^0$  mass with respect to  $k$ -factor.

In figure 2, as the reconstructed  $B$  mass increases, the  $k$ -factor becomes closer to 1. This makes sense because a smaller amount of the mass was taken by the neutrino's momentum, so the correction is smaller. On the right, we have binned the average  $k$ -factor. We then fit it with a 5th order polynomial. We use this fit to find the corrected decay time.

#### 4 BACKGROUND FROM OTHER DECAY MODES OF $B^0$

There are many other decays that produce our desired observed final products ( $K^+K^-\pi^-\mu^+$ ). We used the true particle IDs to identify intermediate decays in the Monte-Carlo  $B^0$  simulation. We identified six decays that occurred frequently in the  $B^0$  Monte-Carlo simulation:

- (1)  $B^0 \rightarrow D^-(\rightarrow K^+K^-\pi^-)\mu^+\nu$
- (2)  $B^0 \rightarrow D^{*-}(\rightarrow D^-(\rightarrow K^+K^-\pi^-)\pi^0)\mu^+\nu$
- (3)  $B^0 \rightarrow D_{0*}^-(\rightarrow D^-(\rightarrow K^+K^-\pi^-)\pi^0)\mu^+\nu$
- (4)  $B^0 \rightarrow D_{0*0}^-(\rightarrow D^-(\rightarrow K^+K^-\pi^-)\pi^0)\mu^+\nu$
- (5)  $B^0 \rightarrow D^{any}(\rightarrow K^+K^-\pi^-)\tau(\rightarrow \mu^+\nu\nu)\nu$

### (6) Other

These decays are mutually exclusive. That is, if a decay is of type (1), it cannot also be of type (2), or of any other type. Furthermore, if the mother of the  $\mu^+$  is a  $\tau$ , then it must be of type (5).

The first decay is the desired decay. All other decays contribute to the background. Decays (2), (3), and (4) produce an extra pion, whereas decay (5) produces two extra neutrinos. Note that  $D^{any}$  denotes any  $D$  meson that decays into  $K^+K^-\pi^-$ . The other category includes all other intermediate resonances and decays.

## 4.1 SAMPLE COMPOSITION

The following figure shows the decay composition of the  $B^0$  Monte-Carlo simulation.

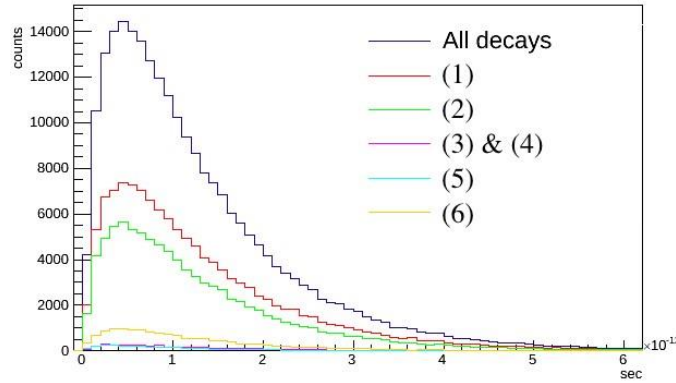


**Figure 3:**  $B^0$  true visible decay time, by decay type.

The desired decay accounts for about half of all decays that generate  $K^+K^-\pi^-\mu^+$  in the simulation, so there is a significant amount of background from other decays. Decay (2) accounts for about 40% of all decays, (3) and (4) together account for about 2%, (5) accounts for about 1%, and (6) accounts for about 6%.

## 4.2 DECAY TIMES

Because we miss at least one particle (in addition to the original neutrino) when reconstructing the  $B^0$  decay time for decays (2) through (6), the shape of the decay time distributions is not the same as that of decay (1), the desired decay.

Figure 4 shows the normalized version of figure 3, for comparison of the shape of decay time distributions. We have the  $B^0$  decay time distributions on the left and the  $B_s^0$  decay time distributions on the right. For the  $B_s^0$ , we divided the decays into six decay types. The decay types are the same as for the  $B^0$ , replacing  $B^0$  with  $B_s^0$  and adding the subscript  $s$  to any  $D$  particle. We see that the composition of the Monte-Carlo simulated  $B_s^0$  is fairly similar to that of the  $B^0$ .

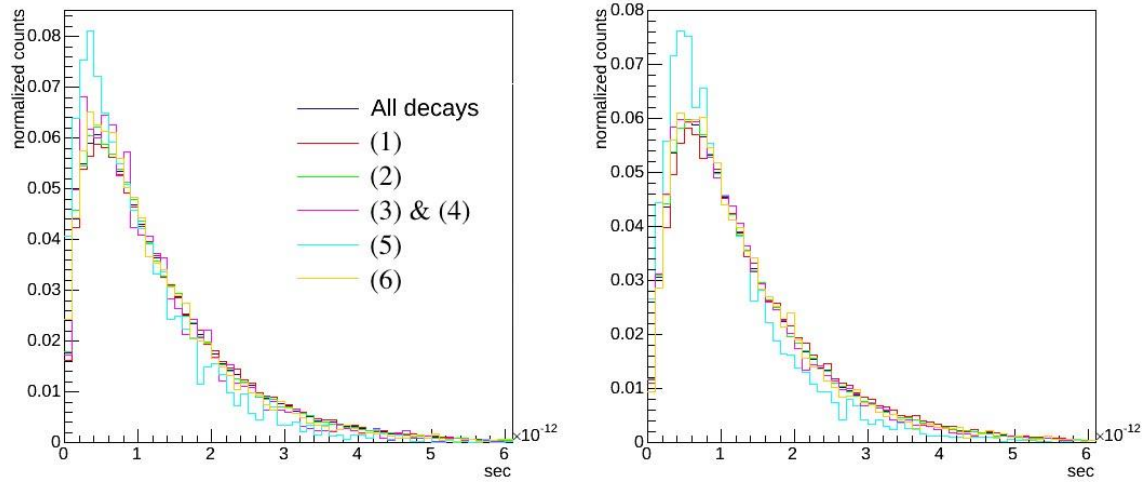


**Figure 4:** Normalized true visible decay time, by decay type (the left figure shows  $B^0$  and the right shows  $B_s^0$ )

In figure 4, the shape of the decay time distribution for decay (5), the cyan curve, is significantly different than that of the others. This is likely due to the fact that we do not detect two additional neutrinos when we reconstruct the decay. The neutrinos probably carry off more momentum, leaving us with a sharper peak.

### 4.3 K-FACTORS

If the decay time distribution varies by decay, then the momentum distribution also varies by decay and the k-factor correction will be different for different decays. This is problematic because it is difficult to distinguish between these decay types in data, so we cannot apply a separate correction for each decay type.

In figure 5, the k-factor corrections are different for different decays. As expected, the k-factor for decay (5) is significantly different from the rest, due to the missing momentum of the two extra neutrinos. Decay (1), the desired decay, is the closest to 1, as the reconstruction is missing the fewest particles. We must also keep in mind that while the k-factor distributions for decays (3), (4), (5), and (6) are very different from that of our desired decay, those decays together account for less than 10% of the decays in the Monte-Carlo simulation.

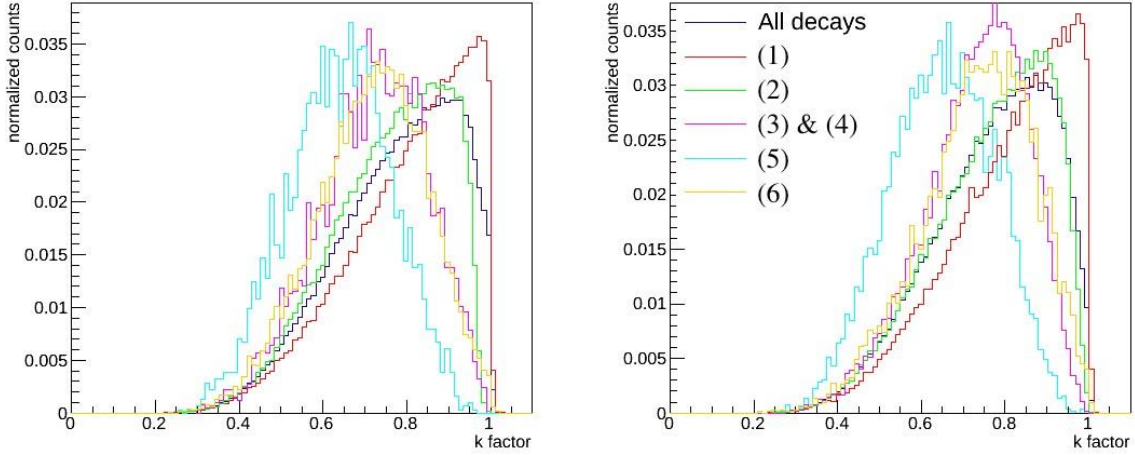


**Figure 5:** *K-factor distribution, by decay type (the left figure shows  $B^0$  and the right shows  $B_s^0$ )*

We then applied an overall k-factor correction to each decay time distribution. The overall k-factor was computed using all of the decays in the Monte-Carlo simulations.

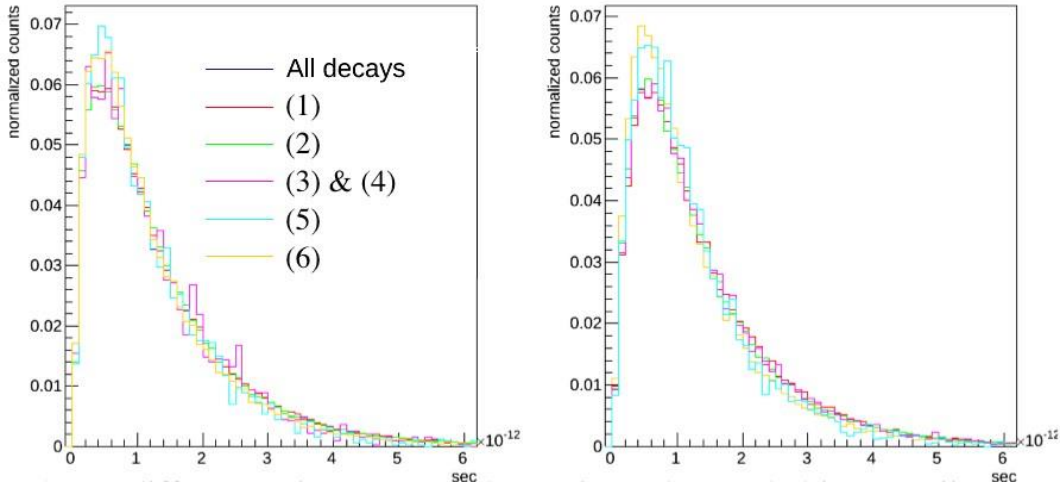


**Figure 6:** *Normalized true visible decay time with overall k-factor correction (the left figure shows  $B^0$  and the right shows  $B_s^0$ )*

With the overall k-factor correction, there are still differences in decay times, but they probably have a small effect when scaled for the contamination fractions.

## 5 BACKGROUND FROM $B^+$

The  $B^+$  meson decays to a similar final state as the  $B^0$  and  $B_s^0$  mesons:  $B^+ \rightarrow D^- (\rightarrow K^+ K^- \pi^-) \pi^+ \mu^+ \nu$ . In the final state, the  $B^+$  has an extra pion. The proportion of  $B^+ \rightarrow D^- \pi^+ \mu^+ \nu$  with respect to  $B^0 \rightarrow D^- \mu^+ \nu$  is about 10%, thus it represents a sizable background.

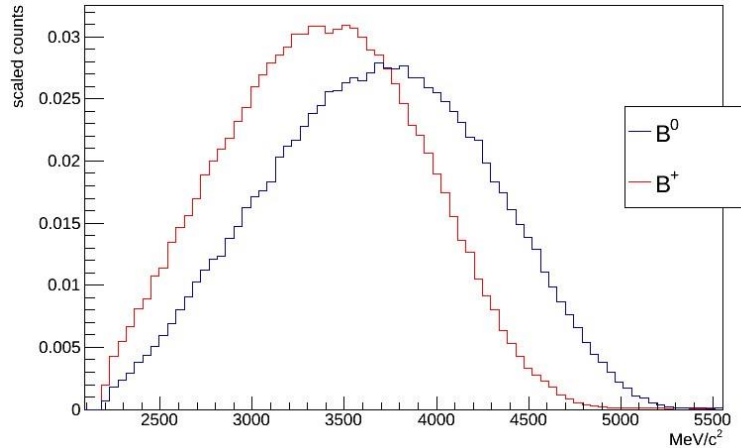


**Figure 7:** Reconstructed  $B^+$  and  $B^0$  mass distributions.

Figure 7 shows that the mass distributions of  $B^+$  and  $B^0$  are significantly different. Thus any measurement of the decay times of the  $B^0$  must take into account the  $B^+$ .

### 5.1 FITTING TO RECONSTRUCT THE SAMPLE COMPOSITION

In order to determine the percent of  $B^+$  contamination, we developed a preliminary method. It entails fitting each of the  $B^0$  and  $B_s^0$  reconstructed mass distributions with a Gaussian and then using the parameters from those fits to fit the data according to the following function:

$$h(f) = N[f \cdot G_{B^+} + (1 - f) \cdot G_{B^0}]$$

where  $f$  is the fraction of entries that are  $B^+$ ,  $N$  is a normalization constant, and  $G_{B^+}$  and  $G_{B^0}$  are Gaussians. We checked the fit performance for various true fractions of contamination. We found that we can reconstruct the fraction of total entries that are  $B^+$  fairly well (figure 8).

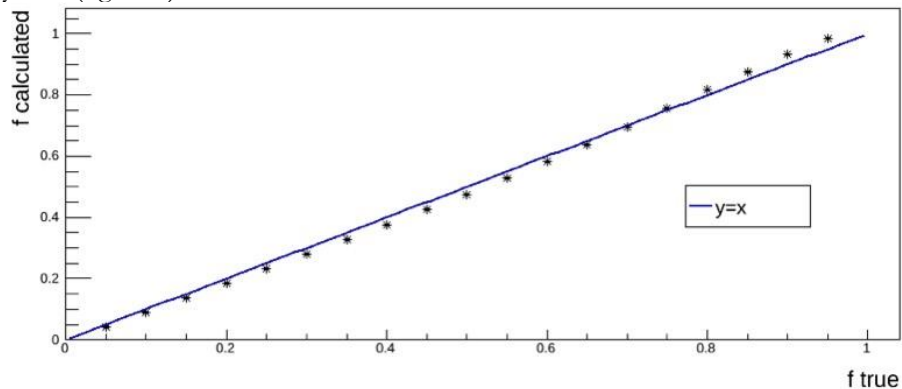


**Figure 8:** Checking the fit performance: reconstructed versus true fraction of entries that are  $B^+$ , plotted against  $y = x$ .

The preliminary fit method shows promise in reconstructing the amount of entries that are  $B^+$ . It reconstructed the contamination to around a percent. The small observed biases can probably be reduced with a more refined model.

## 6 CONCLUSION

We found that we can correct for the momentum carried by the neutrino using the k-factor method. Furthermore, we found that there is a significant amount of background from other  $B$  mesons and from decays other than the desired decays in the Monte-Carlo simulation. However, the overall k-factor correction reduces the differences in decay time distributions. When scaled for contamination fractions, the differences will probably have a small effect. Moreover, the preliminary fit method suggests that it is possible to discern the amount of  $B^+$  contamination.

So far, the challenges presented by background from other  $B$  mesons and other intermediate resonances seem conquerable. This holds promise for measuring the difference in lifetimes of the  $B^0$  and  $B_s^0$  mesons to high precision, but more work must be done to test this method. To ensure that it works for data, as well as for Monte-Carlo simulations, we need to run tests on a control group of data.



## REVIEW: ELECTRICAL COMPONENT RESEARCH AND BEAMLINE PREPARATION AT ISOLTRAP

George F. Epstein

Cornell University, Ithaca, NY 14853

Université de Genève, 1205 Genève, Suisse

Submitted: 30 June 2014

**Abstract** The following article details my four months of work at the ISOLTRAP facility at CERN during the ISOLDE facility's off-line upgrade time. Joining the ISOLTRAP team as a new recruit, I took on several side projects in preparation for new beams and new data acquisition. Over the course of this internship, I learned about vacuum systems, hardware-software interfaces, and working with electrical components. The tasks accomplished contribute not only to my knowledge, but also to the restart of ISOLTRAP at the end of the summer, and to the knowledge of the future ISOLTRAP team when further upgrades must be made.

### I. Introduction

The Isotope Separator On-Line Device (ISOLDE) facility, at the European Organization for Nuclear Research (CERN) in Meyrin, Switzerland, was taken off-line in December 2012 for technical developments and maintenance. At the time of publication, the anticipated beam restart and renewed data collection in ISOLDE was scheduled for July 2014

ISOLTRAP, the tandem Penning trap mass spectrometer at ISOLDE, is one of the experimental setups within the facility that was affected by this shut down. A pioneer in the field of Penning trap nuclear mass measurements, the ISOLTRAP setup (fig. 1a) is currently equipped with a Radiofrequency quadrupole (RFQ) cooler and buncher, a Multi-reflection Time-of-Flight (MR-

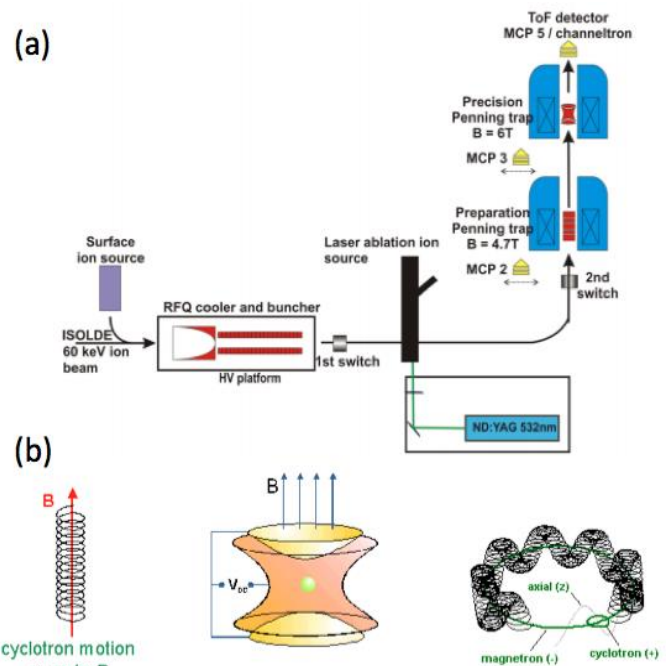


Fig. 1: (a) Diagram of the ISOLTRAP setup. (L to R) continuous beam from ISOLDE main line, surface ion source, RFQ cooler and buncher, laser ion source, MR-ToF setup (not pictured), preparation Penning trap, precision Penning trap, Time of Flight detector. (b) Diagram of the three ion eigenmotions within the Penning traps.

ToF) mass separator, and two Penning traps (preparation and precision). During beam-time, these devices have measured masses of more than 400 short-lived, exotic nuclides with a relative uncertainty  $\delta m/m \sim 5 \times 10^{-8}$  with some special cases improving that ratio by up to an order of magnitude. These measurements are important for greater understanding of nuclear structure and deformation, nuclide pairing, standard model predictions, and astrophysical nucleosynthesis.

At the time of publication, the scheduled date for ISOLTRAP to receive new beams was 1 August 2014. In the year-and-a-half bridging the dates of shutdown and restart, the ISOLTRAP team disassembled many of the parts of the experiment, tested the performance of each section of the vacuum chamber, rebuilt the system of beam optics with new components, replaced dysfunctional electrical constituents, improved the computer systems controlling the dynamic parts, gauges, and sensors, and realigned and reassembled all of the sections of the setup to a functional condition.

Between March and June 2014, I joined the ISOLTRAP team and helped with these hardware upgrades. It is these projects that will be discussed in detail in the sections below. They include wiring plugs for valve actuators, aiding in the assembly and testing of the vacuum chambers, characterizing the dynamic conduction system for the laser ion source electrodes, and characterizing the pattern of leakage resistance in capacitors

to be implemented into the RFQ cooling and bunching system.

## II. Project Descriptions

### A. Valve Actuator Plugs

As a newly arrived bachelors student who would be working closely with high-voltage electronics meant for precision nuclear mass measurements, it's understandable that my first few days of work in March were an introduction to hands-on work, and an effective test of whether or not I could be trusted.

Thus, the first task I completed at ISOLTRAP was to solder wires to the pin connections of a seven pin plastic plug (fig. 2). The pins would be placed under potential differences of several kilovolts, so it was crucial to have strong electrical contact at the soldered points and no short circuit contact between wires. Once completed, the cable was successfully tested in conjunction with the pneumatic valve and the binary switch actuation.

### B. Vacuum Testing

Due to the need for pure ion samples when performing measurements within the upper precision Penning trap, the beam-line and optics of ISOLTRAP are all placed under high vacuum when operational. This allows unobstructed ion eigenmotions within the Penning trap (fig. 1b) and a reduction of noise in the time-of-flight measurements. Part of the instrumental maintenance work at ISOLTRAP during shutdown is ensuring that all of the chambers—as well as all of



Fig. 2: Pin wiring for valve actuator plug.

the connections between sections of the setup—will not leak under high vacuum.

To test the individual sections requires cleaning the interior of the steel chamber, the cutting edges, and the O-rings with Isopropanol, followed by bolting vacuum flanges around the openings of the chambers. Once the chamber is sealed tightly, pre-vacuum is applied through a tube to bring the pressure in the chamber down to  $\sim 10^{-3}$  millibarr. An example of this setup is shown in Figure 3a. The joints (flange and connection points) of the system are then sprayed either with Helium or Isopropanol. If there are leaks while the system is under vacuum, the sprayed fluid will be taken in through the leak causing a significant rise in pressure.

Once a section successfully holds pre-vacuum, it is affixed to the other parts of ISOLTRAP for the high vacuum test. The procedure for this test is essentially the same as the pre-vacuum test, except that the chamber is connected to the rest of the experiment, and the pump-down requires a longer operation time. Figure 3b shows this test.



Fig. 3: (a) Optics chamber between the lower preparation and upper precision Penning traps. (b) Leak test of the upper part of the chamber shown in (3a).

In the case of vacuum failure (as was the case for the component shown in figure 3), the next step is to identify the point of failure. The method used is the bubble test: Place the interior of the chamber above atmospheric pressure, spray the joints with an aerosol, and watch for the presence of bubbles indicating the leakage point. This particular leaking chamber was sent to

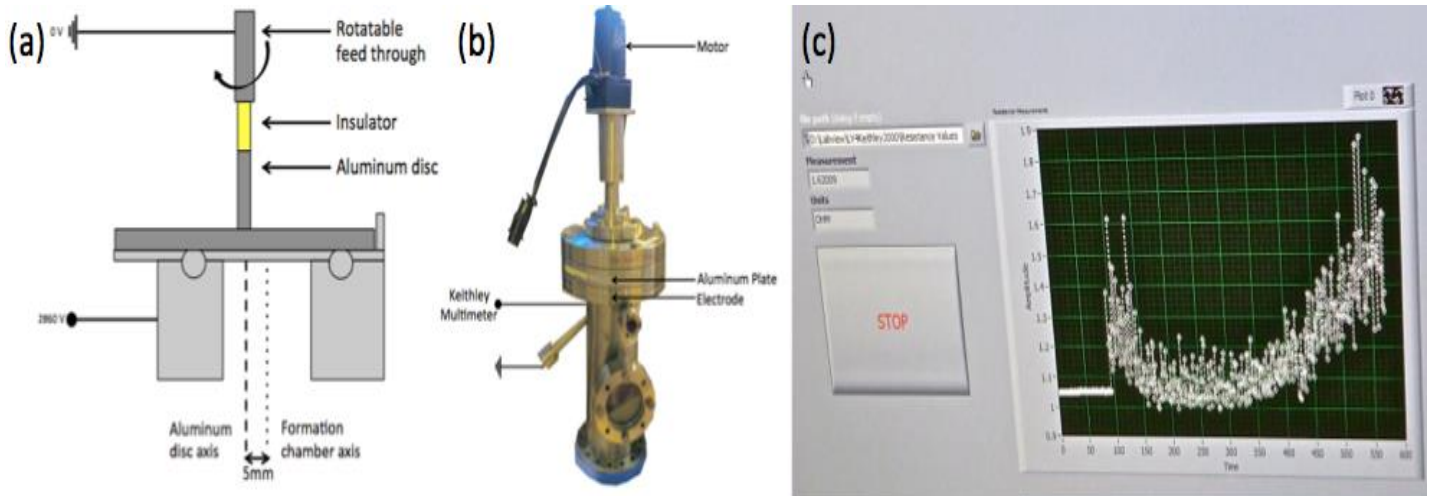


Fig. 4: (a) Schematic of the axial cross section of the laser ion source. (b) Photograph of the laser ion source with indications of the major features. (c) LabVIEW front panel of a representative resistance data sampling. The average resistance increases with increasing rotational frequency. The slight decrease  $\sim 430$  seconds into sampling is due to a direction change in the motor. The dramatic resistance increase and instability is due to the unstable direction of the motor.

technicians at CERN for repairs following the identification of the leak.

### C. Laser Ion Source

The ISOLTRAP Laser Ion Source is used to provide Carbon ions for reference in mass measurements; since the unified atomic mass unit is defined as one-twelfth of the mass of a neutral, unbounded Carbon-12 atom, the singly charged Carbon ions provide an acceptable approximation for mass comparison.

This particular source chamber (fig. 4a) is installed after the RFQ Cooler and Buncher and injects Carbon ion clusters up to the Penning traps. Over the last several years, the formation chamber has undergone several iterations. The present model uses an aluminum plate rotating 5mm off the central axis of the chamber. This plate contains the Carbon source and is electrically contacted to the base electrode by a ring of ball bearings. The lower electrode is held at  $\sim 3\text{kV}$  and the

resulting potential is used to inject the newly created ions into the beam path.

In order to ensure good injection capabilities, it becomes necessary to create good electrical contact between the aluminum plate and the lower electrode. Doing this is rendered more difficult by the rotation of the plate, which is a necessary action to make sure that the pulsed laser does not repeatedly strike the same spot on the Carbon sample, thus depleting the sample in an uneven fashion.

The test I performed to investigate this electrical contact used the Keithley Model 2000 Digital Multimeter, and LabVIEW Version 9. The multimeter (used here on the ohmmeter setting) was connected to the lower electrode while the chamber casing (fig. 4b)—in electrical contact with the aluminum plate—was connected to ground. With the motor turning the aluminum plate, the LabVIEW Virtual Instrument (VI) read resistance measurements off of the

multimeter each second and plotted those measurements on a waveform chart (fig. 4c). Higher average resistance indicates lower electrical contact and vice versa. Too much electrical contact forces the motor to overwork and decreases performance. Following each of these acquisition sessions, position adjustments were made to the plate to optimize the ratio of resistance to friction.

After many tests and adjustments of this system, it became clear that the mechanism that was simultaneously holding the plate and insulating it from the motor arm was unstable, making the system performance extremely subject to initial conditions. At the time of publication, new methods are being investigated to provide a stronger connection between the two system components and a summer graduate student is investigating more stable configurations that allow for a good amount of pressure and translational freedom while maintaining good electrical contact.

#### ***D. Capacitor Leakage Resistance: The Multi-Reflection Time-of-Flight Mass Separator***

##### ***i. Setup and Initial Testing***

One of the new installments to the ISOLTRAP facility is the Multi-Reflection Time-of-Flight (MR-ToF) Mass Separator between the Radiofrequency Quadrupole Buncher and the dual Penning Traps. The MR-ToF uses two electrostatic ion optical mirrors—whose potentials are adjusted to

allow controlled oscillations of the ions of interest—and a Bradbury-Neilson beam gate to filter out unwanted ions. Such action allows for greater purification of ion beams than was previously allowed by the ISOLTRAP setup.

The high voltage, high precision power sources used at ISOLTRAP are (despite their production standards) subject to noise and thermal fluctuations; as much as touching the doorknob of the laser room in which the MR-ToF is housed is enough to cause unwanted voltage changes on the electrode mirrors which decreases the separation precision of the MR-ToF. To counteract this result high voltage (40 $\mu$ F, 4100V) capacitors are installed serially to reduce fluctuations to zero. These capacitors (products of General Electric) are ceramic plates encased in an aluminum housing with solid ceramic terminals.

It is important that these capacitors function as closely to ideal performance as possible. Therefore, a key characteristic of the non-ideal capacitor, the leakage resistance, must be determined, and only capacitors with leakage resistances above a certain value (i.e. several gigaohms) can be accepted. This leakage resistance should thus be known to within an order of magnitude to estimate its efficacy in noise reduction. To achieve this end, the following procedure was established to determine the leakage resistance—the nature of the methodology is similar to that for determining the optimized configuration of the Laser Ion Source.



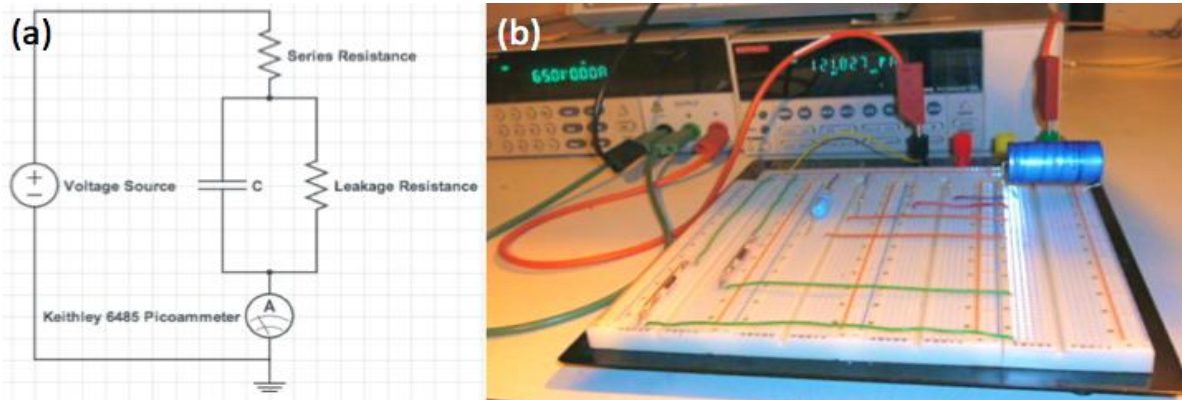


Fig. 5: (a) Circuit diagram of the experimental setup. The real capacitor is shown as the parallel branch of an ideal capacitor,  $C$ , and the Leakage Resistance. (b) Photo of the experimental setup with a  $1000\mu\text{F}$  electrolytic capacitor

The setup is outlined in Figure 5a and shown in Figure 5b. A DC voltage supply is connected to an RC series circuit, and the current through the circuit is read through another LabVIEW VI (fig. 6) through the Keithley 6485 Picoammeter. The real capacitor with leakage resistance is modeled as an ideal capacitor in parallel with an ideal resistor. The series resistance is chosen based upon the capacitor to achieve a good compromise between the approximate time constant<sup>1</sup> and the circuit stability—too high of a resistance will cause a very slow current decay and will make the final current low enough to be greatly distorted by background noise, while too low of a resistance can cause a current overload in particular at the high voltage range.

When the voltage supply is set to constant voltage,  $V$ , the capacitor is

initially discharged and acts as a short circuit to ground. The initial current is thus:

$$i_{\text{initial}} = \frac{V}{R_{\text{series}}}$$

The capacitor then charges over time towards its final voltage. When this happens, current only passes through the series resistor and the leakage resistance which makes the final current:

$$i_0 = \frac{V}{R_{\text{series}} + R_{\text{leakage}}}$$

It is this value that is of particular interest, because by rearranging this relationship, we arrive at an expression for  $R_{\text{leakage}}$  based solely on controlled parameters (applied voltage and  $R_{\text{series}}$ ) and experimentally-determined results:

<sup>1</sup> The time constant of the ideal RC circuit is simply the product of the resistance (in ohms) and capacitance (in farads). Since this circuit does not have a current decay to exactly zero, but to a small, non-zero value, the decay time is not quite this value, though it remains a good estimate, as evidenced by the experimental results obtained.

$$R_{leakage} = \frac{V}{i_0} - R_{series}$$

To obtain an asymptotic value of the circuit's current, the data sets were

extrapolated value of  $i_0$ , the major quantity of interest.

To verify that this method works and that the setup can be safely extended to high voltage experimentation, a number of tests on small, low voltage capacitors

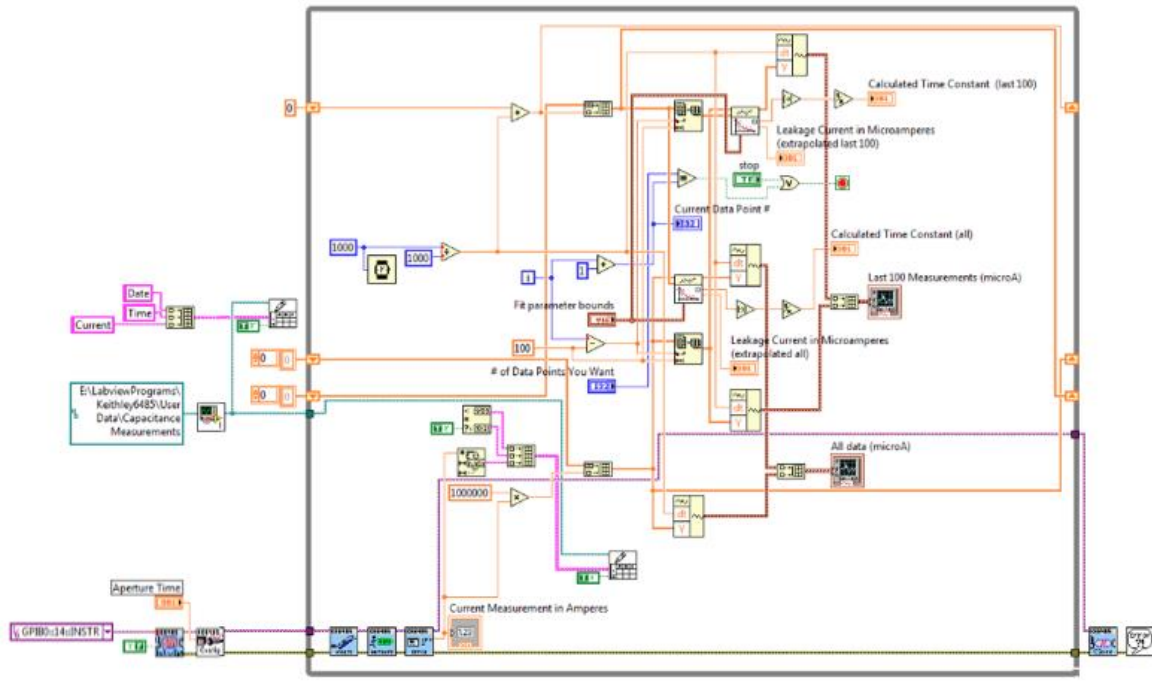


Fig. 6: LabVIEW Virtual Instrument for measuring the current of the charging RC circuit. Output waveforms of the VI are graphs of the entire decay curve and of the most recent 100 measurements. The second waveform gives a more perceivable measure of when the current has approached its final constant value.

imported into Oracle 7 and fit with a function comprised of the sum of three exponential decays and a constant of the form:

$$i(t) = i_0 + \sum_{j=1}^3 A_j e^{-\frac{(t-t_0)}{t_j}}$$

Though there does not appear to be an easily determined physical explanation for the fit equation's form, this particular form was used because it provided the highest  $R^2$  value (in most cases, unity), which suggests the most accurate

(ceramic and electrolytic) were performed. Figure 7 displays a sample curve from one of these capacitors. Based on the asymptotic fit values, data was gained with regards to the capacitor leakage resistance (tab. 1). It should be noted that, while the presented data is not sufficient enough to draw definitive conclusions, there seems to be a negative correlation between capacitance and associated leakage resistance, enough to motivate a further investigation into the study.

<b>Table 1: Leakage Resistance of Sample Capacitors (V=20.0V)</b>		
Capacitance (C) ( $\mu F$ )	Final Current ( $i_0$ ) (nA)	Leakage Resistance ( $R_L$ ) (M $\Omega$ )
47	269	73
470	319	62
1000	1324	15

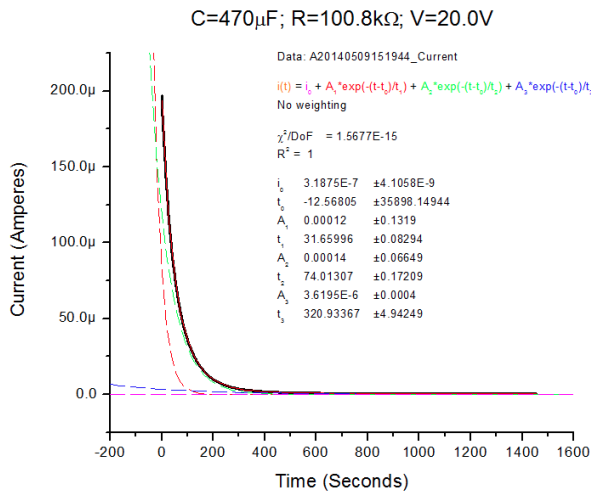


Fig. 7: Sample decay curve for a test  $470\mu F$  electrolytic capacitor. Exponential decompositions displayed and final, asymptotic current given here.

## ii. The Semi-High and High Voltage Regime

After completing the low voltage tests and streamlining the experimental process, attention turned to the high voltage capacitors. A photograph of this modified setup—with high voltage source and the grounded capacitor cage—is shown in Figure 8. The same approach was used for these high voltage capacitors as for the test capacitors. Six capacitors were tested at voltages ranging from 0.100kV to 2.800kV. 0.100-1.500kV constitutes the “semi-high” regime (trials conducted with the circuit

unshielded) while 0.100kV-2.800kV constitutes the “high” voltage regime (trials conducted with a shielded circuit as shown in Figure 8). Data was analyzed to produce plots of Leakage Resistance (in  $G\Omega$ ) versus Applied Voltage (in Volts). The main method for achieving these plots involved calculating the Leakage Resistance—as described in the previous section—then plotting these

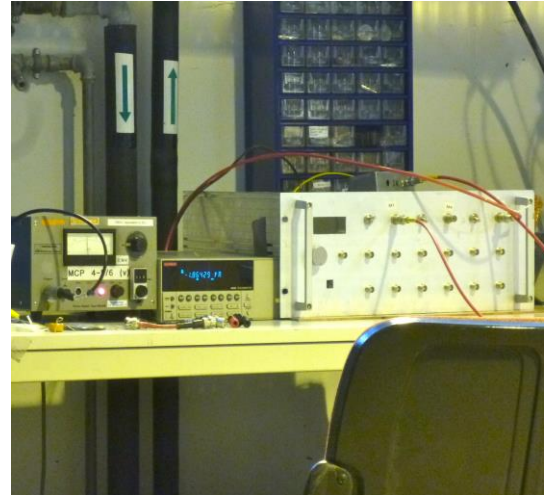


Fig. 8: High Voltage configuration for capacitor testing. L to R: Voltage source (up to 2.800kV), Keithley 6485 Ammeter, Capacitor shielding cage.

values against the voltage applied from that trial. The plots obtained from this method are shown in Appendix A for all six capacitors. In examining these results, it becomes clear that there is a marked discrepancy between the results from the shielded and unshielded trials as shown for Capacitors 1-3. The unshielded results seem to have a much higher voltage-dependent leakage resistance. To rule out errors in the voltage source (two different sources were used at various times throughout the trials) the possible combinations of voltage sources and experimental configurations were



retested. After ruling out errors due to the voltage sources through these tests, the data analysis was examined. As an alternative approach to the fit test, an average of the final 100 data points from each of the Capacitor 1 unshielded trials was taken, and these average values were used as the  $i_0$  values for each trial. Plugging these values into the equation for  $R_L$  yielded new results for the leakage resistances in the unshielded configuration that were much more faithful to those of the shielded configuration. This plot can be found in Appendix B.

Regardless of the method by which the data is analyzed, the result is evident in each capacitor: There exists a direct correlation between the leakage resistance of the capacitor and the voltage applied across its terminals. This resistance levels off (to  $\sim 2\text{G}\Omega$ ) as the voltage approaches the patent maximum voltage of the capacitor.

### III. Closing Notes

#### A. Summary

In four months of working at the ISOLDE facility, I gained hands-on experience with electrical systems, vacuum systems, data acquisition and analysis. The main result of my work, which adds to the scientific knowledge

base at ISOLTRAP, is the quantified characteristic behavior of the six capacitors that will be used for the MR-ToF mass spectrometer. Since most components used at CERN (such as the large capacitors) are recycled components, the methods used to test these components are invaluable to further upgrade procedures.

#### B. Still to Come

During the weeks following my departure from ISOLDE, the ISOLTRAP team continues to prepare for the first beams and new data. This includes the implementation of the stabilization capacitors in the MR-ToF power supply circuits as well as the revision and reconstruction of the rotating electrode support mechanism in the Laser Ion Source.

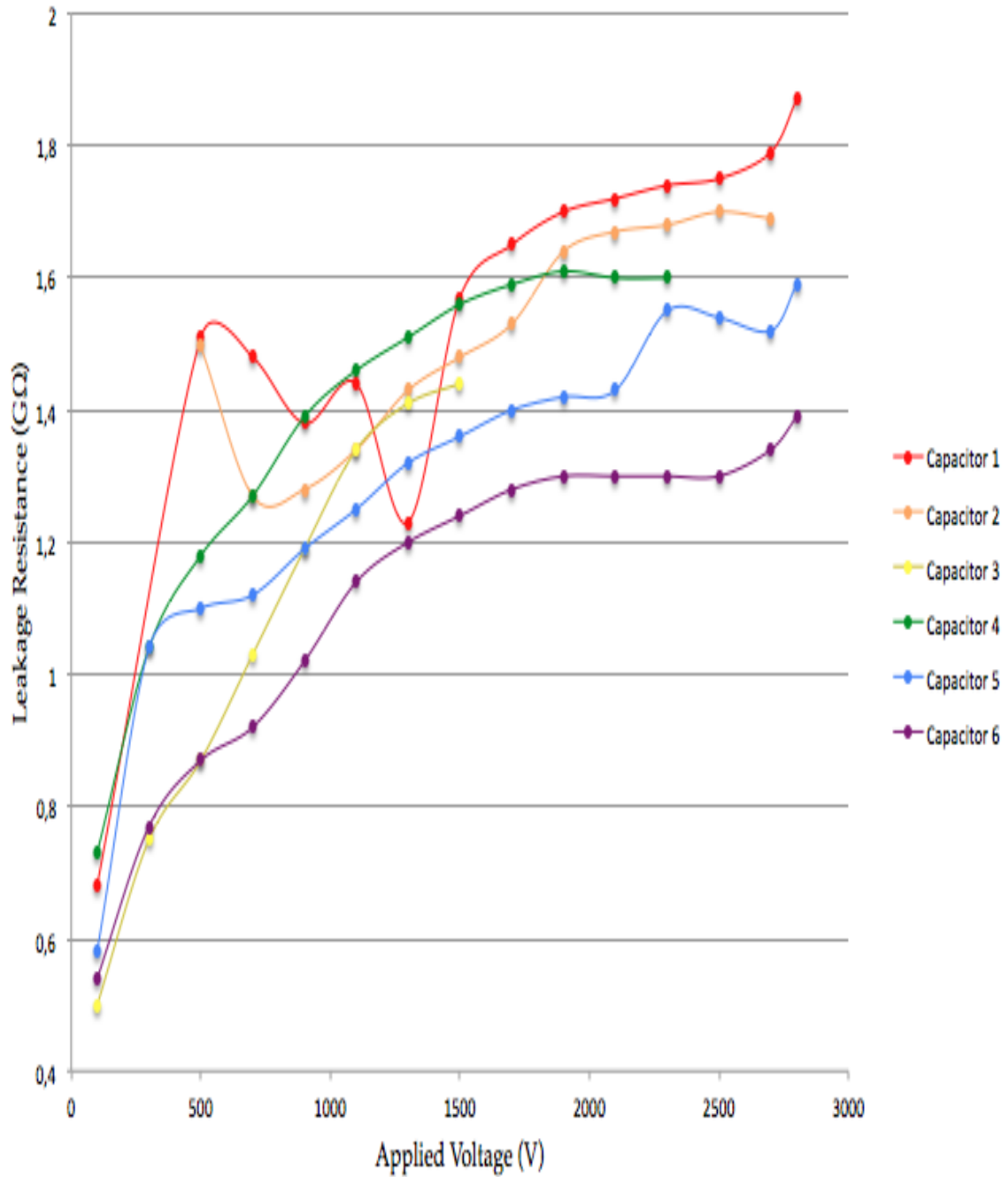
#### C. Acknowledgements

I would like to thank the team at ISOLTRAP: Frank Wienholtz, Vladimir Manea, Dinko Atanasov, Dmitry Kisler, Andree Welker, and Ian Murray. I would like to acknowledge the ISOLDE Scientific Coordinator, Magdalena Kowalska, and the ISOLDE Physics Coordinator, Maria Borge. Finally, I would like to thank Augusto Ceccucci.



## Appendix A

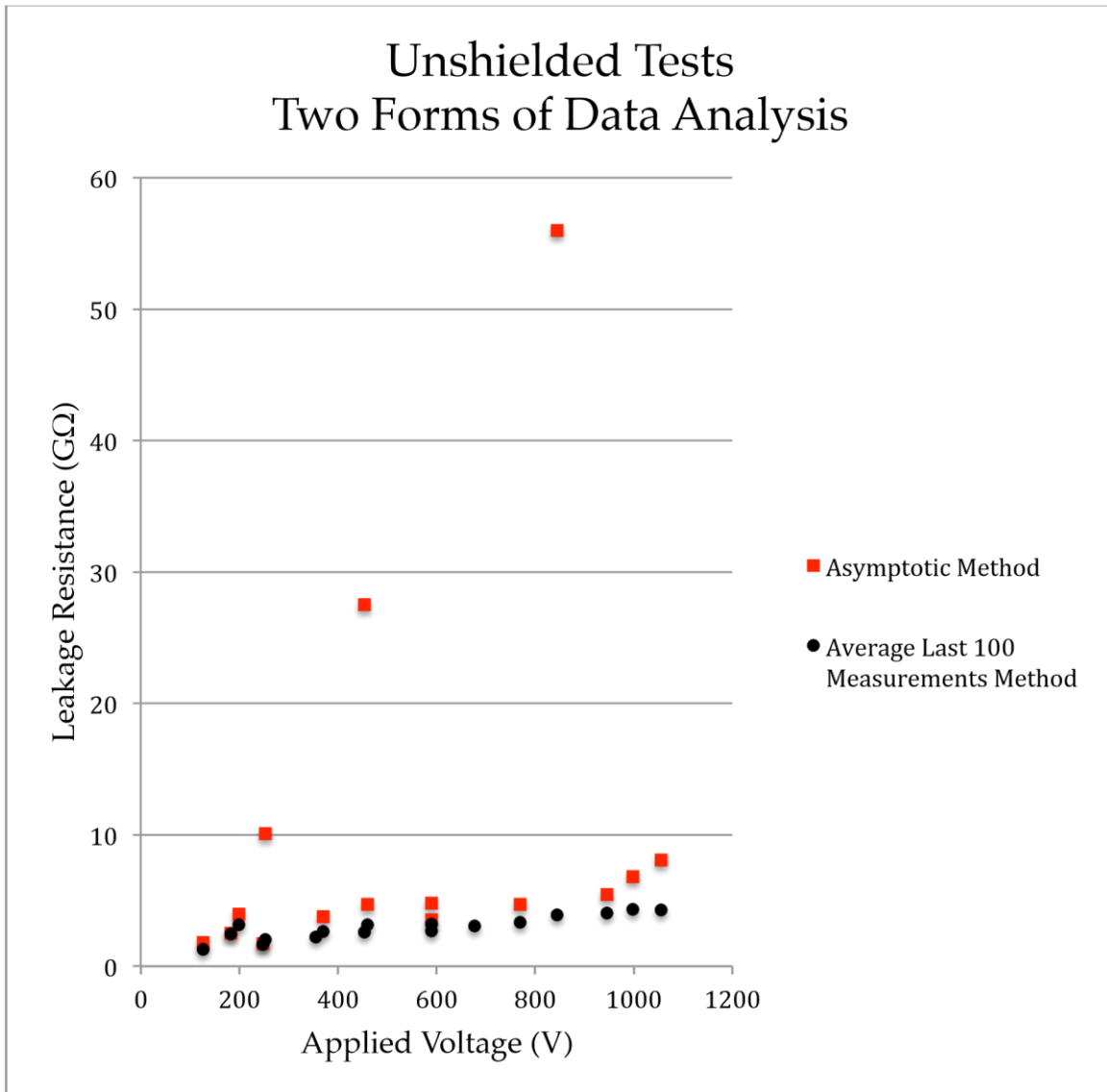
### Leakage Resistance Versus Applied Voltage Fit Line Method



---

**APPENDIX B**

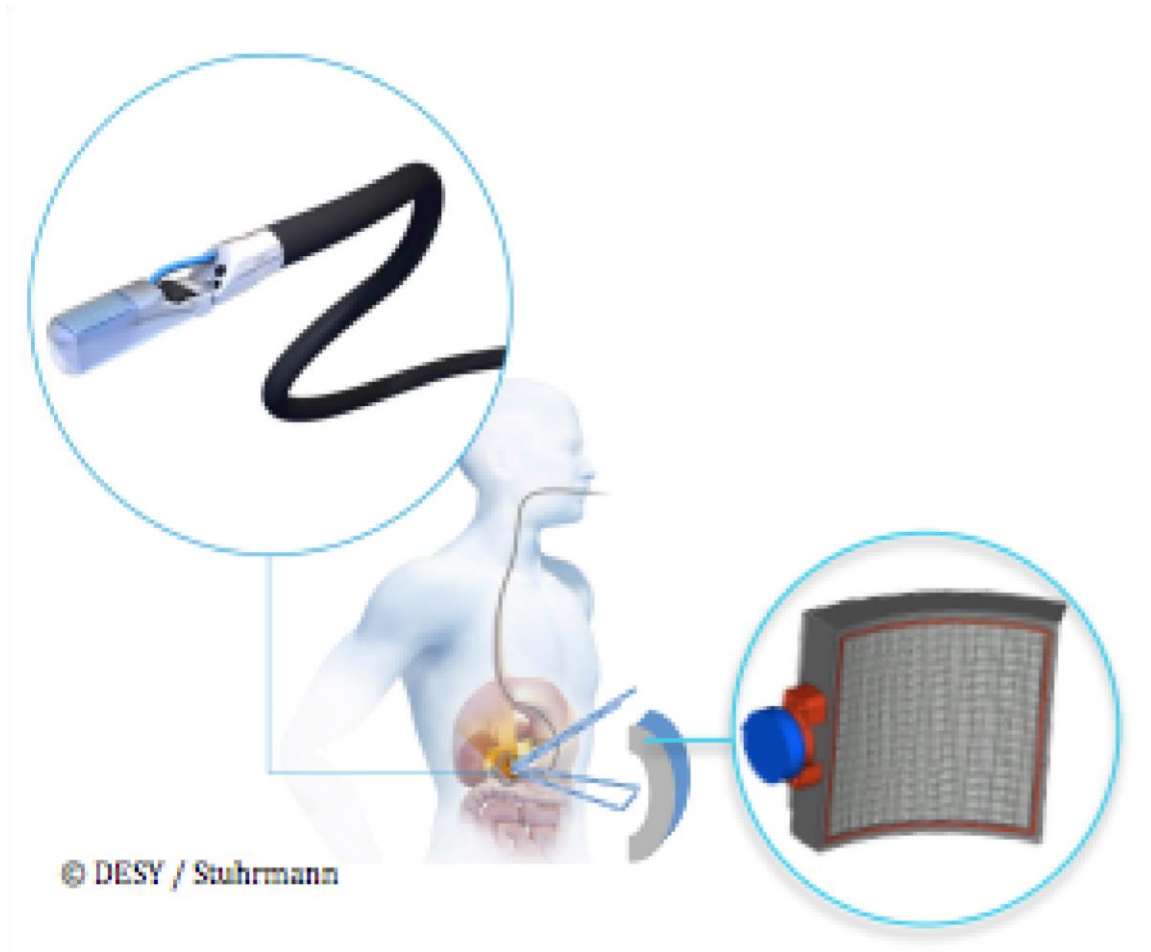
---



---

**ENDOSCOPIC TIME-OF-FLIGHT POSITRON EMISSION TOMOGRAPHY: FOR THE  
EARLY DETECTION OF PANCREATIC AND PROSTATE CANCER**

---



Inna Gertsenshteyn  
Augusto Ceccucci  
PY392: Directed Study at CERN  
Spring 2014

Supervisors:  
Etiennette Auffray  
Giacomo Cucciati  
Marco Pizzichemi

In the spring of 2014 I worked with Crystal Clear Collaboration, in the EndoTOFPET-US group. The overall goal of the EndoTOFPET-US project is to create an instrument that detects pancreatic and prostate cancer earlier, with more efficiency and less cost, than the machines and methods that are used in medicine today. For example, endoscopic ultrasound procedures and full body PET scans are often used separately for analyzing the pancreas and prostate. However, it would be greatly beneficial to combine the two methods of detecting cancerous lesions in order to have accurate imaging along with metabolic information. Particularly for the pancreas and prostate, which are small and located near other organs that have a naturally high intake of Fluorodeoxyglucose (FDG), it is difficult to detect small lesions from only a PET scan. The EndoTOFPETUS, however, has a small PET detector containing LYSO crystals that is capable of focusing on the areas of the prostate and pancreas with a very good spatial resolution and signal to noise ratio. This will allow oncologists to detect small lesions that would not be found by simply using today's methods, and diagnose these deadly cancers early enough to increase the patient's chances of survival.

Physically, the EndoTOFPET-US is a small PET detector head clamped onto a commercial endoscopic probe that is inserted inside the body, as shown on the cover page. Outside of the body is a PET plate. Following the procedure taken for a regular full body PET scan, FDG is injected into the patient's body because cancerous cells absorb more glucose than healthy cells, so there is more FDG found in the tumors. The FDG releases positrons, which emit two gamma rays of 511 keV in opposite directions. The probe and plate detect these gamma rays, and the location of the source is found from the point at which the lines connecting gamma pairs cross. The ultimate goal of this project is to obtain a coincidence time resolution of 200 ps and spatial resolution of 1mm from the device.

Under the direct supervision of Giacomo Cucciati and Marco Pizzichemi, I learned the basics of coding in GAMOS and GEANT4, ran simulations to analyze different medical scenarios, and measured the scintillation properties of a large variety of crystals by physically wrapping them in different materials and finding energy peaks with the lab's PMT.

I started work at CERN at about the same time as Giacomo, who was just beginning to learn how to use GAMOS with colleagues from DESY and SurgicEye, Milan Zvolsky and Áron Cserkaszky. Before I arrived they had been using GATE, but there were too many problems with implementing asymmetric detectors, generating large output files, and it was impossible to place detectors inside the body during simulations without leaving a small gap of air, which is a critical defect. Therefore, we were all learning how to use GAMOS at the same time.

The first thing I worked on after successfully installing GEANT4 and GAMOS onto my computer, which took a few days longer than expected, was to create a phantom of the pancreas and surrounding organs in GAMOS. I learned from reading the manual and followed Giacomo's style from when he created phantom of the prostate. The basic procedure I followed was to research the average size and location of organs and bones surrounding the pancreas, and to make sure that they do not overlap with each other when creating them in GAMOS. I used the average sizes of male organs, since the phantom for the prostate was based on male proportions, for obvious reasons. The final version of my phantom of the pancreas and its surrounding organs is shown on the next page.

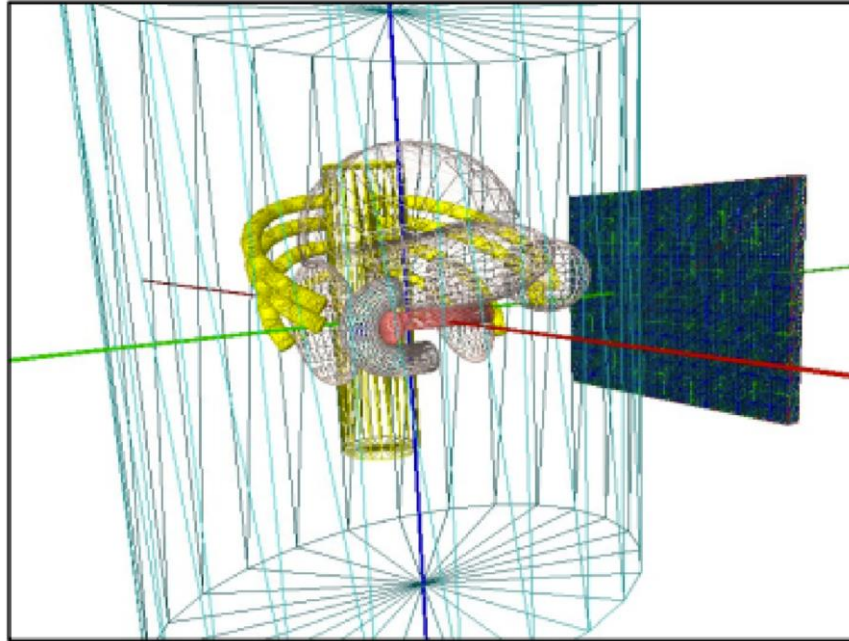


Figure 2: The pancreas is pictured in red at the center of the body. The bones are yellow, and enclosed organs are white. If you look closely, the PET head is inside the curved small intestine, located behind the pancreas, and the PET plate is outside the body.

GAMOS allows you to place a radioactive source, either a point source or one evenly distributed throughout a volume, anywhere in the phantom. That way we can analyze how quickly and at what energies the gammas reach the probe and plate from the source, and we can mimic small lesions of an early stage of cancer. The phantoms were sent to DESY to find the most effective cut level of gammas that were scattered or random based on their energy and time. For example, whether it is best to reject gammas with some energy below a particular threshold, or outside of some time difference between the gamma hitting the probe and its paired gamma hitting the plate. The plots shown on the next page are a good summary for the information provided by the phantoms:

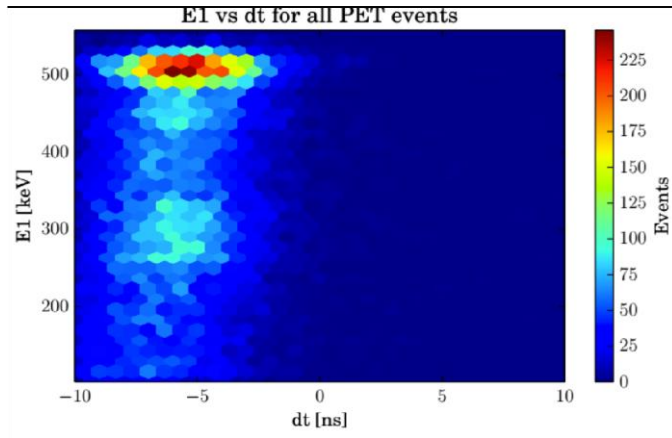


Figure 3: E1 is the energy level detected by the plate, and dt is the difference between the time it took for one gamma to reach the probe subtracted from the other to reach the plate. The highest number of events is around 511 keV, which is the energy we have from the annihilation. Lower energies around 300 keV come from Compton scattering.

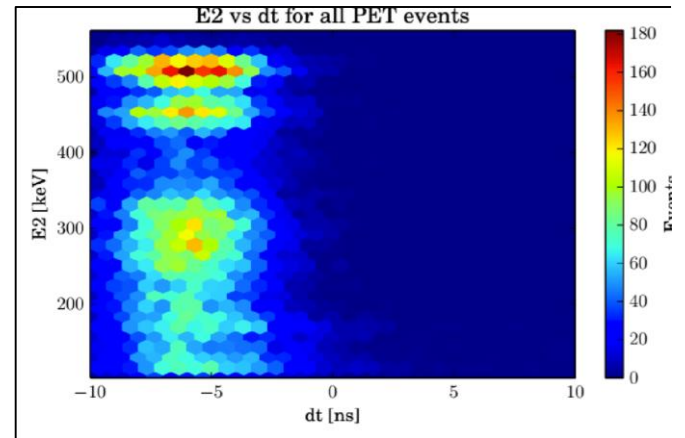


Figure 4: E2 is the energy level detected by the probe, and dt is the same as in Figure 3. The second peak right below 511 keV comes from the electron knocked off the Lutetium atom (from the LYSO crystal), which gives off energy of 511-63 keV. Again, energies below that at around 300 keV are from Compton scattering.

From the energy versus time distributions above, it was interesting to see in Figure 4 that there was a second peak below the expected 511 keV from the gammas. That turns out to be the energy from the K-alpha emission of Lutetium's valence electron with energy of 511-63 keV. We also saw this peak when measuring LYSO crystals on a PMT with a Cs137 source. Due to the small crystals inside the probe, and the probe's close proximity to the gamma ray source, it detected the energy loss. Therefore, in Figure 4, you see two peaks around energies 511 keV and 448 keV. But in Figure 3 for the plate with larger crystals, by the time de-excitation happens, both peaks add up to 511 keV. The group concluded that it makes sense to sum up both peaks when analyzing data from human subjects. Also, due to a clear line at which detected energies come from the Compton effect (340 keV) when compared to the large distribution of dt, it is better to reject rogue gammas based on their energies rather than the time it takes for them to reach the detectors.

Another use for the phantoms is to see how a radioactive point source of 1mm, a realistic size for a small lesion of the early stages of cancer, would look. The dimensions of the following figures are 3x3cm, and the red voxels represent the radioactive source.



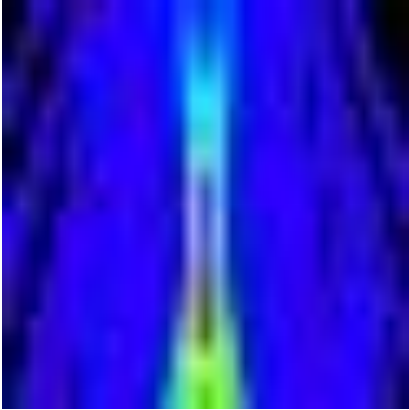


Figure 5: Radioactive source seen from a stationary plate and stationary probe.

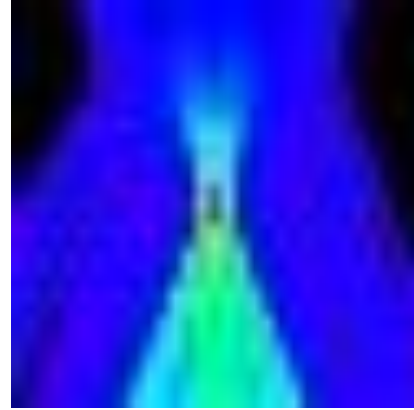


Figure 6: Radioactive source seen from a moving plate and moving probe.

Within GAMOS we are able to run a simulation that allows the probe and/or plate to rotate around the source in any direction or angle we tell it to. From Figure 5, it is clear that leaving both the probe and source stationary makes it difficult to pinpoint where the source is in the body. However, if you rotate the plate around the body by a few centimeters and the probe as well (not quite as much as you would move the plate), the source's true location becomes much easier to see, with a much better resolution. The only problem is that it is not very realistic to move the probe around very much, especially near the pancreas for a small patient. Either way, we see that it is necessary to move the outer plate, which will be implemented in the final physical design of the product.

A couple of weeks after Giacomo and I created these phantoms, we received CT and PET scans from real patients from a hospital in Lausanne in DICOM format. Converting the data into files read by GAMOS, we were able to add radioactive sources that represented tumors into the pancreas or prostate, insert the probe in the small intestine or colon, and observe how our EndoTOFPET-US receives gammas among the background noise that I mentioned in the beginning of the paper. For example, in a healthy person, FDG is naturally absorbed by the liver and kidneys and other organs, which you can see lit up in the PET scan shown above. After running very long simulations to be completely sure, we discovered that the background noise is not an issue, even for very small lesions represented by point sources.

When I was not running simulations with Giacomo, I worked with Marco in the lab. My primary role in the lab was to wrap crystals in various materials, such as Teflon or Vikuiti, and measure the energy distribution of crystals varying in size of a PMT. These measurements were for providing real data for people in other parts of Crystal Clean Collaboration who were purely running simulations, so that the results from their simulations would be more accurate. They were looking for crystals with a high scintillation light yield, which is why we were testing different dimensions of crystals (mostly LYSO).

Because we were using Cesium-137 with the PMT, I received radiation training and had my own dosimeter to wear in the lab. There I learned how a PMT works, how to take data from it using ROOT,

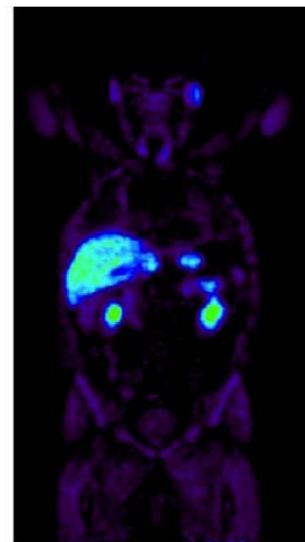


Figure 7: PET scan showing natural intake of FDG.

and the frustrations of things physically not going the way you want them to, which is an experience reserved for experimental physicists. Especially working with small crystals (some were about 5x5x5 mm), wrapping them in flimsy material was very tedious and difficult to do all day in a dark room.

Overall, I had an excellent time working with Crystal Clear Collaboration, and was very lucky to have the opportunity to apply my old and newfound knowledge of physics to medicine. Everyone here is great to work with, and I would highly recommend future students to work in this group, especially if they want a taste of both hands-on work and computer work. In the future, there will be many variations to the type of projects I've done, either with my mentors or others who are just as qualified and helpful.



# **Optical Pumping Simulations of Copper Isotopes**

Julie Hammond  
Boston University  
COLLAPS  
ISOLDE  
CERN

Geneva, June 2014

---

## CONTENTS

---

<b>1. Introduction</b>	<b>1</b>
<b>2. Technique</b>	<b>2</b>
2.1 Atomic Rate Equations.....	2
2.2 Nuclear Polarization.....	2
2.3 Optical Pumping.....	3
2.4 Interaction Time and Power Density.....	5
<b>3. Results</b>	<b>6</b>
3.1 Comparison with Published Results.....	6
3.2 Nuclear Polarization of <sup>58, 74, and 75</sup> Cu.....	7
3.3 Saturation Plots for Power Density and Interaction Time.....	8
<b>4. Conclusions</b>	<b>8</b>
4.1 Optimal Frequencies .....	8
4.2 Outlook.....	9
<b>5. References</b>	<b>9</b>
<b>6. Acknowledgements</b>	<b>10</b>

---

## 1. INTRODUCTION

---

Optical pumping with circularly-polarized light can change the populations of atomic states, and thus it can polarize electron spins. Via the hyperfine interaction, this process also gives rise to a polarization of the nucleus, which can be used to study  $\beta$ -decay. Furthermore, it is well known that fine structure energy levels split when placed in an external magnetic field, according to the Zeeman effect. Equally interesting is the splitting of the hyperfine structure when the magnitude of the magnetic field is increased. At small fields, the electron and nuclear spins remain coupled, but as the strength of the field increases, the spins decouple and the nuclear-spin polarization is thus unobservable while neglecting the electron spins.

The degree of spin polarization has been simulated in order to determine which atomic transitions provide the largest nuclear polarization for copper isotopes <sup>58, 74, and 75</sup>Cu, for both positively and negatively circularly polarized light, as a function of the laser power density and the interaction time of the ions with the laser beam. The results of the simulations be used in data analysis for an experiment at the CERN ISOLDE facility studying copper's interaction with the body, planned to take place in the next five years.

The experiment will employ for the first time  $\beta$ -NMR technique ( $\beta$ -nuclear magnetic resonance) to liquid samples to study the interactions of trace elements within the body, which had previously been difficult to observe due to a lack of sensitivity of traditional NMR. By measuring the angular distribution of the  $\beta$ -decay of radioactive isotopes, rather than the electrical signal measured in traditional NMR,  $\beta$ -NMR's sensitivity is 10 orders of magnitude greater than traditional NMR.

---

## 2. TECHNIQUE

---

### 2.1 ATOMIC RATE EQUATIONS

Optical pumping simulations were done previously for the CERN-ISOLDE nuclear physics experiment on  $^{29}\text{Mg}$  and  $^{31}\text{Mg}$  in 2006 [Kow06], and this code was used as the basis for the copper simulations. The code describes the atoms and laser beam by perturbation theory to the first order, following a semiclassical approach, leaving the populations of the higher energy states very small compared to the population of the lower energy states. Thus, treating a twolevel system, the atomic rate equations are:

$$\begin{aligned}\frac{d}{dt}N_i &= \sum_j P_{ij}^{st}(\nu)(N_j - N_i) + \sum_j P_{ij}^{sp}N_j \\ \frac{d}{dt}N_j &= \sum_j P_{ij}^{st}(\nu)(N_i - N_j) - \sum_j P_{ij}^{sp}N_j\end{aligned}$$

where  $N_i$  is the population of the ground state,  $N_j$  is the population of the excited state,  $\nu$  is the laser frequency, and  $P_{st}$  and  $P_{sp}$  are the probabilities for stimulated and spontaneous emission between levels  $i$  and  $j$ .  $P_{sp}$  is equal to the Einstein coefficient  $A_{ij}$ , which may be derived from the lifetime of the excited state,  $\tau \approx 7.3$  ns. The stimulated emission probability is given by

$$P_{ij}^{st} = \left(\frac{c}{2\pi\nu}\right)^3 \rho_{las} \frac{A_{ij}}{2h\tau} \frac{1}{(\nu_{ij} - \nu)^2 - (1/(2\pi\tau))^2}$$

where  $h$  is Planck's constant,  $\nu_{ij}$  is the frequency corresponding to the energy difference between the ground and excited states, solved from Planck's relation, and  $\rho_{las}$  is the laser power density. [Bra83].

The above rate equations were solved using the numerical approach of 4<sup>th</sup> order RungeKutta (RK4) method. To improve accuracy, a second code was written including the metastable state (a state into which the excited state may decay, other than the ground state). The second (three-level) code was cross-referenced against the two-level code by setting the probability of transition to the metastable state to zero.

### 2.2 NUCLEAR POLARIZATION

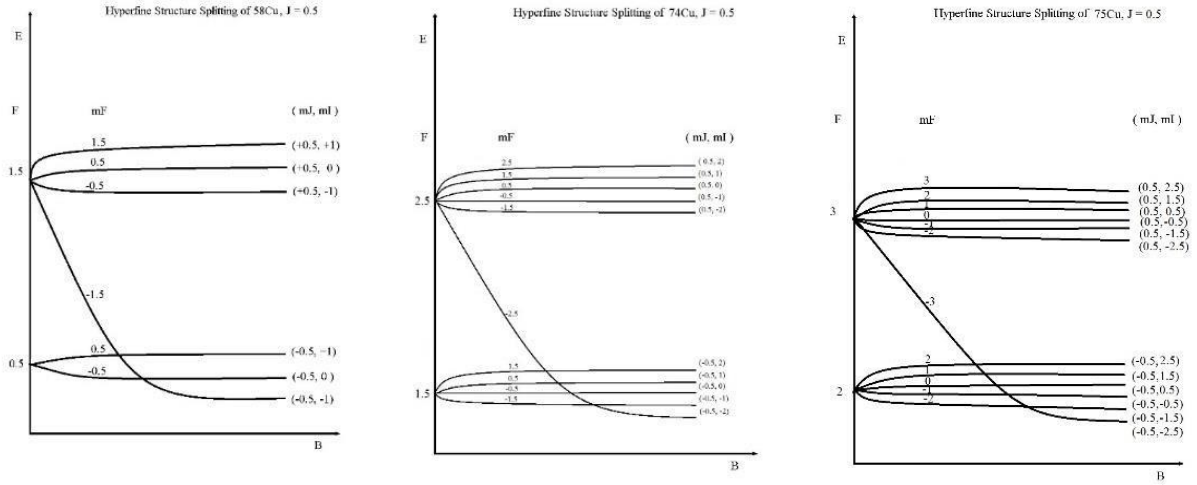
The nuclear polarization  $P$  is calculated by the equation

$$P = \frac{\sum_{m_I} m_I * N(m_I)}{I * \sum_{m_I} N_{m_I}}$$

where  $I$  is the spin of the nucleus and  $m_I$  (ranging from  $-I$  to  $+I$ ),  $N(m_I)$  is the population of the having a specific  $m_I$ , and  $\sum_{m_I} N_{m_I}$  is the total population.

The states are described by  $m_F$  ( $F = \text{total electron} + \text{nuclear spin}$ ,  $m_F$  being the corresponding magnetic quantum number in weak magnetic fields, and are described by  $m_J$  and  $m_I$  in stronger magnetic fields, as shown in the following energy splitting diagrams. These groupings were used to

assign  $m_J$  and  $m_I$  values to the populations to calculate the nuclear polarization. The populations of the  $m_F$  states were calculated using the atomic rate equations in the previous section with input parameters listed in the following section.



Figures 1-3: Hyperfine splitting of ground state of copper isotopes  $^{58}\text{Cu}$ ,  $^{74}\text{Cu}$ , and  $^{75}\text{Cu}$ .

### 2.3 OPTICAL PUMPING

The ground state of the copper atom is  $[\text{Ar}] 3d^{10} 4s^1$ , and the excitation of interest brings the electron from  $4s$  to  $4p$ . [Cop14]

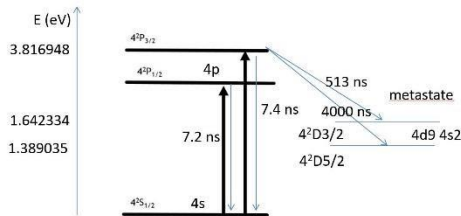


Figure 4: Fine structure splitting of copper.

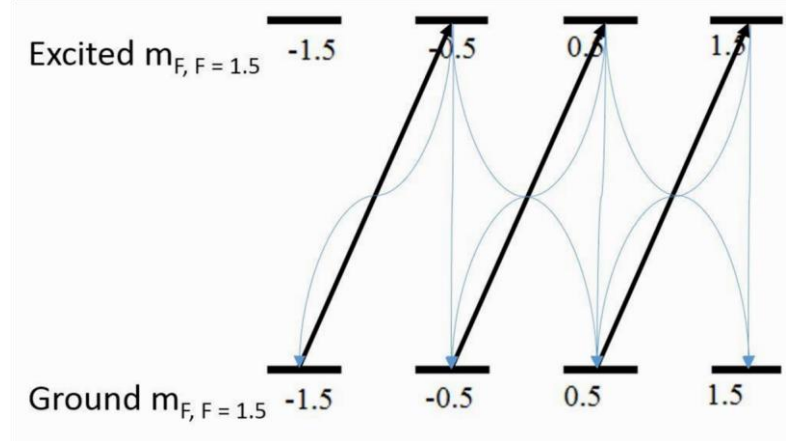


Figure 5: Optical pumping of  $^{58}\text{Cu}$ ,  $F = 1.5$ , with positively circularly polarized light. Bold arrows indicate excitations, while faded arrows indicate decay transitions.

Several input parameters are required, which are listed in the following section: the energy difference between the ground and excited states, the hyperfine structure constants, LS parameters, the lifetimes of the excited and metastable states, the spin of the nucleus, the laser power density, the polarization of the laser beam (positively or negatively circularized), and the time the ions interact with the laser.

The frequency corresponding to the energy difference of the upper transition ( $S_{1/2}$  to  $P_{3/2}$ ) is  $9.23 \times 10^8$  MHz, while the frequency of the lower transition ( $S_{1/2}$  to  $P_{1/2}$ ) is  $9.15 \times 10^8$  MHz, which

corresponds to an approximate wavelength of 320 nm, within the UV range. The lifetimes of the excited states, given by the inverse of the Einstein coefficient, are respectively 7.2 ns and 7.4 ns for the lower and upper transitions. [Kur95]

The metastable state for the upper transition has a lifetime of 513 ns, while the lifetime of the lower transition metastable state is 526 ns. [Kur95]

The hyperfine structure constants, A and B, vary for each fine-structure level, as well as each isotope. [Bra83] The hyperfine structure constants for the ground and excited states were taken from experimental data from ISOLDE [Vin10,11], while the constants for the metastable state were irrelevant to the calculations, and were arbitrarily set to zero. Research is ongoing to determine the hyperfine structure constant A for the lower transition.

*Table 1: Hyperfine structure constants for the ground ( $S_{1/2}$ ) and excited ( $P_{3/2}$ ), from experimental data. Note that  $B = 0$  when  $J = 1/2$ .*

Isotope	A ( $S_{1/2}$ )	A ( $P_{3/2}$ )	B ( $P_{3/2}$ )	Source
$^{58}\text{Cu}$	2257	77	-20	[Vin11]
$^{74}\text{Cu}$	-2113	-71.6	34	[Vin10]
$^{75}\text{Cu}$	1593	53	-36	[Vin10]

The LS parameters are consistent for all isotopes, as they depend only on the valance electrons, but do vary according to the upper and lower transitions. The total angular momentum (J) values are given in the Kurucz database, and the LS parameters were derived from normal quantum mechanical relation

$$\mathbf{J} = \mathbf{L} + \mathbf{S}$$

and the transition selection rule  $\Delta l = \pm 1$  for  $\pm$  circularly polarized light, where  $J$  is the electron total angular momentum,  $L$  is the orbital angular momentum, and  $S$  is the electron spin.

*Table 2: LS Parameters for the upper transition ( $S_{1/2}$  to  $P_{1/2}$ ).*

	<b>L</b>	<b>S</b>	<b>J</b>
Ground ( $S_{1/2}$ )	0	0.5	0.5
Metastable ( $D_{5/2}$ )	2	0.5	2.5
Excited ( $P_{3/2}$ )	1	0.5	1.5

*Table 3: LS Parameters for the lower transition ( $S_{1/2}$  to  $P_{3/2}$ ).*

	<b>L</b>	<b>S</b>	<b>J</b>
Ground ( $S_{1/2}$ )	0	0.5	0.5
Metastable ( $P_{3/2}$ )	1	0.5	1.5
Excited ( $P_{1/2}$ )	1	-0.5	0.5

Finally, the nuclear spin for each isotope is given in the table below.

Isotope	Nuclear Spin (I)
$^{58}\text{Cu}$	1
$^{74}\text{Cu}$	2
$^{75}\text{Cu}$	2.5

*Table 4: [Sta13], [Nat].*



## 2.4 INTERACTION TIME AND POWER DENSITY

The time that the ions interact with the laser, and the laser power density, are independent variables which may be changed to increase the nuclear polarization. The interaction time is calculated as a function of the ion beam velocity and the length of the apparatus. The copper ion beams at ISOLDE are produced at an energy of 60 keV, which will be polarized by a laser beam along a length of 2 m. The velocity of the ion beam is  $< 2\%$  of the speed of light, so the calculations are performed in the non-relativistic limit.

Table 5: Maximum interaction time for copper isotopes.

Isotope	Maximum Interaction Time ( $\mu\text{s}$ )
$^{58}\text{Cu}$	4.5
$^{74}\text{Cu}$	5.1
$^{75}\text{Cu}$	5.1

Another variable used to maximize the nuclear polarization is the laser power density: the power divided by the cross sectional area of the laser beam. The lasers used at ISOLDE are approximately 1-100 mW, and the cross sectional area may be changed by placing a lens in the beam's path to (de)focus it. For reference, 1 mW power with a 1 cm diameter beam would correspond to a power density of about  $10 \text{ W/m}^2$ .

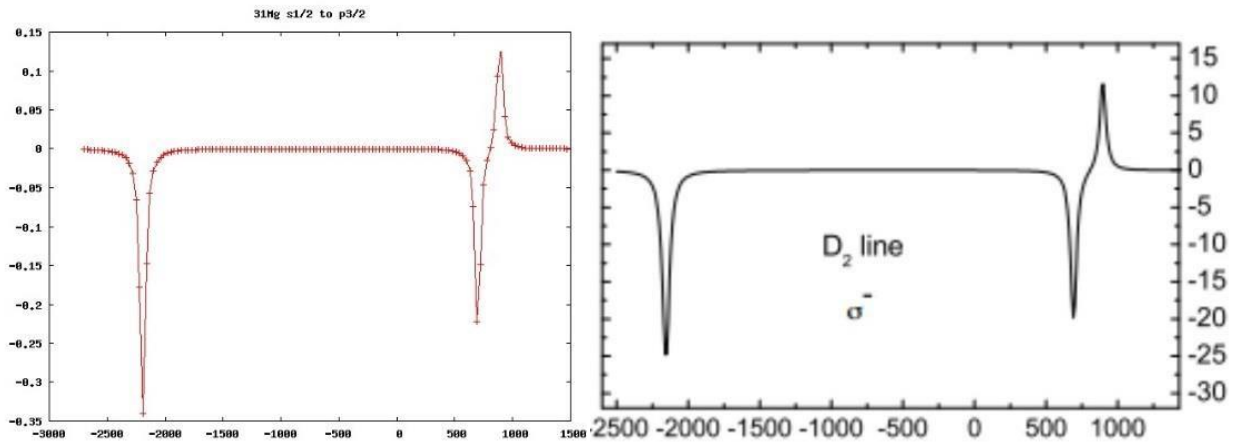
---

## 3. RESULTS

---

### 3.1 COMPARISON WITH PUBLISHED RESULTS

To verify the accuracy of the simulations, the code was programmed for  $^{31}\text{Mg}$ , and checked against published results based on the same code. From the figures below, it is clear that the simulations match publications that have been verified with experimental data.



Left: Figure 6: Simulation for negatively circularly polarized light for  $^{31}\text{Mg}$ . Right: Figure 7: Published graph of nuclear polarization as a function of frequency. [Kow06] (X-axes correspond to frequencies in MHz, while the y-axes correspond to the degree of nuclear polarization.)

The populations of the  $m_I$  levels, from which the nuclear polarization was calculated, were plotted as a function of frequency. The initial ground state populations were each normalized to 1, and it may be seen in the graph below that one state is depopulated as another state increases in population.

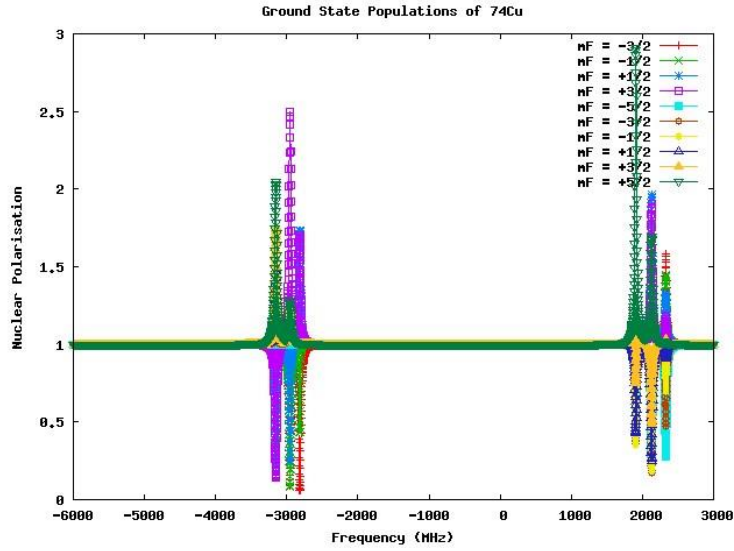
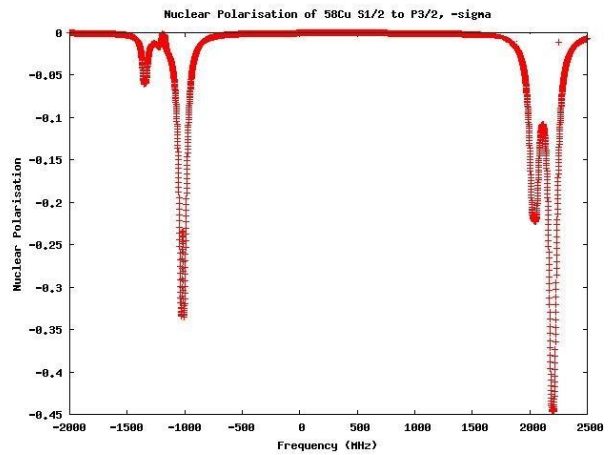
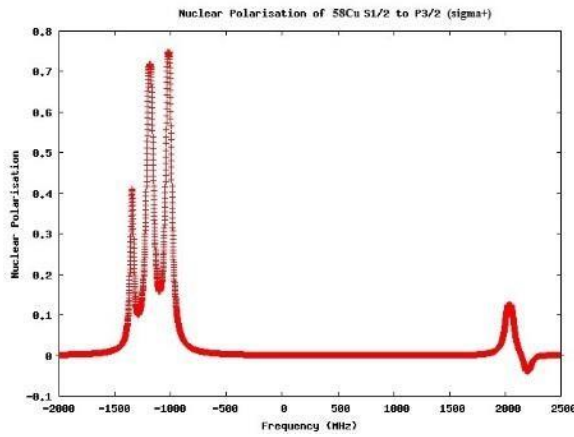
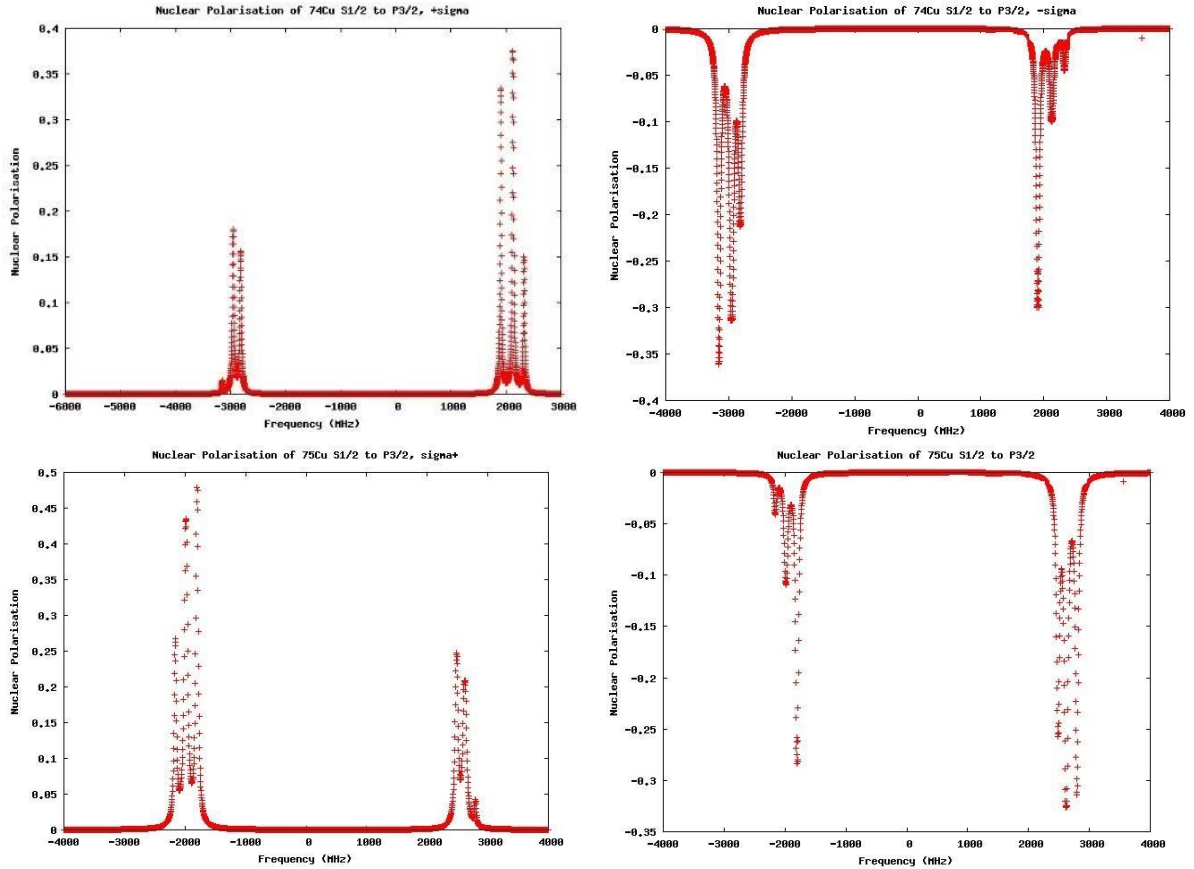


Figure 8: Ground State Populations of  $^{74}\text{Cu}$ .

### 3.2 NUCLEAR POLARIZATION OF $^{58}\text{Cu}$ , $^{74}\text{Cu}$ , AND $^{75}\text{Cu}$

Below are examples of nuclear polarization reached for all three isotopes with different polarization, with laser power density fixed to  $500 \text{ W/m}^2$  and each isotope's maximum interaction time for the upper transition ( $S_{1/2}$  to  $P_{3/2}$ ).

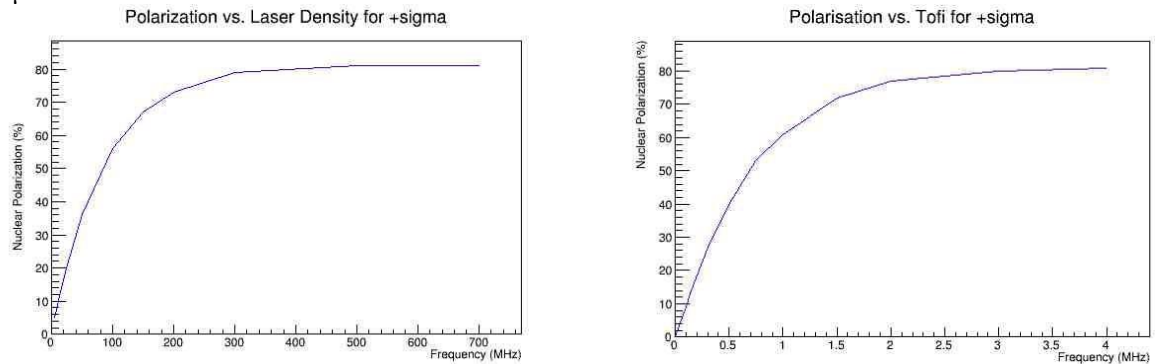




Figures 9-15: Simulations of nuclear polarisation of the upper transition for  $^{58}$ ,  $^{74}$ , and  $^{75}\text{Cu}$  with both positively ( $\sigma^+$ ) and negatively ( $\sigma^-$ ) circularly polarized light. Figures on the left correspond to positively circularly polarised light, while figures on the right correspond to a negative polarisation.

### 3.3 SATURATION PLOTS FOR LASER POWER DENSITY AND INTERACTION TIME

The nuclear polarization for the hyperfine-structure peak giving highest polarization was plotted as a function of the laser power density, as well as the interaction time for both positively and negatively circularly polarized light for  $^{58}$ ,  $^{74}$ , and  $^{75}\text{Cu}$ . Sample plots for positively circularly polarized light for  $^{58}\text{Cu}$  are shown below. From these plots, it is seen that the nuclear polarization reaches saturation when the power density approaches  $300 \text{ W/m}^2$ , and when the interaction time approaches  $3 \mu\text{s}$ .



Figures 16-17: Saturation plots of nuclear polarisation as a function of laser energy density and interaction time.

The remaining saturation plots are not shown here to reduce the length of this paper, but are available upon request at ISOLDE. Their results are summarized in the table below

Table 5: Nuclear polarization saturations as a function of laser power density and interaction time. Saturation is defined as within 2% of the asymptotic value.

Isotope	Polarization of Laser Beam ( $\pm$ sigma)	Nuclear Polarization at Saturation (%)	Saturation Laser Power Density ( $W/m^2$ )	Saturation Interaction Time ( $\mu s$ )	Frequency Offset from "Center of Gravity" (MHz)
$^{58}Cu$	+	75	300	2	-1000
	-	45	150	1.5	+2200
$^{74}Cu$	+	50	200	2	+2000
	-	37	400	3	-3200
$^{75}Cu$	+	47	300	3	-1800
	-	28	200	2	+2700

---

#### 4. CONCLUSIONS AND OUTLOOK

---

The highest nuclear polarization (75%) may be obtained using positively circularly polarized light with  $^{58}Cu$ , with a power density greater than  $300 W/m^2$  and an interaction time greater than  $2 \mu s$ , corresponding to the transition at -1000 MHz from the transition's center of gravity. The secondary highest nuclear polarization is achieved using positively circularly polarized light with  $^{74}Cu$  with a laser density greater than  $200 W/m^2$  and an interaction time greater than  $2 \mu s$ , corresponding to a frequency of approximately +2000 MHz from the center of gravity. Other variations had a nuclear polarization less than 50%.

#### 4.3 FUTURE

Once the hyperfine structure constant  $A$  is determined, simulations will be run for the lower transition ( $S_{1/2}$  to  $P_{1/2}$ ).

These simulations will be used to prepare the experiment studying the interaction of copper with biological compounds planned at CERN in the next five years. This project also lays the groundwork for optical pumping simulations of other elements, and may be used for the laser-spectroscopy experiment on zinc planned for fall 2014.

---

## 5. REFERENCES

---

- [Bra83] Bransden, B. H. and C. J. Joachain. *Physics of Atoms and Molecules*. London: Longman. (1983).
- [Cop14] “Copper.” *WebElements Periodic Table of the Elements*. N.p., n.d. Web. 10 June 2014.
- [Hem10] L. Hemmingsen et al., *Beta-NMR as a novel technique for biological applications*, CERN INTC-I-088 (2010).
- [Kow06] M. Kowalska, *Ground-state properties of neutron-rich Mg isotopes – the “island of inversion” studied with laser and  $\beta$ -NMR spectroscopy*, CERN-THESIS-2006047 (2006).
- [Kow08] M. Kowalska et al., *Nuclear ground state spins and magnetic moments of  $^{27}\text{Mg}$ ,  $^{29}\text{Mg}$ , and  $^{31}\text{Mg}$* , Physical Review C 034307 (2008).
- [Kur95] Kurucz, R.L., and B. Bell. *Atomic Line Data*, Kurucz CD-ROM No. 23. Cambridge, Mass.: Smithsonian Astrophysical Observatory (1995).
- [Nat] National Nuclear Data Center. Web. 1 June 2014. <http://www.nndc.bnl.gov/ensdf/>
- [Sta13] M. Stachura et al.,  *$\beta$ -NMR of copper isotopes in ionic liquids*, CERN INTC-P-393 (2013).
- [Vin11] P. Vingerhoets et al., *Magnetic and quadrupole moments of neutron-deficient 5862Cu isotopes*, Physics Letters B 703 34-39 (2011).
- [Vin10] P. Vingerhoets et al., *Nuclear spins, magnetic moments, and quadrupole moments of Cu isotopes from  $N=28$  to  $N = 46$ : Probes for core polarization effects*, Physical Review C 82, 064311 (2010).

---

## 6. ACKNOWLEDGEMENTS

---

A huge thank you to Dr. Magdalena Kowalska, who served as my advisor for this project and answered my incessant questions. Thank you also to Ronald Fernando Garcia Ruiz, who wrote the original starter code, and to Dr. Mark Lloyd Bissell who helped me with the energy splitting diagrams. Finally, thank you to Dr. Lawrence Sulak and Dr. Augusto Ceccucci for organizing the Boston University program at CERN.



# Analysis of $B^0$ and $B_s^0$ Lifetime Differences Using Kinematic Weighting

Kirby Hermansen

2014 Boston University Geneva Program University of Notre Dame  
LHCb Semileptonic Working Group

Diego Tonelli (CERN), Angelo Di Canto (CERN)

30 June 2014

---

## ABSTRACT

---

The Particle Data Group accepted mean lifetime measurement for  $B_s^0$  is  $1.516 \pm 0.011$  ps, for a precision of roughly 0.7%. Here is presented an alternative method of measuring the lifetimes of  $B_s^0$  and  $B^0$  mesons using kinematic variable weighting and acceptance ratio calculations. These calculations are done in Monte Carlo simulation to test efficiency of the proposed technique. Future zero-tests must be conducted on data to approve the technique before implementation.

## 1 BACKGROUND

### 1.1 CONCEPT

$B$  mesons occur in a number of different varieties, but here we will only focus on  $B_s^0$  and  $B^0$  particles and one specific decay of each.

$$B_0 \rightarrow D-\mu+\nu \rightarrow K+K-\pi-\mu+\nu \quad (1)$$

$$B_{s0} \rightarrow D_s-\mu+\nu \rightarrow K+K-\pi-\mu+\nu \quad (2)$$

In Monte Carlo simulation, the entire decay can be reconstructed to yield the ‘true’ particle kinematics. However, in practice the neutrino is undetectable and introduces a biasing factor that must be corrected.

Using these decays, the mean particle lifetime can be found through either direct measurements or ratio measurements, where, in the latter, the lifetime of the measured particle is compared to a second particle. Direct measurements introduce large systematic uncertainties due to the nature of the calculations. However, a ratio measurement eliminates many of these uncertainties as they are present in both particle measurements. This correction, though highly useful, does introduce a number of additional factors that must be corrected. The ratio is calculated as follows

$$R(t) = \frac{N_{B_s^0}(0) \times G(t) * e^{-\frac{t^{corr_s}}{\tau_s}} \times A_{B_s^0}(t)}{N_{B^0}(0) \times G(t) * e^{-\frac{t^{corr}}{\tau}} \times A_{B^0}(t)} \quad (3)$$

where  $t^{corr_s} = k_{B_{s0}} \times t$  and  $t^{corr} = k_{B0} \times t$  (the k-factors correspond to a correction for the missing neutrino),  $N_{B_{s0}}(0)$  and  $N_{B0}(0)$  are the decays at  $t = 0$ ,  $A_{B_{s0}}$  and  $A_{B0}$  are the acceptance factors, and finally,  $G(t)$  is the resolution in measuring decay times. In this study we are only concerned with acceptance factors. The problems that necessitate the acceptance factor correction (as will be discussed in the next section) are physical detector biasing corrections for true lifetime differences and kinematic variables.

## 1.2 CHALLENGES

The problems presented in the acceptance factor correction are clear:

- i) Calculate the correction ratio for the difference in true lifetimes.
- ii) Calculate the corrections for differences introduced by decay kinematics.

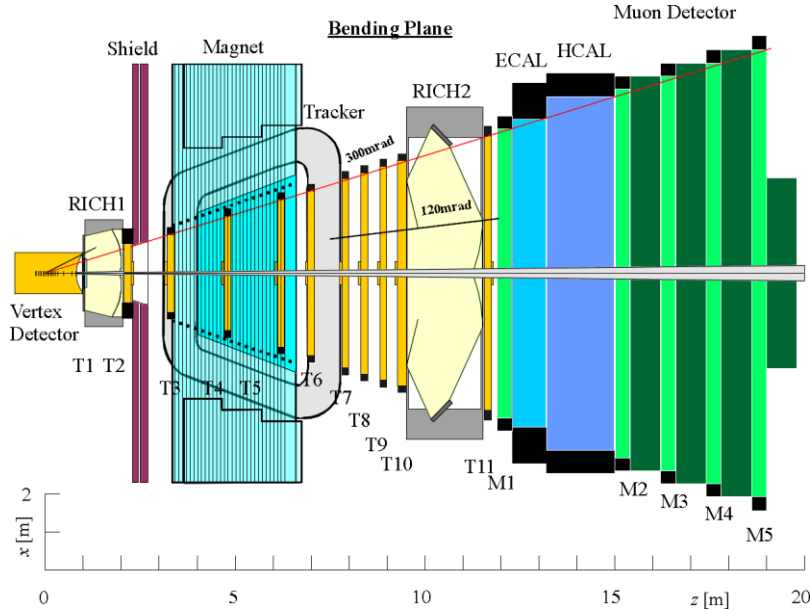


Figure 1: Side view of the LHCb detector.

These corrections arise from the physical setup of the detector (Fig.1), as decays occurring either after or before the various detectors (e.g. Vertex Detector (VELO)) will not be identified or recorded. This biases the results as the detector only selects a certain number and variety of decays. The immediate difference in mean lifetimes of the  $B$  particles present one biasing factor already. Additionally, variations in decay kinematics (e.g. particle momenta, masses, decay angles, etc.) bias the results as the kinematics can cause the decay to occur outside the detectable range and eliminate the decay from record. Clearly, the lifetime ratio must be corrected according to both of these variations.

## 2 ACCEPTANCE STUDIES

In ideal conditions, where the detector identifies every residual particle from every decay, we would have no need of incorporating any kind of correction into our model ratio. However, physical limitations necessitate the implementation of these corrections. The detector does not identify every particle, as the decay path may result in a particle passing undetected. This is due to kinematic variables in the  $B$  particle and its resulting daughters. This section addresses these issues.

### 2.1 RELATIVE ACCEPTANCES

To begin, the  $B$  decay time itself biases the acceptance in the detector. If the  $B$  decays too quickly or too slowly it can pass undetected or incorrectly detected. However, knowing how many decays are expected in a certain interval can be used to eliminate or at least



mitigate this problem. Using a bin-by-bin ratio of true decay times of the accepted  $B_s^0$  and  $B^0$  candidates, we can approximate the acceptance rate as follows:

$$P(t) = \frac{P_{B^0}(t)}{P_{B_s^0}(t)} = e^{-t\left(\frac{1}{\tau_d} - \frac{1}{\tau_s}\right)} \quad (4)$$

where  $P(t)$  is the probability density of the decays, and  $\tau_s$  and  $\tau_d$  are the known mean lifetimes of  $B_s^0$  and  $B^0$  respectively.

Applying this correction factor to the distribution ratio—a simple division of the distributions  $B_s^0$  by  $B^0$ —results in the ratio of acceptances seen in Fig.2. The important statistics of the linear fits of the ratios are listed in the legends, and are as follows:

- $\chi^2/ndf$ : the  $\chi^2$  value divided by the degrees of freedom of the fit
- p0 : the  $y$ -intercept of the fit
- p1 : the slope of the fit

The goal of eliminating biases to reduce the ratio to one is then manifested in the analysis by a small  $\chi^2/ndf$ , a p0 close to one, and a p1 close to zero. It must be noted that Fig.2 shows the corrections actually *reversed* progress towards this goal. However, the correction implemented here is not designed to improve in this regard but rather to cancel out biasing due to  $B$  decay time acceptances. The main progress is made in the next section.

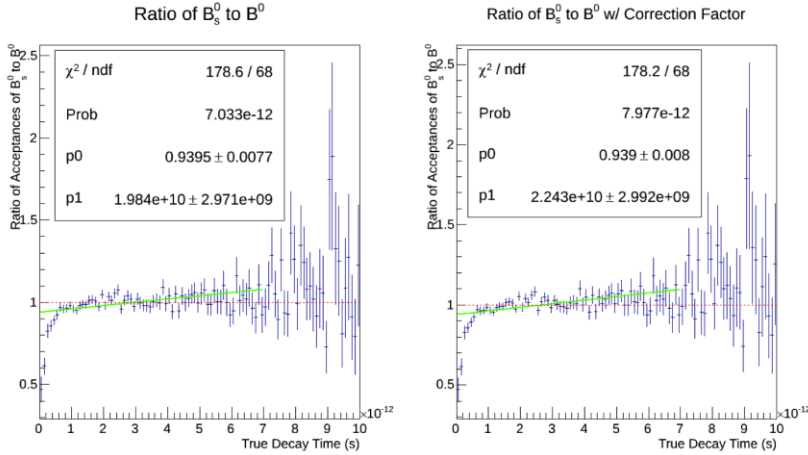


Figure 2: Ratio of acceptances before (left) and after (right) corrections

## 2.2 WEIGHTING

Ideally, with no background and identical acceptances between  $B_s^0$  and  $B^0$  decays, *only* a difference in lifetime would cause a difference in decay time distributions between  $B_s^0$  and  $B^0$ . However, other deviations arise from differences in many kinematic variables, namely momenta, masses, and lifetimes of the particles involved in the decay chain. We propose to mitigate these differences by weighting the  $B$  decay time distributions according to these variable differences. As examining every possible variable difference would be highly inefficient, we will select one primary variable on which to base our weighting, and add a secondary variable to refine it.

### 2.2.1 PRIMARY WEIGHTING

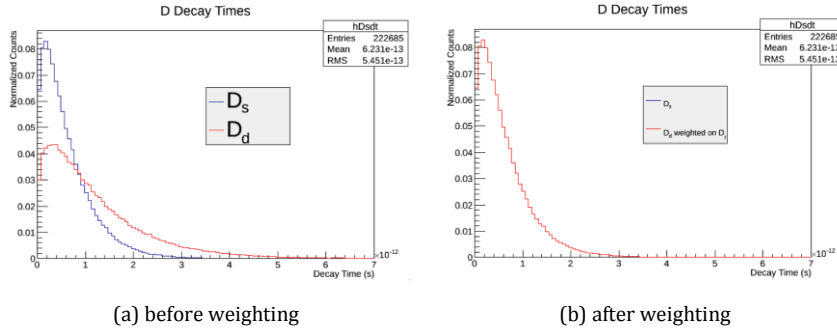


Figure 3: *D* decay time distributions

As seen in Fig.3(a), the difference in decay time distributions between  $D_s^-$  and  $D^-$  is quite drastic. We choose this variable as the basis for our weighting.

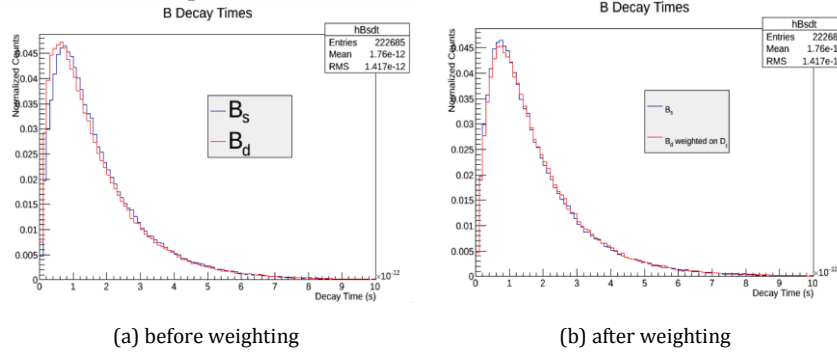


Figure 4: *B* decay time distributions

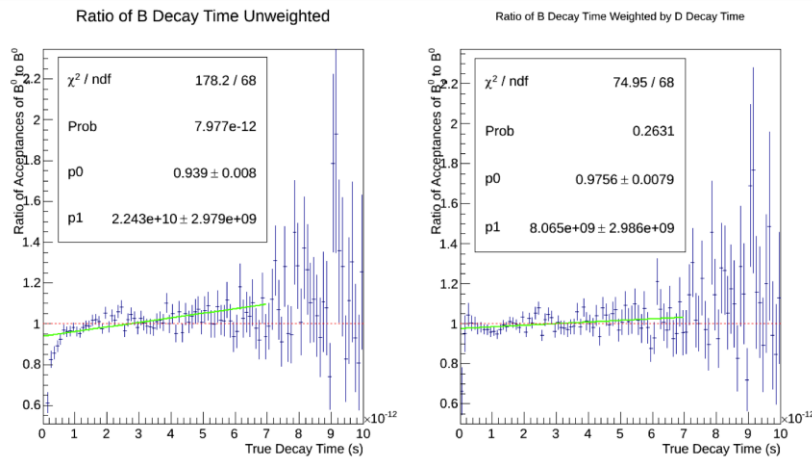


Figure 5: Ratio of acceptances before (left) and after (right) *D* decay time weighting

The weighting process is quite simple. The *D* decay time distributions are divided and the values corresponding to each entry are recorded (a verification of this process is exhibited in Fig.3(b)). When the entry is used to fill the *B* decay time distribution, the value for that entry is recalled and used to weight the entry. This effect can be visibly seen

in the difference between the unweighted  $B$  decay time distributions (Fig.4(a)) and the weighted counterpart (Fig.4(b)).

These newly weighted distributions are then used to find a new ratio of acceptances which can be seen in Fig.5.

## 2.2.2 SECONDARY WEIGHTING

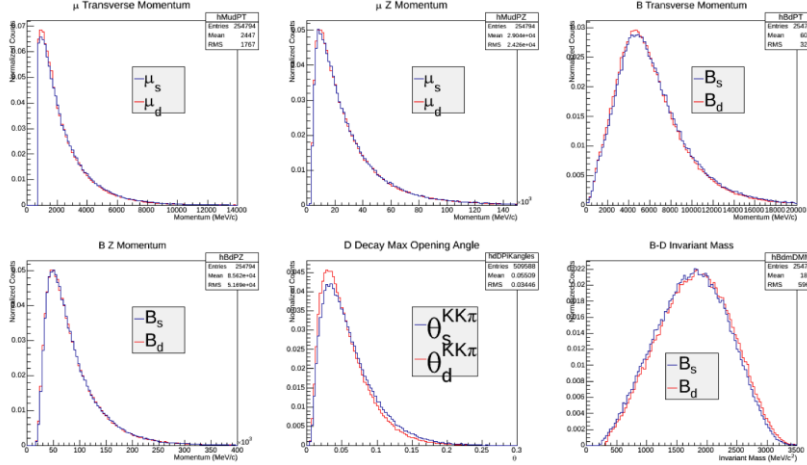


Figure 6: Variable candidates for secondary weighting

Now that a primary weighting variable is established, attention can be directed towards identifying a secondary weighting variable to further refine the process. In order to use a second weight, it is first necessary to verify that the variables are independent of the primary weight, or else it would be possible that the correction is being biased further. In order to confirm independence, each of the variables in the following section had their distributions weighted as in the previous section, and then the weights were multiplied by the  $D$  decay time weights and the effect was examined. If the resulting multiply-weighted distribution differed significantly from the singly-weighted distribution, the variables are *not* independent. However, the six variables in the discussion that follows were each independent of the  $D$  decay time.

Fig.6 shows these six possible variables, selected based on their presumed impact on  $B$  decay time. The first four (momenta of the  $\mu$  and  $B$  particles) are straightforward variables and have a clear impact as the direction and speed of a particle can change how it is detected. The fifth variable ( $D$  decay maximum opening angle) is calculated by finding the opening angle between the  $D$  particle and its daughter particles and taking the maximum angle found. This impact is again clear as the angle in which the  $D$  decays has a significant effect on the detection of the daughter particles (i.e. a smaller or larger angle could mean a particle escapes detection). The sixth variable ( $B$ - $D$  invariant mass) is calculated by simply taking the difference of the reconstructed (missing neutrino) invariant masses of the  $B$  and  $D$  particles. This has an impact similar to momentum as the mass affects the energy and therefore the momentum. Of the six variables, the only one to stand out with a significant difference between  $B_s^0$  and  $B^0$  is the maximum opening angle.

The weights corresponding to these six variables are then individually

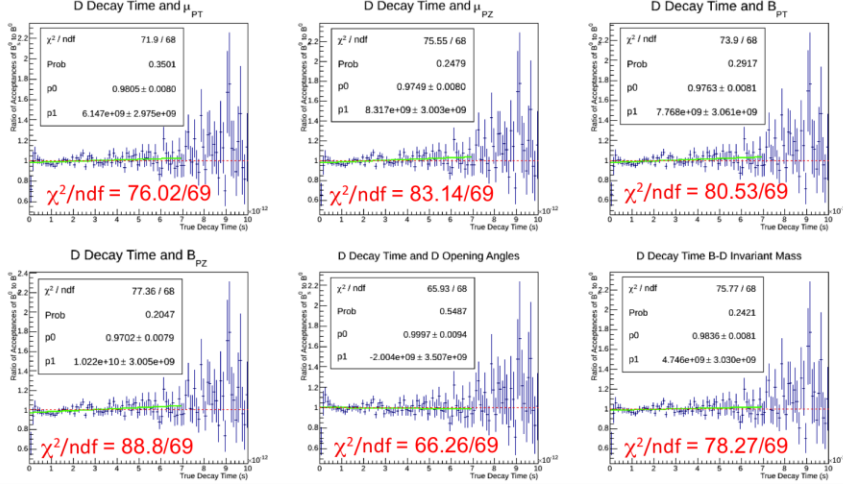


Figure 7: Ratios of acceptances weighted with  $D$  decay time and various secondary weights

multiplied by the  $D$  decay time weights to produce the complete secondary weight for each respective event. The resulting distribution (Fig.7) is corrected for lifetimes and divided by the same means as above to produce the ratio of acceptances.

Clearly, the  $D$  decay opening angles is the best variable for a secondary weighting technique. The  $y$ -intercept ( $p_0$ ) is within the error of one, the slope ( $p_1$ ) is within the error of zero, and the  $\chi^2/ndf$  of the distribution when fit to a fixed horizontal line at  $y = 1$  is less than one. Only this particular secondary variable performs so well in all of the criteria.

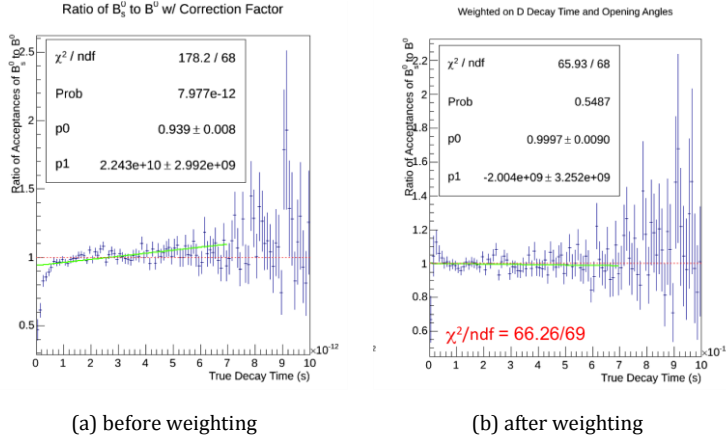


Figure 8:  $B$  decay time distributions

### 3 CONCLUSIONS

After all of the corrections, the ratio of acceptances is significantly close to one. In comparison with the initial ratio of acceptances (Fig.8(a)), the final result (Fig.8(b)) demonstrates marked improvement. This weighting technique can now be implemented on data and zero-tested to be used in verifying the  $B_s^0$  and  $B^0$  lifetime differences.

However, it is important to note that the weighting and acceptance calculation is only a small part of the ratio introduced by Eq.3 and further work needs to be done investigating the background and k-factor corrections to reach a more complete and satisfying conclusion.

# NA62 Liquid Krypton Electronics

Matthew Huszagh  
BU PY392: Directed Study at CERN  
Supervisor: Stefano Venditti

## Abstract

The NA62 experiment begins data acquisition in October of 2014. As a result, everything must be completely installed and thoroughly tested for functionality by October. I wrote algorithms in ROOT to ensure that the acquisition system for the liquid krypton calorimeter met certain minimum quality specifications. I found that the calorimeter readout modules met the specified noise parameters, but failed the specifications for coherent and non-coherent noise. Since our test data was acquired through signals generated by the electronics and not by particles passing through the liquid krypton tank, we intend to re-perform these quality tests when we are receiving data directly from the tank.

## Introduction

The aim of the NA62 experiment is to study the rare  $K^+$  meson decay into a  $\pi^+$  meson and a neutrino/antineutrino pair. The experiment hopes to achieve a more precise measure for the probability of a top quark decaying into a down quark,  $|V_{td}|$ .

The experiment receives protons of 400 GeV/c from the Super Proton Synchrotron at CERN. The high-energy protons collide with a beryllium target at the starting end of the 270 meter-long track, producing a hadron beam of 800 MHz. Because the decay is so rare, the experiment only hopes to obtain roughly 80 data points during 2 years of data collection. In order to extract only the appropriate data, the experiment employs numerous veto detectors and relies on an extremely accurate temporal resolution of 150ps.

My work on the NA62 experiment began in March of 2014, with data taking scheduled to begin in October. As a result, my work was focused around preparations for data taking. Specifically, I worked on the Liquid Krypton calorimeter, a photon veto detector employing low-noise electronics and the capability to handle immense data loads. Because of these stringent requirements, my responsibility was largely to ensure that the electronics met the specified criteria. Additionally, I took part in the electronics installation process at the experiment site.

## Materials and Methods

The liquid krypton calorimeter is a 10m<sup>3</sup> liquid krypton (LKr) tank with numerous preamplifiers inside. Particles in the forward direction pass through the tank and deposit their energy by ionizing the liquid krypton. The electrons originating from the ionization are free to drift in the in the liquid krypton and induce an electric signal which is then amplified and shaped into a bipolar pulse shape (AC signal) digitized by the calorimeter readout modules (CREAMs). The conceptual schematic of the electronics chain is shown in Fig 1.

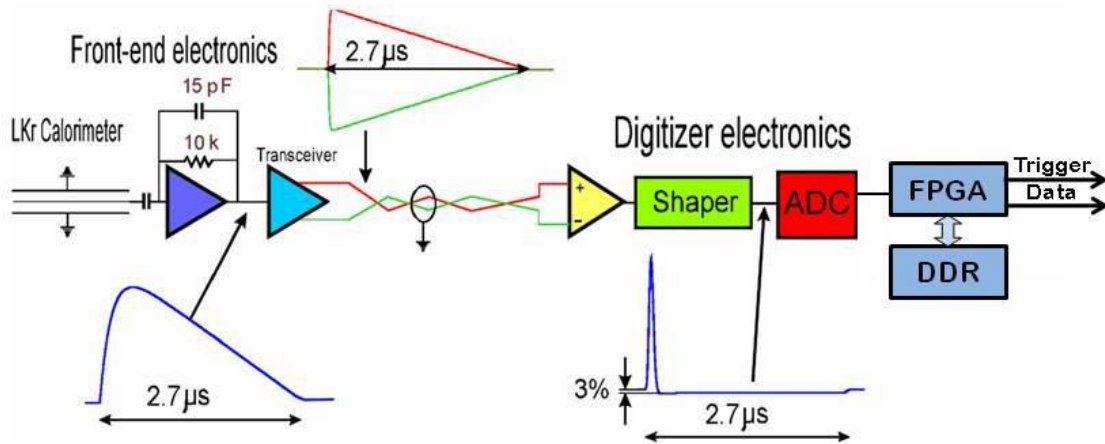


Figure 1: A conceptual schematic of the NA62 calorimeter electronics.

The CREAMs are organized in crates of 16 CREAMs with 8 columns of 4 crates. Each CREAM receives the input AC signal from 32 channels, where each channel corresponds to a preamplifier in the LKr tank. They convert the AC signal into a digital code and place the digitized signal in a circular buffer. A level 0 (L0) trigger is then applied through the backplane of the crate and moves data which passes an initial selection criteria to the L0 buffer. Since the PC farm (where the data will ultimately be stored and analyzed) will be inundated with so much data, the L0 trigger allows us to only extract the data corresponding to a particle depositing energy in the tank and discard the data gathered when no particles are moving through the tank. A level 1 (L1) trigger is then sent by the PC farm through a Multi-Request Packet (MRP) to each crate. The L1 trigger discards insufficiently relevant data which was not discarded by the first trigger. The data that has passed both triggers is then sent out by Ethernet ports to a 10Gbit switch where the data from each crate is aggregated and sent to the PC farm for storage and analysis.

One of my tasks was to adjust the signal baseline in real time. The AC signal is digitized into 14 bits, corresponding roughly to 16,000 voltage counts. Without any adjustment the signal comes in at about 8,000 counts (approximately  $\frac{1}{2}$  volts). However, the difference between the baseline of a signal and its peak is approximately 15,600 voltage counts (ADC), so the baseline needs to be readjusted to around 400 ADC in order to collect the entire signal. Additionally, there is an undershoot after the peak so we cannot simply adjust the signal to 0 ADC. The baseline needs to be readjusted continually because the voltage is affected by various uncontrollable variables, such as humidity. I wrote an algorithm which recognizes when a new data file is created by the CREAMs and extracts the baseline. The algorithm then adjusts the baseline by the difference between the old baseline and 400 ADC and re-extracts the new baseline. It then repeats this process until the baseline is within 1 ADC of 400 ADC.

Another important task I had was to verify that the signal noise was sufficiently small. To do this, I wrote an algorithm to extract and plot the sigma values (corresponding to the RMS deviation of the voltage counts) of each channel of every CREAM.

My last task was to readapt existing code to compute the coherent and non-coherent noise for many CREAMs (the previous code only did this for a single CREAM). I extracted values for the coherent and non-coherent noise from all channels and plotted the values in a histogram.

## Results

I found the mean sigma value to be within the minimum specification parameters of 2 ADC. The tested mean sigma value was 1.2 ADC.

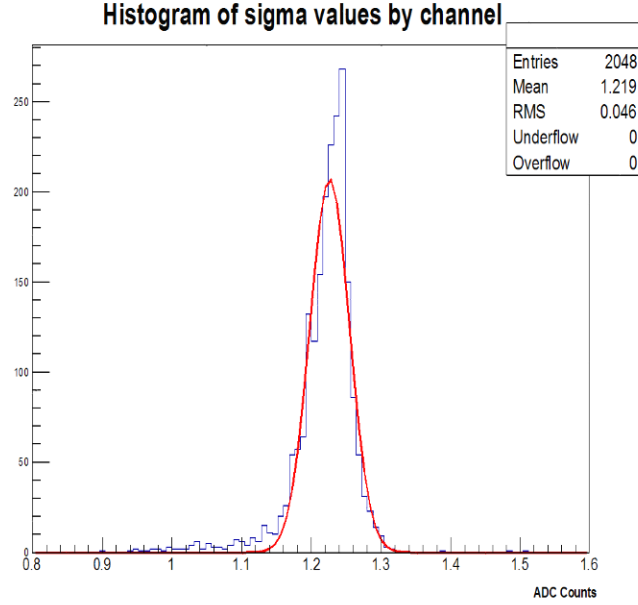


Figure 2: A histogram of the total noise from each channel of 4 crates.

The specifications for coherent and non-coherent noise were that coherent noise should be less than 2 ADC and less than 10% of non-coherent noise. Non-coherent and coherent noise were computed as follows:

$$\sigma_{NCOH} = \frac{\sigma_D}{\sqrt{32}} \quad \sigma_{COH} = \frac{\sqrt{\sigma_S^2 - \sigma_D^2}}{32}$$

Here,  $\sigma_S$  gives the computed sigma of the sum of the 32 channels for all CREAMs of 4 crates.  $\sigma_D$  gives the computed sigma of the difference of the last 16 channels from the first 16 channels for all CREAMs of 4 crates.

Contrary to the specifications and earlier tests for a single CREAM, I found coherent noise to be around 0.2 ADC, which is greater than 0.1% of the non-coherent noise (1.2 ADC).

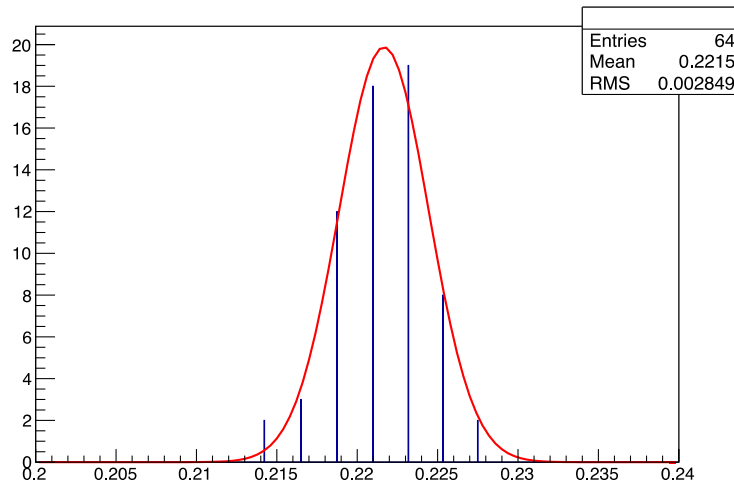


Figure 3 Coherent noise

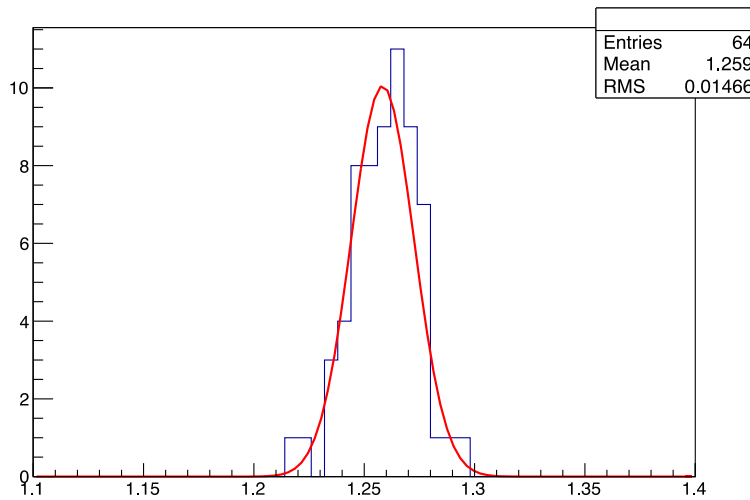


Figure 4 Non-coherent noise

## Discussion

While the coherent noise result seems to indicate insufficiently accurate CREAMs, the data were generated by preamplification signals intended to mimic a real signal. The data were not generated from real ionization signals picked up by the preamplifiers in the LKr tank. So, we intend to perform the same algorithm on real data before making conclusions about the quality of the CREAMs, especially since the CREAMs passed all previous quality tests.

In the next couple weeks, we expect the cooling system to be completely functional. At this time, we can turn on the crates permanently and perform our tests on real data input from the LKr tank.



# Antiprotonic Lithium ( $\bar{p}\text{Li}^+$ ):

Optimal Detection Through Simulation

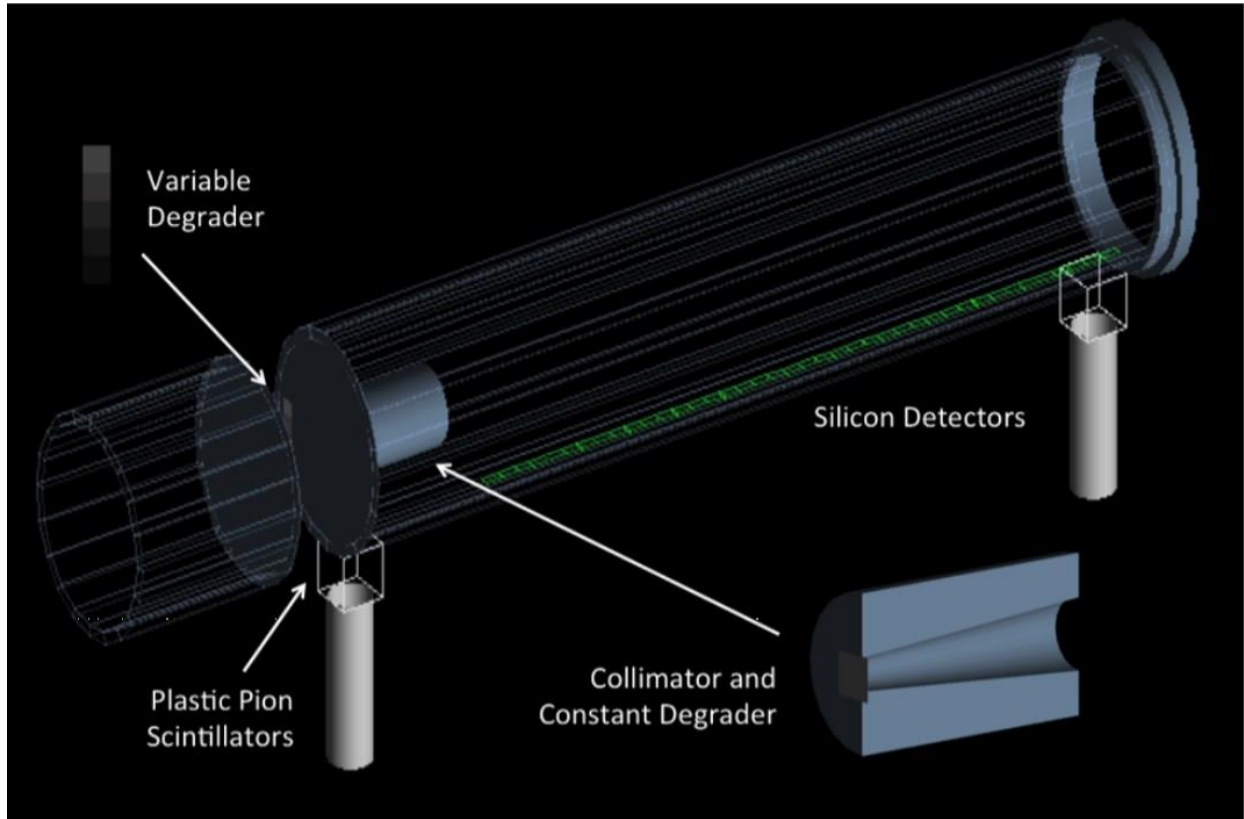
Logan Kageorge, Conrad Roman

Boston University

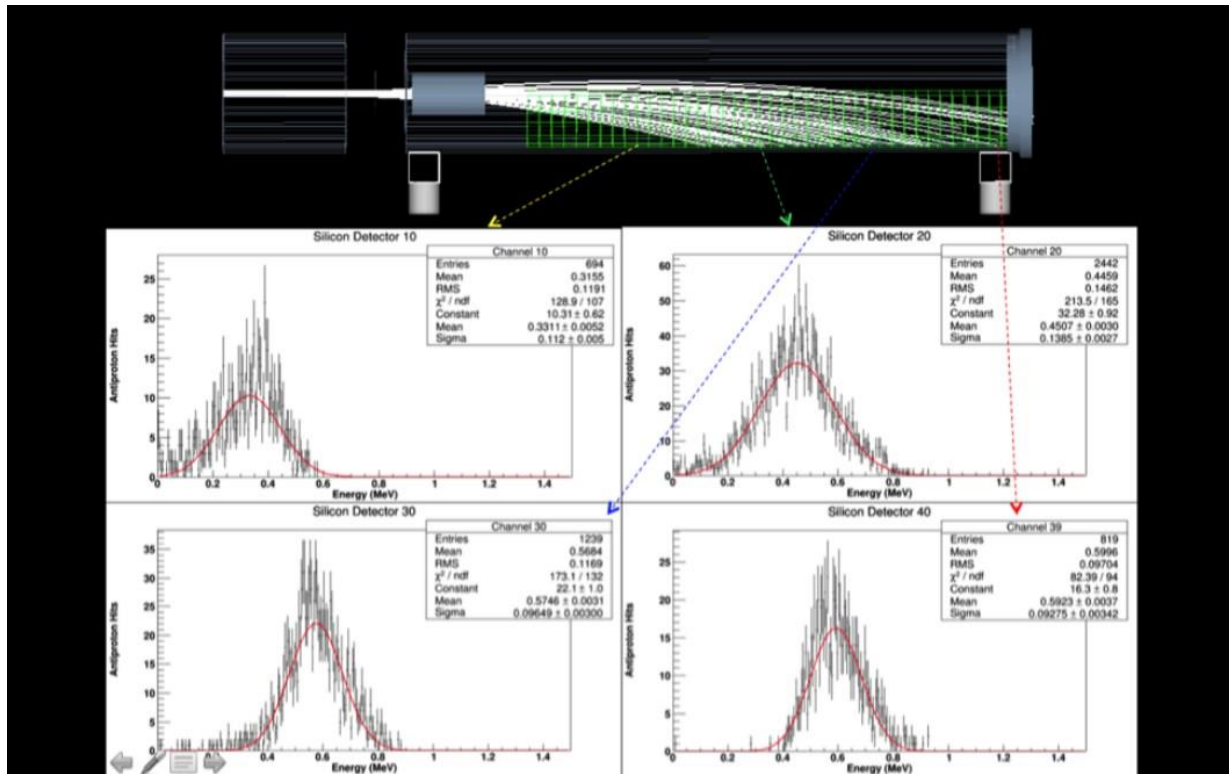
For the last semester, the two of us have worked to simulate the construction of several different experiments for installment on the ACE beam line, which runs parallel to that of the AEGIS project. The ACE beamline will be utilized during the times when the AEGIS experiment is not operating. Through our studies, we have learned a great deal about programming in C++ while utilizing Geant4, a powerful physics simulator. However, to fully grasp the performance of our simulations, we first needed to understand the basics of Monte Carlo simulation, detector functionality, metastable exotic antiprotonic atoms, and magnetic field construction.

To study the properties of antimatter, we utilize the Antiproton Decelerator program at CERN, which in August 2014 will supply a monochromatic beam of antiprotons with momentum of  $105 \text{ MeV}/c$ , or  $5.3 \text{ MeV}$  of kinetic energy. For the best analysis of various antiproton properties, we want to cool the incident beam with foil degraders into the range of  $1 \text{ eV}$  to  $100 \text{ keV}$ . We investigated the use of a variable degrader to allow the specification of energy within this range.

At the beginning of this project, we first built up our experimental environment based on descriptions given to us by our mentor, Michael Doser. At first, this consisted of a few key components: the steel beam housing to prevent escaping particles, a small air gap to separate the experiment from the AD beam line, two degraders (a variable degrader in discrete steps made of aluminum foil and one constant degrader made of aluminum or lithium), a titanium collimator, and the main vacuum chamber. Later, two scintillators were placed just outside underneath the beginning and end of the vacuum chamber to detect pions emitted in antiproton-proton annihilations, along with a silver bromide emulsion setup at the very end of the chamber to detect larger particles. All alterations to the vacuum chamber geometry were made for financial accessibility and ease of disassembly for emulsion analysis.



In order to determine the energy spreads that we were detecting for any given degrader setup, we utilized a uniform magnetic field and a silicon strip detector. Forty silicon channels were placed along the full interior length of the chamber. After being scattered by the variable degrader in the air gap and the constant degrader in the vacuum chamber, the antiprotons were collimated and deflected by a 0.1 Tesla magnetic field toward the silicon channels. When plotting the kinetic energy of the antiprotons in a one dimensional histogram, we saw that the energy distributions were near perfect gaussians, with the mean energy increasing as we looked to channels further down the chamber. These gaussians were exactly what we wanted since the antiprotons were being angularly scattered into a conical shape. Once the physics of the simulation was established, it was easy to manipulate the degrader widths to find the optimum width combinations.




---

## CONRAD

---

The steps needed to create  $pLi^+$  are as follows: degrade and collimate the incident  $p$  beam into our desired energy range ( $KE \approx 100keV$ ), and have that beam strike a  $Li$  foil near the end of the chamber. This energy has been chosen as the energy most likely to produce the  $pLi^+$  in a metastable state characterized by the antiproton's principle quantum number,  $N$ , being very high ( $\approx 60$ ). The  $p + p$  annihilations will create a distribution of daughter particles, mainly  $\pi^+ \pi^-$  and  $\pi^0$ , whose ionizing radiation we can detect with the two scintillators. Since  $pLi^+$  is an potentially metastable exotic atom consisting of a matter-antimatter pair, its lifetime is characterized by the amount of time it takes for the  $p$  to spiral inwards and annihilate with the nucleus. This will create its own delayed annihilation signal separate from the  $p$  annihilations with the  $Li$  foil at the far scintillator.

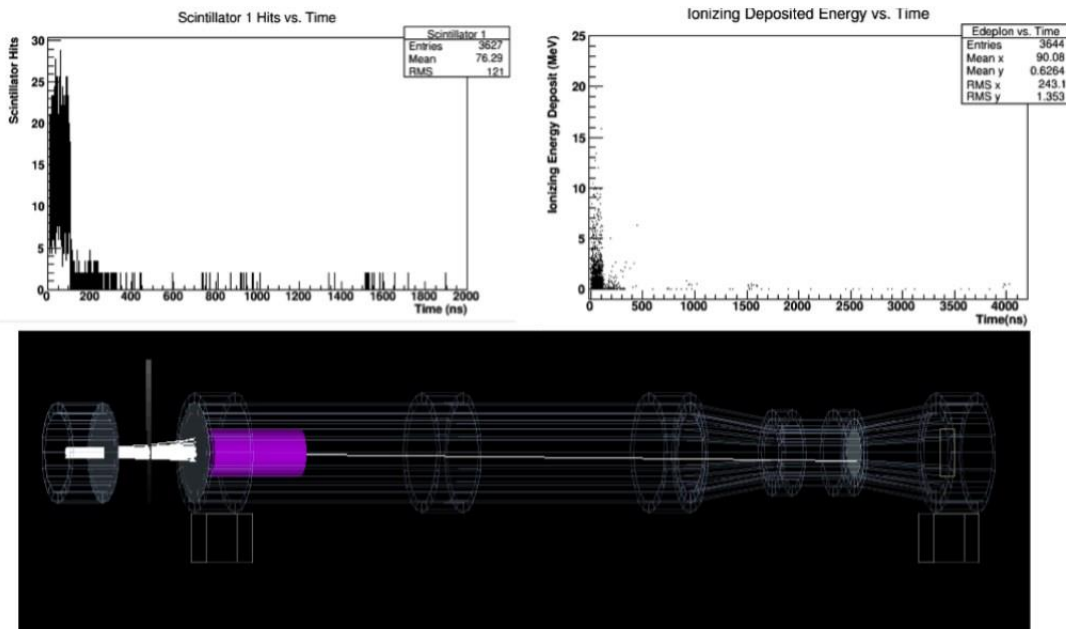
To detect the annihilations of antiprotonic atoms, we placed a  $125\text{ cm}^3$  ( $5 \times 5 \times 5\text{ cm}$ ) plastic scintillator cube underneath the emulsion at the back of the vacuum chamber. We chose polyvinyl toluene doped with anthracene as our scintillation material. These metastable atoms have a theoretically calculated average lifetime of  $3\ \mu\text{s}$ . For this scintillator to be able to detect the signal produced by the annihilation of these exotic atoms, we need the scintillator signal from all other particles to die off significantly before  $3\ \mu\text{s}$  have passed. This way, we can distinguish the signal coming from antiproton annihilations from the signal created when the exotic atom decays.

To do this, I simulated a scintillator signal and analyzed the signal vs. time distributions for various degrader thickness combinations that produce antiprotons in our desired energy range for the exotic atom creation. The way that Geant4 handles scintillation is fairly straight forward: the scintillation signal comes from "optical photons", which are created in number proportional to the amount of ionizing energy deposited in the scintillation plastic by a particle passing through it. But, this process requires a lot of computing power (which I do not have), so I chose to instead substitute the optical photon signal (number of optical photons created vs. time) for an ionizing energy deposit signal

(ionizing energy deposited vs. time). Also, the individual time components of each energy deposition were uniformly randomized by adding a random time from 0 nanoseconds to 200 nanoseconds to recreate the fact that the AD provides the antiprotons in 200 nanosecond bunches.

After plotting these two dimensional histograms, I found that the bulk scintillation signal occurs in the 0 to 0.5 $\mu$ s range, and seems to decay significantly after 1.5  $\mu$ s. Since the exotic atoms are estimated to have a mean lifetime around 3  $\mu$ s, we would hope for the signal to diminish before this point. Unfortunately, I found that it is not quite possible to have the signal completely diminish by this time, but the ionizing energy deposit after the 1.5  $\mu$ s point is almost always very small (on the order of 1-20 eV). There are often very low energy deposits in the scintillator, but rarely above 300 keV. It seems that any kind of bulk scintillation signal resulting from the exotic atom decay past the 1.5  $\mu$ s time would be significant and distinguishable from the background.

Analysis of various thickness combinations of the variable and internal degraders led me to determine that an internal degrader in the 115-120  $\mu$ m range, with a variable degrader varying from 5-45  $\mu$ m would be an optimal combination. The specific choice of internal degrader thickness depends on what energies we specifically want the mid-degrader thickness to create. In the simulation, I created a 10-step variable degrader so that I could modify the thickness in 5  $\mu$ m steps, but I do not know if this financially logical. So, it may make more sense to have 5 steps varying by 10  $\mu$ m each (5, 15, 25, 35, 45  $\mu$ m), in which case I found that an internal degrader thickness closer to 115-117  $\mu$ m would be optimal.



In the future, there is not much more to do with this specific analytical part of the project, unless access to a larger amount of computing power is available and the “optical photons” can be simulated. Since this will be an ongoing experiment, there will always be opportunity for people in the future to utilize the same simulating toolkits as we have to optimize various parameters that are yet unforeseen, or attempt to design new intriguing experiments based off this design. Learning the Geant4 toolkit can be a priceless skill for any physicist, whether it be for practical purposes, or just for exploring curious physical situations for fun.

---

## LOGAN

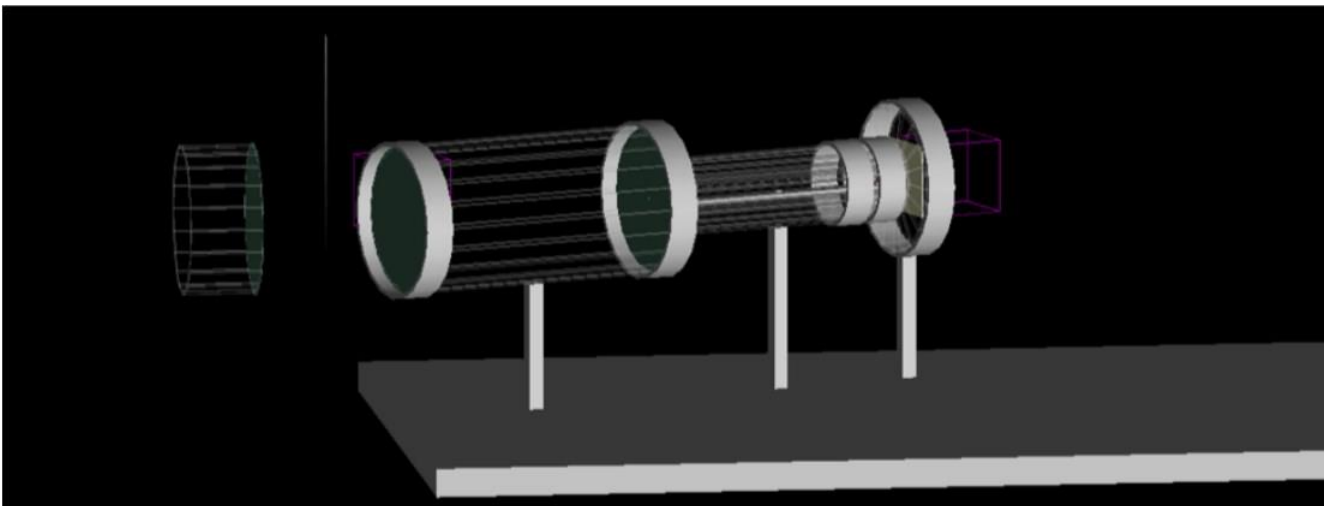
---

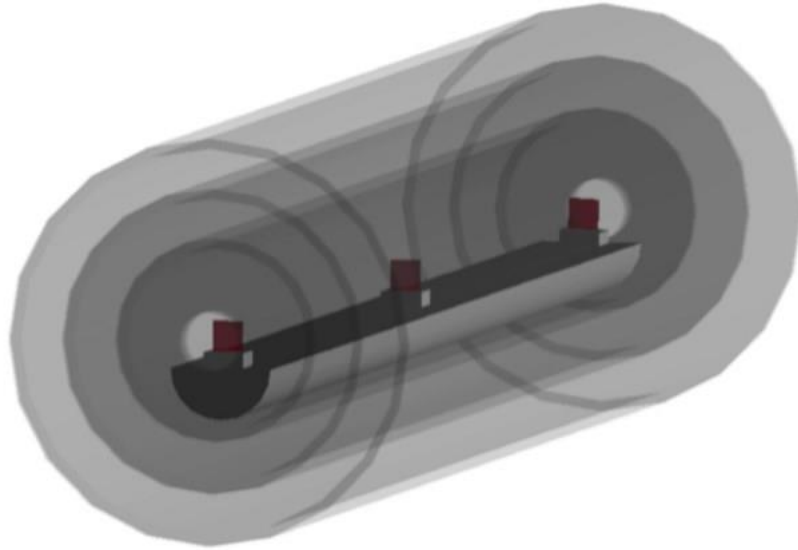
While Conrad was designing his experiment to detect a time distribution of pions to indirectly determine antiproton annihilation, I was tasked with creating slightly different chambers for two separate experiments: working with a group in Heidelberg, we want to use unique nano gratings to study the quantum nature of antiprotons; we also would like to determine the fragmentation properties of various foils when struck with an antiproton beam.

The fragmentation experiment required the smallest number of modifications to Conrad's chamber. Using a flange and gate valve, we will be able to dismantle the back of our detector, which will contain an emulsion that is specifically chosen to see only nuclear fragmentations rather than pions, as well as an interchangeable foil. With about 10 different elemental foils to test, it will be necessary for access to this foil to be easy and quick.

The simulation of the fragmentation events is not quite as simple as the setup. Geant4 has a minimum step size for tracking particles of about 1 mm. However, the foils that will be used will only be a few tens of microns thick. Changing the step size, though easy, is not the best solution for this, as decreasing the step size by a factor of 10 increases the simulation time by a factor of about 100. Instead, a new physics engine will need to be created to handle small step sizes only for nuclear fragments and antiprotons.

The second task is not nearly as intuitive as the first, as the interferometry experiment is not the traditional one used for demonstrating the self-interference of photons. Instead, the apparatus consists of three gratings, two of which will be aligned with one another, and the third of which will be slightly angled. Doing this will create a Moire pattern on our emulsion. To observe the de Broglie wavelength of antiprotons, we will be sending a beam of them through one-of-a-kind  $3 \times 3 \text{ mm}^2$  silicon nitride gratings that are only 160 nm thick. However, our beam starts with a 1 cm diameter, which is given a large divergence and range of momenta by the degraders. The divergence can be corrected slightly by replacing the aluminum degrader with a lower-Z lithium foil. To select the momenta we want, we will be mounting the detection chamber on a table in such a way that it can be rotated. We will then use a small, localized magnetic field to select antiprotons of 10-1000 eV (which is cold enough to be entirely stopped by the grating when not passing through a slit) then collimate them in a titanium chamber. In this way, we hope to have a flux of approximately 1000 antiprotons per burst, where each burst has  $10^7$  antiprotons, across the gratings.





The momentum selection creates even more problems for our detector: if the fringing fields of our magnetic field, which in the current construction is created by two parallel magnetized toroids, is much larger than 1 Gauss at the gratings, then the interference pattern will be too disturbed to glean any useful information from the emulsion. Our backup plan for this case is to replace the nucleon-detecting emulsion with a silicon pixel detector. In this way we can gather information about spatial and temporal motion, thus allowing us to sort our results by momentum and look only at events with the desired energy and removing the need for a chamber rotation or magnetic field.

The future of this project will hopefully be completely experimental. With the assembly of this detector beginning in July and the AD beamline running in August, next year should see a lot of data-taking and analysis. With new figures from actual physical phenomena, we will be able to communicate with Geant4 developers any changes that need to be made to existing physics engines. The prospect of creating metastable states of  $pLi^+$  in our type of experiment, something that has not yet been accomplished, is very exciting. The possibility of measuring the quantum properties of antimatter will bring us one step closer to the purpose of AEGIS itself: determining the matter/antimatter symmetries of the Weak Equivalence Principle, which states that all objects fall at the same rate under the influence of gravity.

Ivan Lavrentyev

20 August 2014

## **SDD Detector Analysis**

### **Abstract**

We are working with an SDD Detector that will be mounted to CAST to take data in the summer of 2014. In order to understand how the detector performs, we ran some tests in the lab and carried out an analysis. The detector was calibrated, its resolution was found, and its efficiency was studied. The results of the detector analysis are described in detail in this report.

### **Calibration and Resolution Analysis**

#### Introduction:

The SDD Detector is tested in the lab using an apparatus consisting of an X-Ray Generator and a Vacuum Tube Chamber.

The X-Ray generator consists of a cathode and anode target. When a voltage is applied to the filament, electrons are accelerated through the potential difference between the cathode and anode. The stream of electrons strikes the metal (anode) target and causes it to emit X-Rays. The emission of X-

Rays is caused by the sudden deceleration of the electrons as they pass through the target

(Bremsstrahlung) and by the collisions with the metal target that release inner shell electrons, causing them to be replaced by higher state electrons releasing X-Rays with an energy equal to the energy difference between states (Characteristic X-Ray Emission). The Characteristic X-Rays are unique to the atomic structure of the particular target used.

#### Calibration:

The SDD detector data is recorded in channels by a multi channel analyzer (MCA). The calibration of the detector involves finding a relationship between the channel output and energy. This is done by changing the anode targets of the X-Ray Generator. Each target has a unique Characteristic X-Ray spectrum, which is recorded by the detector as one or more peaks with Gaussian distributions along a continuous spectrum (Bremsstrahlung). The energy of each peak is known, and can be compared with the channel output. To finish the calibration, a fit is performed that results in the calibration formula.

#### Resolution:

The peaks of the Characteristic X-Rays are recorded as Gaussian distributions (ideally they would be recorded as vertical lines). The resolution of the detector can be found from the full width at half-maximum (FWHM) of the Gaussian distributions. The resolution is conventionally given by the FWHM divided by the peak energy. The FWHM of each peak (for each target) is calculated, and converted to resolution (shown below). Then a fit is performed that gives a relationship between the resolution and energy.

#### Data and Results of Analysis:

*Anode Targets Used:*

Carbon, Aluminum, Manganese, Copper, Silver, Gold, Titanium

**TABLE 1: TABLE OF CHARACTERISTIC X-RAY EMISSION ENERGIES (EV)**

Element	$K\alpha_1$	$K\alpha_2$	$K\beta_1$	$L\alpha_1$	$L\alpha_2$	$L\beta_1$	$L\beta_2$	$L\gamma_1$	$M\alpha_1$
Carbon	277								
Aluminum	1,486.70	1,486.27	1,557.45						
Titanium	4,510.84	4,504.86	4,931.81	452.2	452.2	458.4			
Manganese	5,898.75	5,887.65	6,490.45	637.4	637.4	648.8			
Copper	8,047.78	8,027.83	8,905.29	929.7	929.7	949.8			
Silver	22,162.92	21,990.3	24,942.4	2,984.31	2,978.21	3,150.94	3,347.81	3,519.59	
Gold	68,803.7	66,989.5	77,984	9,713.3	9,628.0	11,442.3	11,584.7	13,381.7	2,122.9

The Characteristic X-Ray spectra of each target were fit with a Gaussian distribution to find the maximum peak values (in channels). Plots of the Gaussian fits for Silver and Manganese are shown below.



FIGURE 1: X-RAY SPECTRUM OF SILVER (DETECTOR DATA)

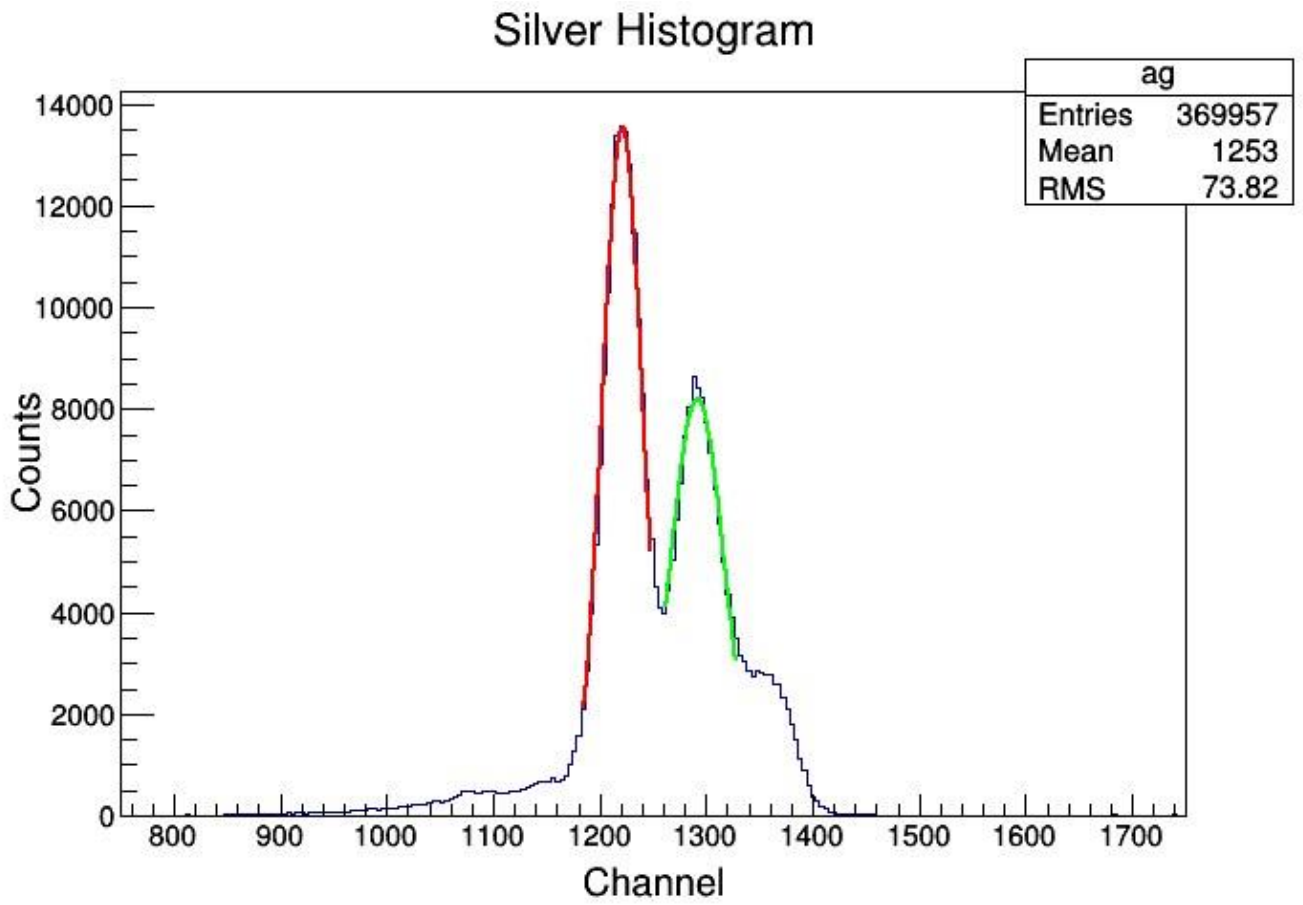
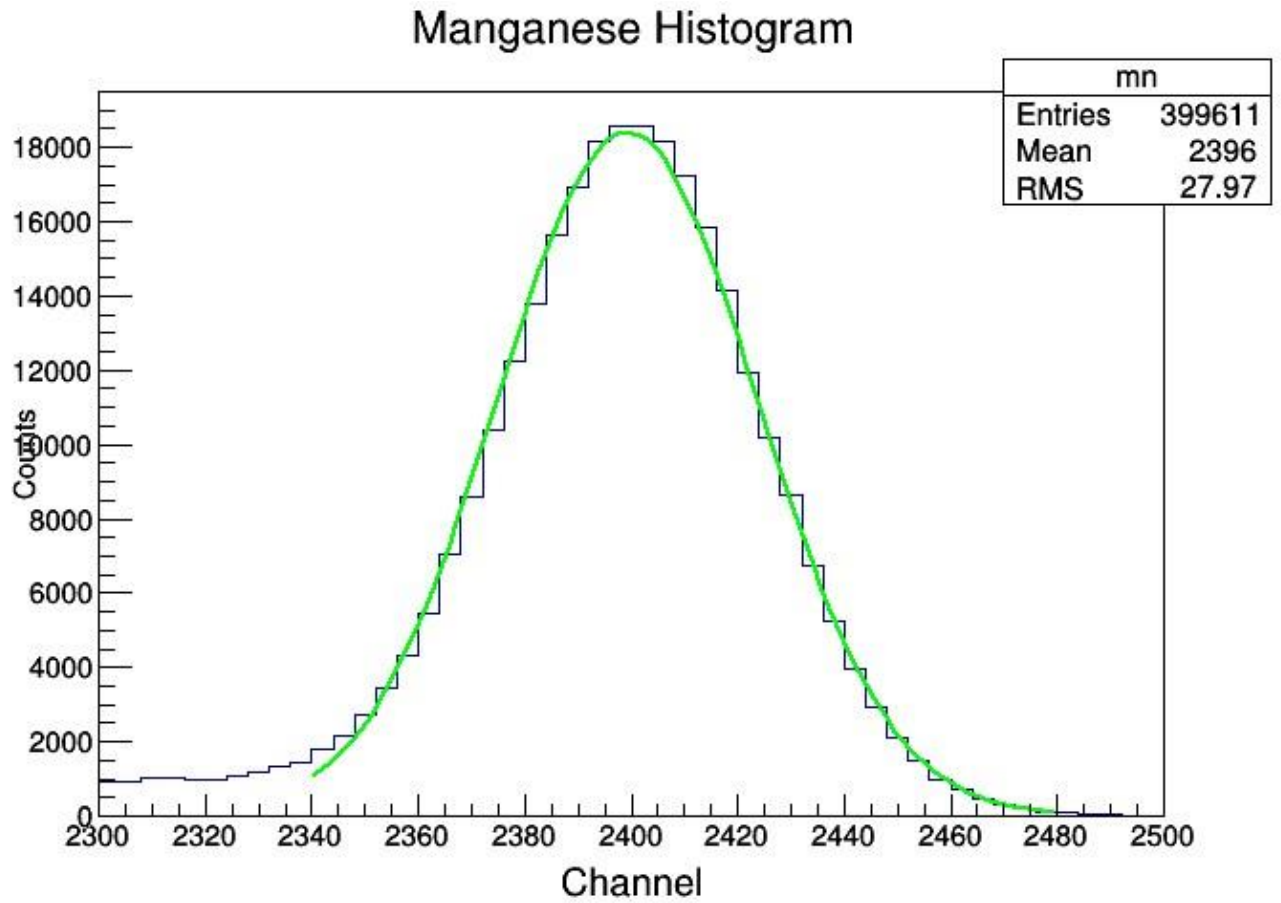


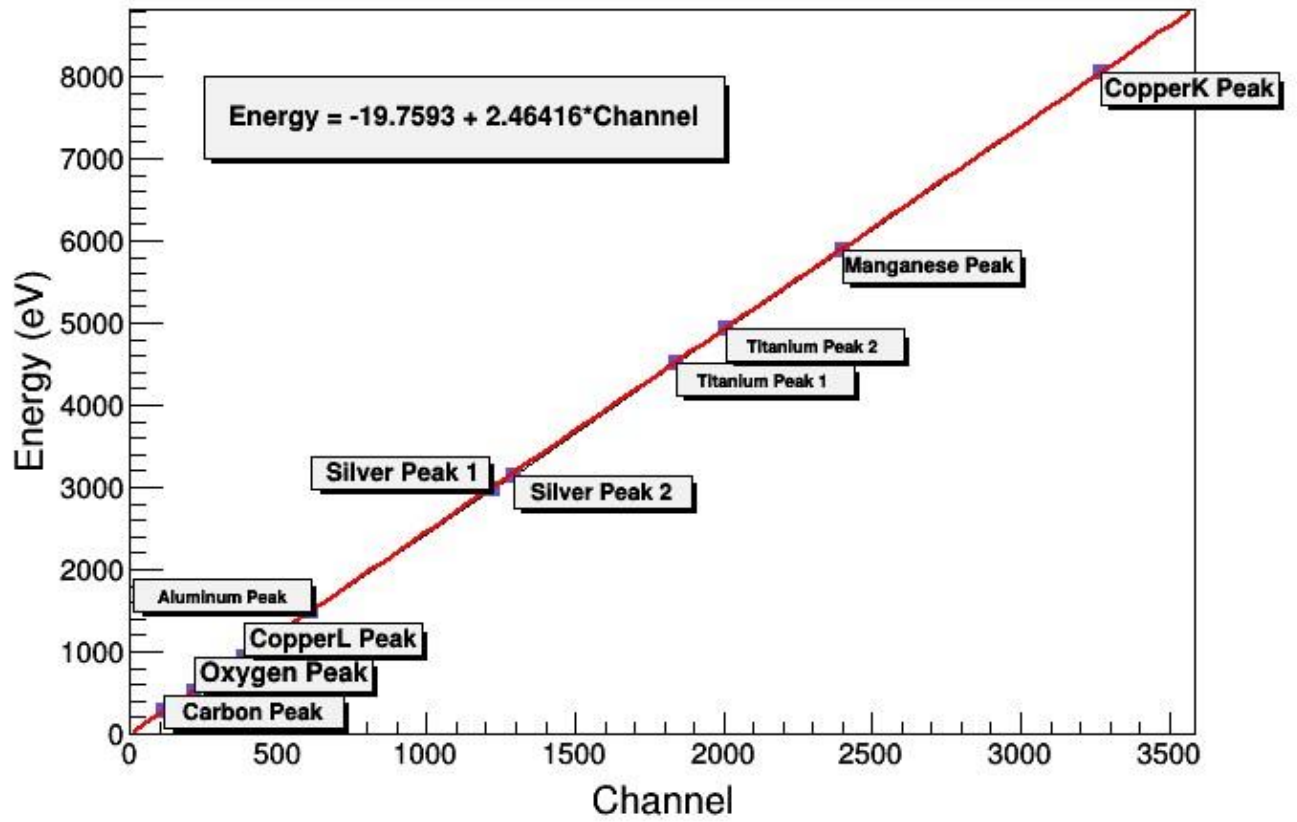
FIGURE 2: X-RAY SPECTRUM OF MANGANESE (DETECTOR DATA)



The peak channel values of each target element were plotted against their corresponding energy values (given in Table 1). This plot (shown in Figure 3) was fit linearly, resulting in the calibration formula relating channel number and energy (given by Equation 1).

Figure 3: Channel versus Energy Fit

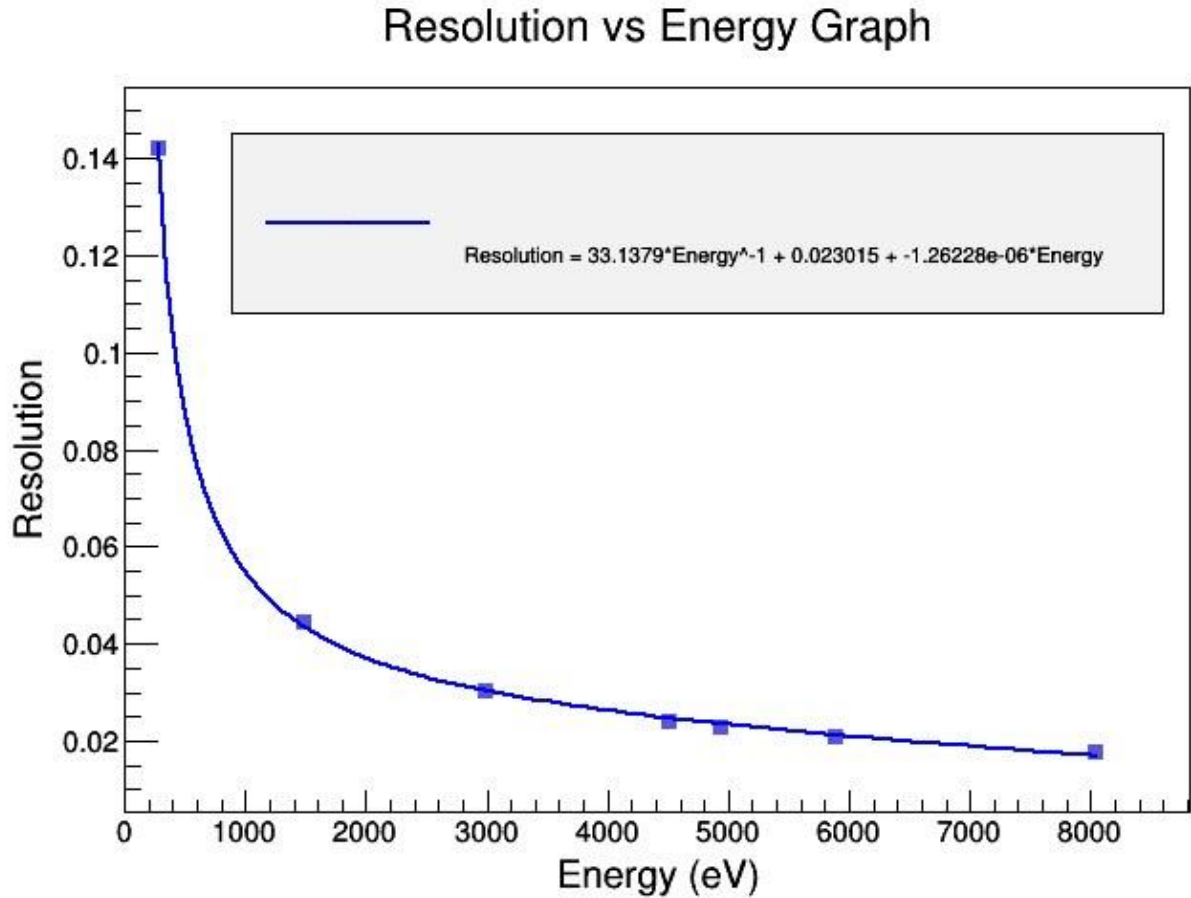
### Channel vs Energy Graph



From the above plot, the fit equation for the detector calibration was calculated to be:

**(Equation 1) Energy = -19.7593+ 2.46416\*Channel**

FIGURE 4: PLOT OF RESOLUTION VERSUS ENERGY



Additionally, the fit equation for Resolution versus Energy is given by:

$$\text{(Equation 2) Resolution} = 33.1379 \cdot \text{Energy}^{-1} + 0.023015 \cdot \text{Energy} + -1.26228 \cdot 10^{-6} \cdot \text{Energy}$$

This completes the analysis of the detector calibration and resolution.

## Detector Efficiency

### Introduction

We notice that the transmission percentage of the SDD detector decreases over time. The purpose of the analysis is to model the efficiency of the detector.

The SDD detector operates by recording the ionization energy of incoming photons. The detector is cooled to around  $-30^{\circ}\text{C}$  (via Peltier cooling) when recording data in order to reduce thermal noise. The decrease in temperature causes a trace gas in the vacuum to

condense and form a thin film over the detector. The thickness the layer of film increases with time (more molecules of gas condense on the detector). This causes a decrease in count number (transmission percentage) as the detector is left running which is most noticeable at low energies (400-600 eV).

When X-Rays pass through a filter of some material, there is some level of absorption and scattering which decreases the count of X-Rays recorded by the detector. The transmission of X-Rays through a filter can be modeled by the Beer-Lambert Law.

$$\text{(Equation 3) } T = I/I_0 \exp [ - \mu \rho \tau ]$$

where  $\mu$  = mass attenuation coefficient ( $1/(\text{microns} \cdot \rho)$ ),  $\rho$  = compound density, and  $\tau$  = thickness of compound (microns). The mass attenuation coefficient of a compound varies with photon energy (and has been calculated experimentally). The mass attenuation coefficient for molecules can be extrapolated from the individual elements using the following equation.

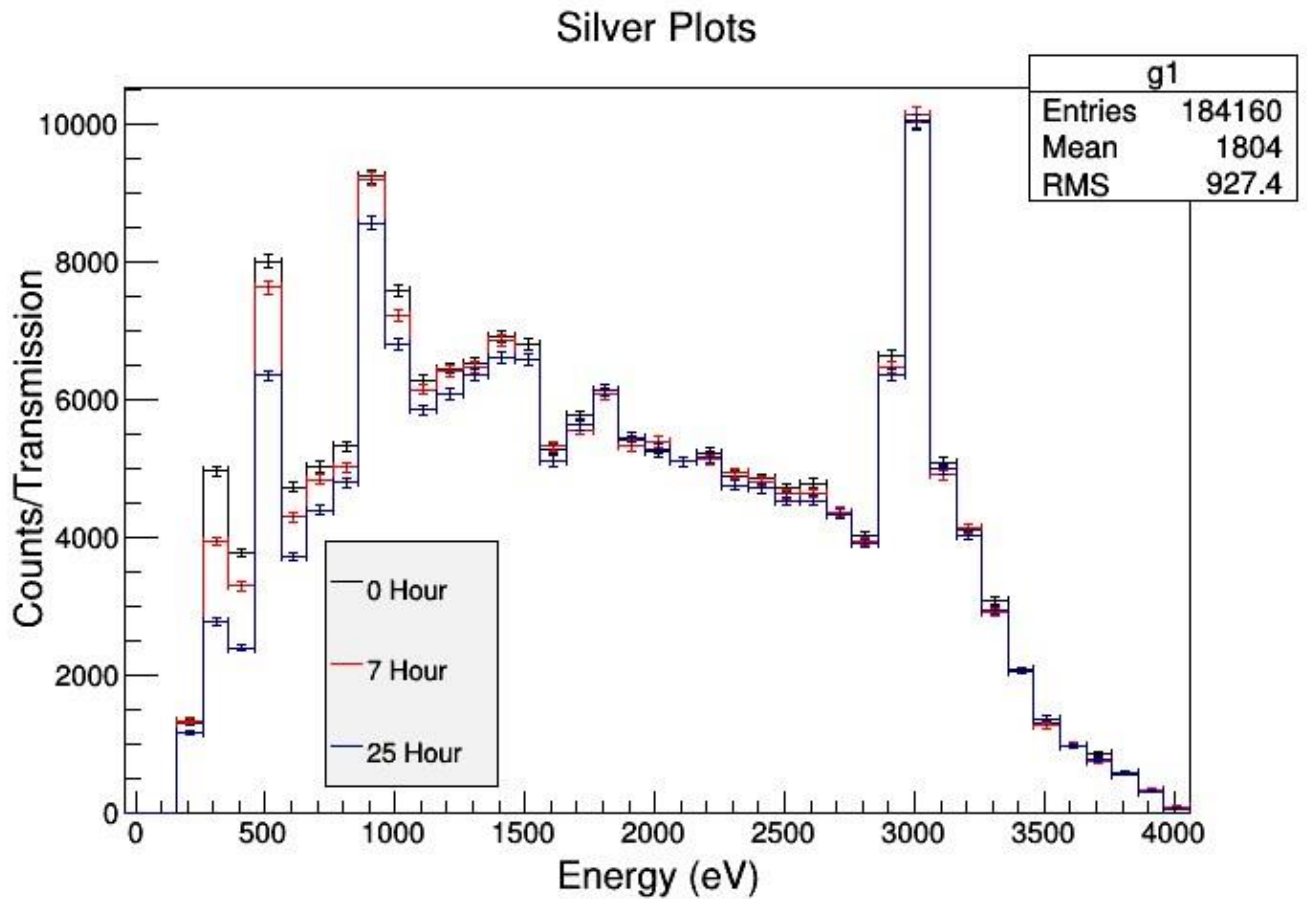
$$\text{(Equation 4) } \mu = \sum_i w_i (\mu)_i$$

where  $w$  is the fractional weight of an element  $i$ .

#### Procedure, Data and Results of Analysis

The detector was left running over a period of 25 hours. It recorded the Bremsstrahlung and Characteristic X-Rays of a silver target. A spectrum was obtained for each hour of data taking by merging 3 data files within a given hour.

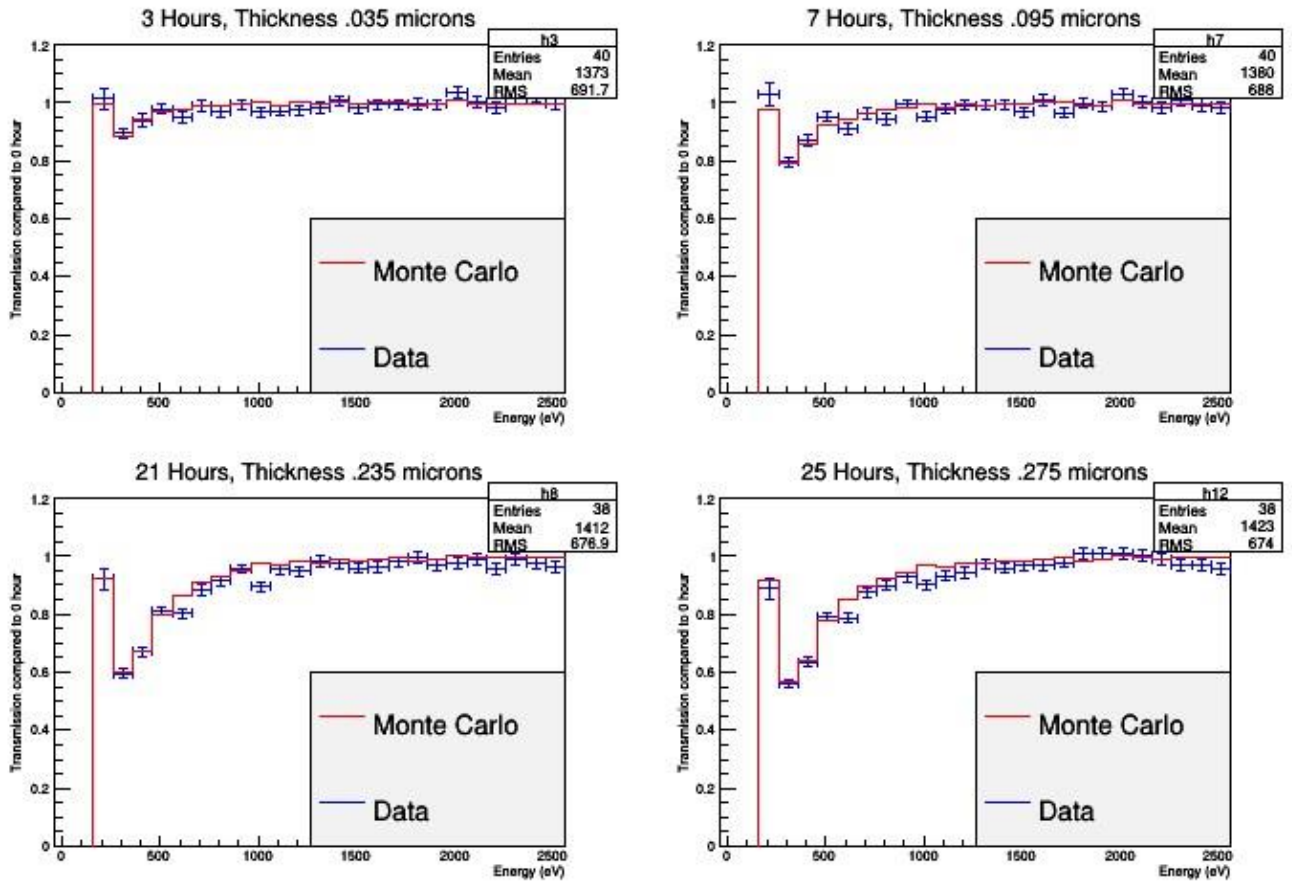
FIGURE 5: HISTOGRAM OF DETECTOR DATA (3 SAMPLE HOURS)



The spectra plots (for each hour) were then divided by the spectrum plot of the detector immediately after it was cooled down, resulting in a plot comparing transmission percentage and energy. The transmission spectrum (versus energy) of the detector was compared with the filter transmission spectra of various elements and compounds. The transmission spectrum closely resembled that of a hydrocarbon. Cyclopropane (C<sub>3</sub>H<sub>6</sub>) was selected to model the efficiency because it has a boiling point at -33° C, similar to the -30° temperature of the detector.

A Monte Carlo simulation was created using the filter transmission data of Cyclopropane (folded with the resolution of the detector) to model the detector efficiency. The Monte Carlo plots were compared with the detector data plots. A Chi-Squared fit was performed that gave the optimal Monte Carlo model for each hour of data.

FIGURE 6: MONTE CARLO COMPARED WITH DATA PLOT



The thickness of the filter was used as the independent variable thickness for each hour of data taking.

The Chi-Squared fit returned the optimal filter thickness per hour, which was used to plot the Monte Carlo plot above. Using the optimal thickness values for each hour, a formula relating thickness and time was calculated.

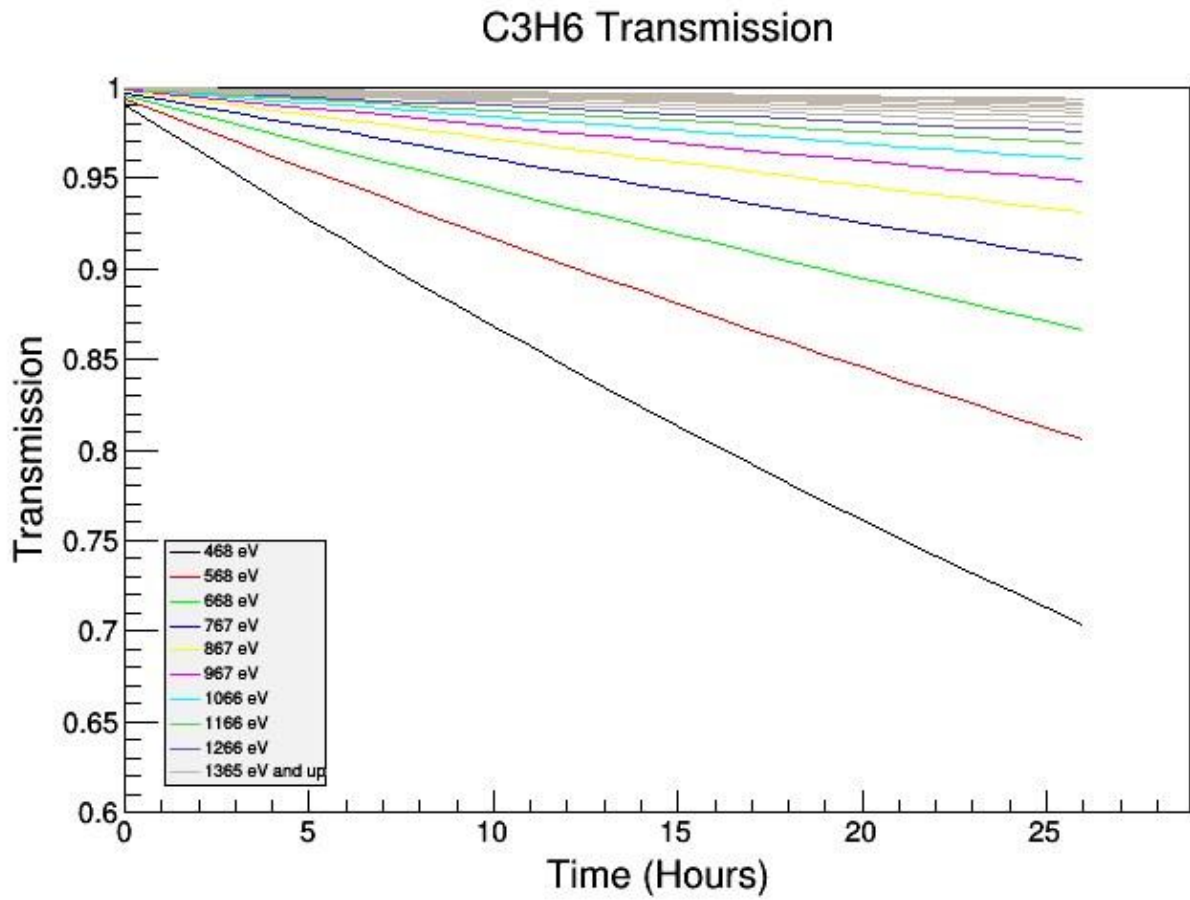
$$\text{(Equation 5) Thickness (microns)} = 0.106 * (\text{Hour}) + .0078$$

The transmission (given by Beer-Lambert Law, Equation 3) depends on both filter thickness and mass attenuation coefficient. The mass attenuation coefficient varies with energy and this relationship is known experimentally. The thickness and attenuation coefficient (for a respective energy) were plugged into the Beer-Lambert law (Equation 3) to find the Transmission percentage for a given hour for a range of energies. Using following formula, we were able to model the detector efficiency for a given energy and time.

**(Equation 6)  $\text{Transmission} = \exp(-\mu(\text{energy}) * \tau(\text{time}) * \rho)$**

where  $\tau$  is given by (Equation 5). Where Transmission is given in percent, the thickness  $\tau$  in units of microns, the attenuation coefficient  $\mu$  in units of  $1/(\text{microns} * \rho)$ .

**FIGURE 7: DETECTOR TRANSMISSION MODEL**



The above plot was created by obtaining the mass attenuation coefficient  $\mu$  for several energies (known data), then plugging  $\mu$  into Equation 6 along with the thickness  $\tau$  for each hour of data. The above curves were then fit and parametrized to model the transmission decrease and to better understand how our detector functions over time.



**TABLE 2: TABLE OF FIT EQUATIONS FOR VARIOUS ENERGIES**

<b>Energy (eV)</b>	<b>Fit Equation</b>
468.68	$T = \text{Exp}(-0.00967997 + -0.0131454*(\text{Time}))$
568.38	$T = \text{Exp}(-0.00595435 + -0.00808604*(\text{Time}))$
668.08	$T = \text{Exp}(-0.00395695 + -0.00537356*(\text{Time}))$
767.78	$T = \text{Exp}(-0.00275548 + -0.00374196*(\text{Time}))$
867.48	$T = \text{Exp}(-0.00197367 + -0.00268025*(\text{Time}))$
967.18	$T = \text{Exp}(-0.00146158 + -0.00198484*(\text{Time}))$
1066.88	$T = \text{Exp}(-0.00111228 + -0.00151048*(\text{Time}))$
1166.58	$T = \text{Exp}(-0.000864285 + -0.0011737*(\text{Time}))$
1266.28	$T = \text{Exp}(-0.000685191 + -0.000930493*(\text{Time}))$
1365.98	$T = \text{Exp}(-0.000550886 + -0.000748106*(\text{Time}))$
1465.68	$T = \text{Exp}(-0.000449715 + -0.000610716*(\text{Time}))$
1565.38	$T = \text{Exp}(-0.000371619 + -0.000504661*(\text{Time}))$
1665.08	$T = \text{Exp}(-0.000310611 + -0.000421811*(\text{Time}))$
1764.78	$T = \text{Exp}(-0.000262227 + -0.000356106*(\text{Time}))$
1864.48	$T = \text{Exp}(-0.000223188 + -0.000303091*(\text{Time}))$
1964.18	$T = \text{Exp}(-0.000191561 + -0.000260142*(\text{Time}))$
2063.88	$T = \text{Exp}(-0.000165678 + -0.000224992*(\text{Time}))$

Above are the numerical formulas for transmission with respect to time. These were extrapolated from the theoretical formula.

## **Conclusion**

During the analysis, several tasks were performed. The detector was calibrated and its resolution was obtained. The efficiency of the detector was analyzed and the transmission percentage was modeled (due to the deposition of an unknown compound on the detector surface). The results of this analysis can be used to interpret and understand the 2013 data. Going forward for 2014, the detector vessel (vacuum chamber) may need to be redesigned (components such as cables removed from the vacuum of the vessel to an external Faraday Cage) in order to decrease the presence of extraneous compounds in the vacuum chamber. We will then mount the detector onto the CAST apparatus and perform data collection for 2014, hoping to eliminate the effect of the hydrocarbon deposition.

# Gain Optimization for Future Large Scale Double Phase Liquid

## Argon TPCs

Ryan Linehan

Advised by Sebastien Murphy, Ph.D, and Shuoxing Wu, Ph.D

July 1, 2014

### 1 INTRODUCTION

#### 1.1 THE LIQUID ARGON TIME PROJECTION CHAMBER

The search for knowledge about neutrinos depends critically on the ability to detect neutrino interactions. Due to the extraordinarily low cross sections of interactions between neutrinos and any kind of matter, neutrino detectors must necessarily be massive. One current type of neutrino detector is the liquid argon time projection chamber, or LArTPC.

Two kinds of LArTPCs exist today: single phase and double phase. The single phase detector is completely filled with liquid argon. On one side of the detector, there is a cathode held at some potential, and on the other side, there is a set of anode wire planes held at a much more positive potential. An electric field is thus created across the chamber. See Figure 1.1 [1] for reference.

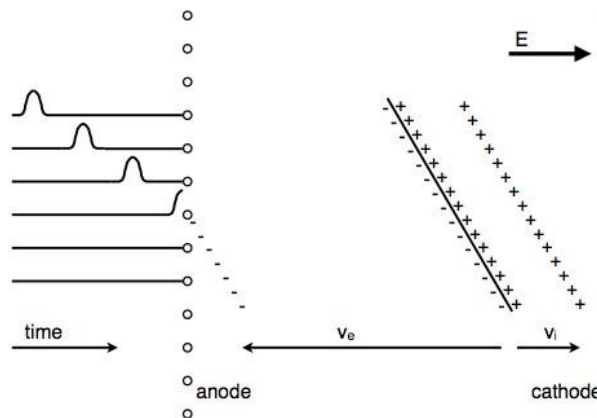


Figure 1.1: Basic function of a single phase LArTPC's operation.

When an ionizing particle passes through the chamber, it creates electron-ion pairs. Due to the electric field, the electrons drift toward the wire planes, and either induce signals or are collected by

these planes. In this way, these planes, whose wires are oriented in different directions, can establish an "x" and "y" coordinate for the particle's trajectory. The trajectory's position along the drift length is determined with the help of the argon's scintillation. A PMT is kept in the chamber to trigger on the scintillation caused by a particle, and the time in between the trigger and the signal at the anode determines the "z" coordinate. In this way, a LArTPC can ideally reconstruct the entire 3D trajectory of a given particle.

The double phase detector operates on roughly the same principles, but is filled only partially with liquid argon. The rest of the chamber is filled with argon gas, and a grid is placed at the liquid-gas interface to extract the drifting electrons into the gas. The electrons then pass through holes of a large electron multiplier (LEM), in which an amplification electric field considerably higher than the drift field is present. Because of the increased electron mean free path in gas, these electrons experience Townsend avalanches in the LEM holes. The exiting electrons then reach an anode, where the charge is split and collected on two views. See Figure 1.2 [1]. This is in contrast to single phase detectors, where signal is obtained on both induction and collection planes.

The motivation for these double phase LEM-LArTPCs comes from the LEMs' ability to amplify the drift charge. This grants a higher signal-to-noise ratio than that offered by the single phase detector, and can therefore provide a more accurate reconstruction of particle trajectories and identities in neutrino detectors.

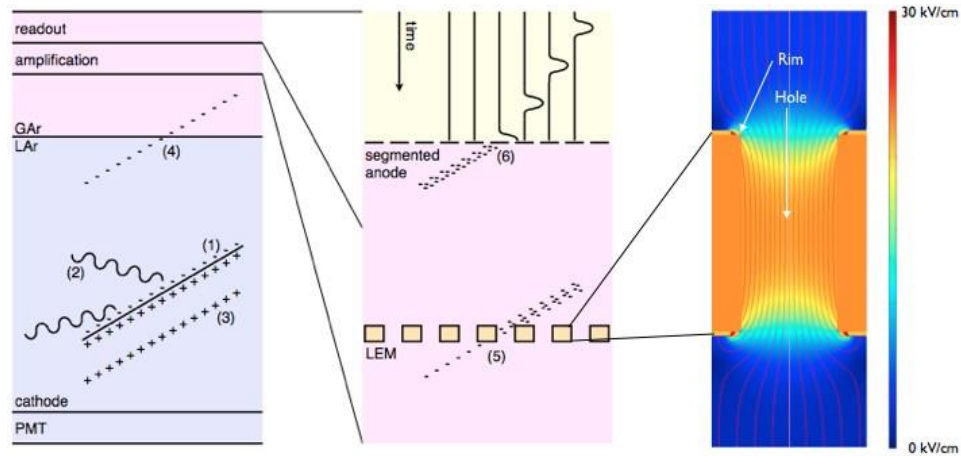


Figure 1.2: Basic function of a double phase LArTPC's operation. The far right image displays a LEM hole with electric field lines passing through.

## 1.2 PROJECT GOALS

Because the signal amplification occurs entirely within the LEM holes, the signal-to-noise ratio is primarily dependent on the geometric characteristics of these holes and the amplification electric field inside. LEMs with different geometries can bring about very different signal-to-noise ratios, so it is important to test several geometries of LEMs to determine which provide optimal ratio.

Here, we define the gain of the detector as  $\frac{dQ/dx_{collected}}{dQ/dx_{released}}$ , the ratio of charge collected on the anode per unit length of the track, divided by the ratio of charge released by the ionizing particle per unit length of the track. In our case, the ionizing particles used for gain measurement were cosmic muons, which have a known  $dQ/dx$  of about 10 fC/cm. Our objective was to find the LEM geometry and manufacturer that yields the highest gain.

For our gain calculations to be as accurate as possible, we must find the most accurate  $dQ/dx$  collected by the anode. We calculate this with the help of Qscan, a software that allows us to

reconstruct 3D particle tracks and determine the track's  $dQ/dx$  as collected on the anode. This software provides multiple track reconstruction methods, and so for the most accurate gain calculations, we needed to find the algorithm with the best efficiency in recognizing and reconstructing tracks.

Once we determine which algorithm is best suited for gain calculation, the next step is to understand how the gain for a given LEM varies with a changing amplification field. Finding these "gain curves" facilitates a comparison of different LEMs, allowing us to select the optimal set of hole patterns and geometries to use in future double phase LArTPC projects. The optimal hole patterns and geometries will be applied to large LEM boards that will be employed by such large TPCs as the 1x1x3 m<sup>3</sup> and the 6x6x6 m<sup>3</sup> detectors, and even larger ones in the far future.

## 2 APPARATUS AND METHOD

This section addresses the setup of our detector and outlines in chronological order the procedure followed to prepare and test the LEMs and analyze the resulting data.

### 2.1 THE 3L DETECTOR

In our gain testing, we used a double phase detector called the 3L (Figure 2.1, left image). It is comprised of a PMT at the bottom, above which is a cathode and a series of metal field shapers, spaced 5mm apart. These create the drift field. Above the field shapers are the extraction grid, LEM (Figure 2.1, right image), and anode, respectively.

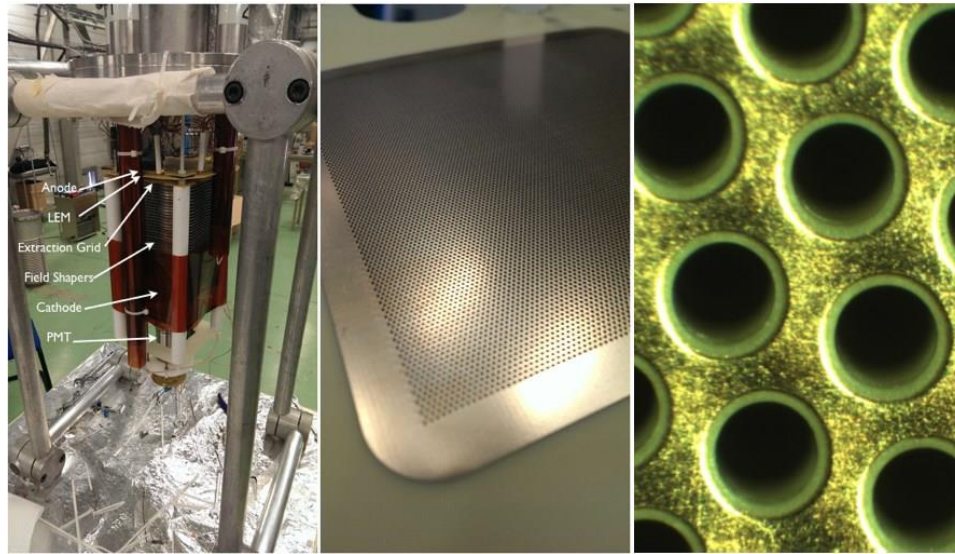


Figure 2.1: Left: 3L Setup, Center: A 10x10 cm<sup>2</sup> LEM board. Right: A Close-up of LEM holes.

The anode consists of two views, each intended to record a two-dimensional position ( $x,z$  or  $y,z$ ) of the drift charge's position. When charge drifts upward and is collected on the anode views, it is transported to a set of two preamplifier boards, one for each view, where the charge is converted to a voltage based on the charge sensitivity of each board. The charge sensitivity is defined as the voltage produced per unit charge collected. Finally, this voltage is digitized, and the result is saved to the data acquisition system.

## 2.2 PREAMPLIFIER CHARGE SENSITIVITY MEASUREMENTS

For a correct computation of a LEM's gain, we needed to determine the charge sensitivities of the preamplifier boards. We had previously known that several of our boards had charge sensitivities depending on the nearly impossible-to-determine detector capacitance, and that two others had sensitivities independent of this detector capacitance. In order to maintain control over more experimental variables, we decided to use the latter two boards for our calculations.

Prior to testing, these two boards often showed a saturation of the digitized voltage signal. Permitting this would provide a low and incomplete estimate of the gain, so we reduced the charge sensitivity on these boards with the intent of preventing saturation.

To determine the reduced charge sensitivities for these two boards and the charge sensitivities of the other boards, we used a pulse generator and a shielding box containing 32 simple circuits in parallel. Each circuit corresponds to a single channel on a given board, and injects charge into that channel. The circuit design is in Figure 2.2.

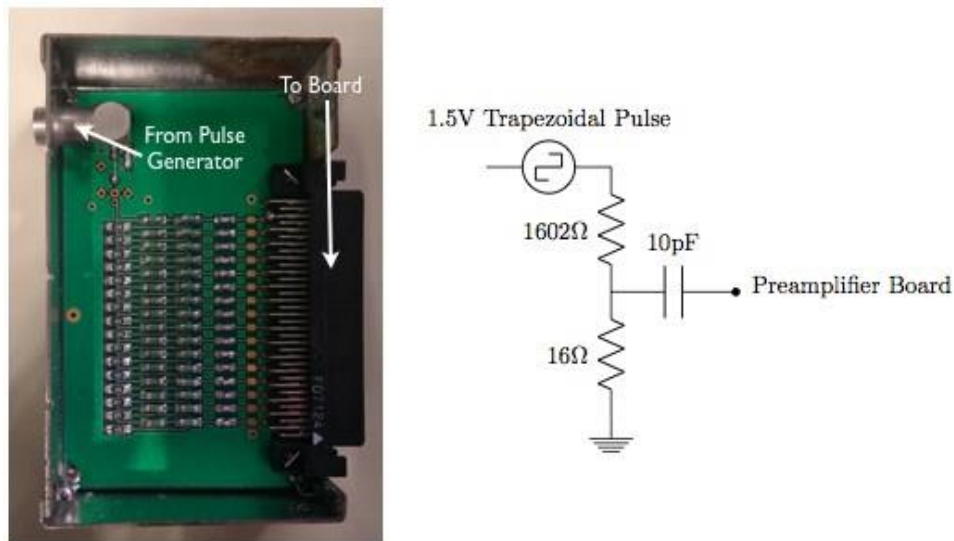


Figure 2.2: Left: The box used to inject charge into the preamplifiers for charge sensitivity testing. Right: A schematic of the circuit that injected charge into a single channel.

We passed a trapezoidal pulse with a height of 1.5V through each of the circuits shown on the right in figure 2.2. (This circuit schematic assumes a detector capacitance of zero, for convenient comparison with previous studies of the sensitivities of the boards that were dependent on this variable [2].) With our voltage divider passing a rise of about 15mV to a 10pF capacitor, we injected 150 fC of charge into each channel for a given board. This produced a waveform in Qscan, which provides the integral of the waveform for a given channel in terms of ADC counts. Since the boards maintain a known relationship between ADC counts and the corresponding voltage, and since we knew the charge injected into each channel, we could find the charge sensitivity for each board. We performed this pulsing process for each of our boards. The result is plotted in Figure 2.3. The group of several histograms around 10 mV/fC display the charge sensitivities for the channels on the detector-capacitance-dependent preamplifier boards. The two histograms around 7 mV/fC are the charge sensitivities of the other two boards' channels. We used the charge sensitivities of these boards' channels for further calculations.

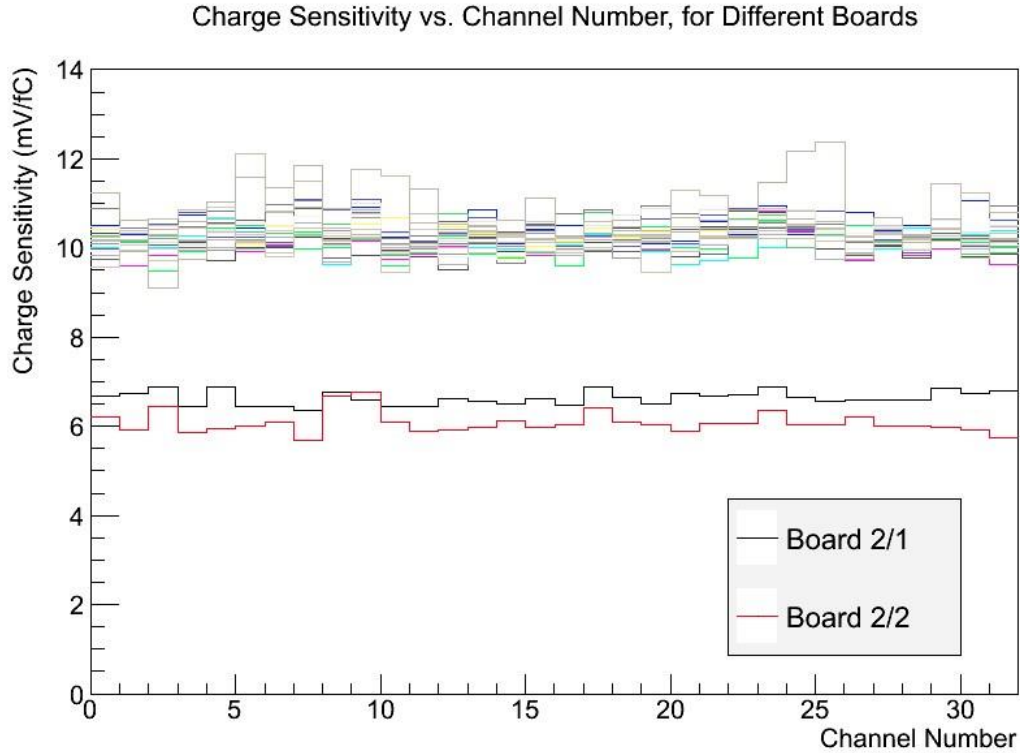


Figure 2.3: Channel charge sensitivities for the different preamplifier boards. The red and black histograms correspond to the detector-capacitance-independent boards, and the unspecified ones correspond to detector-capacitance-dependent boards.

### 2.3 TESTING PROCESS

Our primary objective was to determine which LEM geometry and manufacturer provided the 3L detector with the highest gain. For a given LEM, this implied a need to determine a largest stable gain. Since varying the amplification field changes the gain for a given LEM, this largest "stable" gain is that just before which the field is strong enough to cause discharges in the LEM holes.

To determine this maximum gain for a single LEM, we selected a starting amplification field, usually around 30 kV/cm. For this field value, we recorded the drift charges of a few thousand cosmic muons. The field was then increased at intervals of roughly 1 kV/cm, with similar measurements made at each interval. We incremented the amplification field until we could hear discharges occurring in the LEM holes. The field at which the discharges occurred was just above the field granting the highest stable gain for a given LEM.

We performed this process for five LEMs which varied in hole pattern, hole diameter, rim width (see Figure 1.2), and hole thickness. We will discuss the specific patterns and dimensions in more detail in section 3.

### 2.4 GAIN CALCULATION METHOD

With the drift charges of several thousand cosmic muons digitized and recorded for a given amplification field, we may calculate the gain in the following manner.

Qscan splits the total collected charge between two anode views. The total  $dQ/dx$  seen by the anode is therefore defined as:



$$\frac{\langle dQ_0/dx \rangle + \langle dQ_1/dx \rangle}{\langle dQ/dx \rangle_{MIP}}$$

where 0 and 1 refer to the x and y views, and the average is over all of the "hits" comprising tracks found by Qscan.

Before computing this, however, we must take into account the fact that electronegative impurities in the LAr can absorb drift electrons, causing larger losses of signal from the bottom than from the top. An exponential decay can be observed on the left in Figure 2.4, where  $dQ/dx$  is plotted against drift time. Without taking this signal loss into account, we would underestimate the gain produced by the LEM. We therefore fit the plot on the left for a drift electron lifetime, and then correct the charge per path length received on a given anode view with this lifetime as such:

$$(dQ/dx)_{corrected} = \frac{(dQ/dx)_{uncorrected}}{e^{-(hit\ drift\ time)/\tau}}$$

where  $\tau$  is the electron lifetime.

With the corrected charge, we may produce histograms of the hits'  $dQ/dx$  for each view. An example is that given in the right image of Figure 2.4. To find the gain, we take the means of the two views' plots, add them, and divide by the  $dQ/dx$  of a MIP, 10 fC/cm.

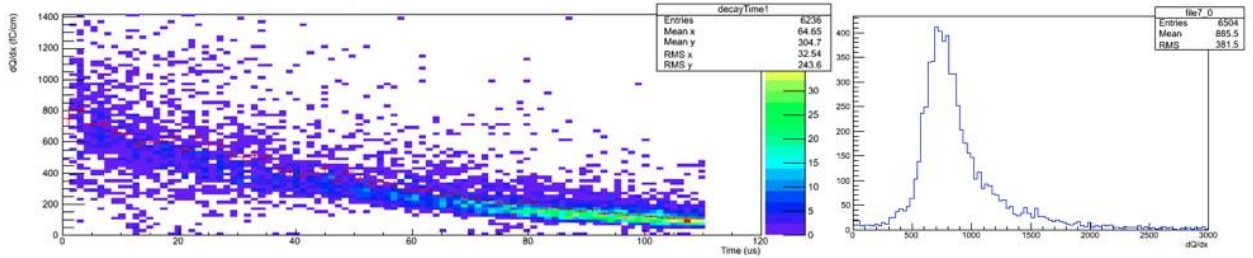


Figure 2.4: Left:  $dQ/dx$  vs. drift time of reconstructed hits. An exponential decay characterizing the absorption of drift electrons is apparent. Right: a distribution of corrected  $dQ/dx$  corresponding to the events used to generate the left image.

### 3 FINDINGS

#### 3.1 TRACK FINDING ALGORITHMS

Qscan offers two algorithms for use in identifying tracks: the hough transform and the tree method. Both aim to discern 2D tracks in the x-z (view 0) and y-z (view 1) planes. In short, the hough transform takes a hit in the image space into a sinusoidal curve in a transform space, and then identifies a line in the image space as a point where many sinusoidal curves intersect in the transform space. The tree method constructs links between adjacent hits, builds trees from these links, and creates "segments" from the longest trees with lowest total curvature. Trees are then made from these segments, and tracks are similarly found from the most ideal segment trees.

Our gain calculations demanded efficient reconstruction algorithms for the most accurate results. We thus sought the algorithm most suitable for these calculations. We found (Figure 3.1, top) that the tree method was able to recognize more good tracks for analysis than the hough transform for a given amplification field.

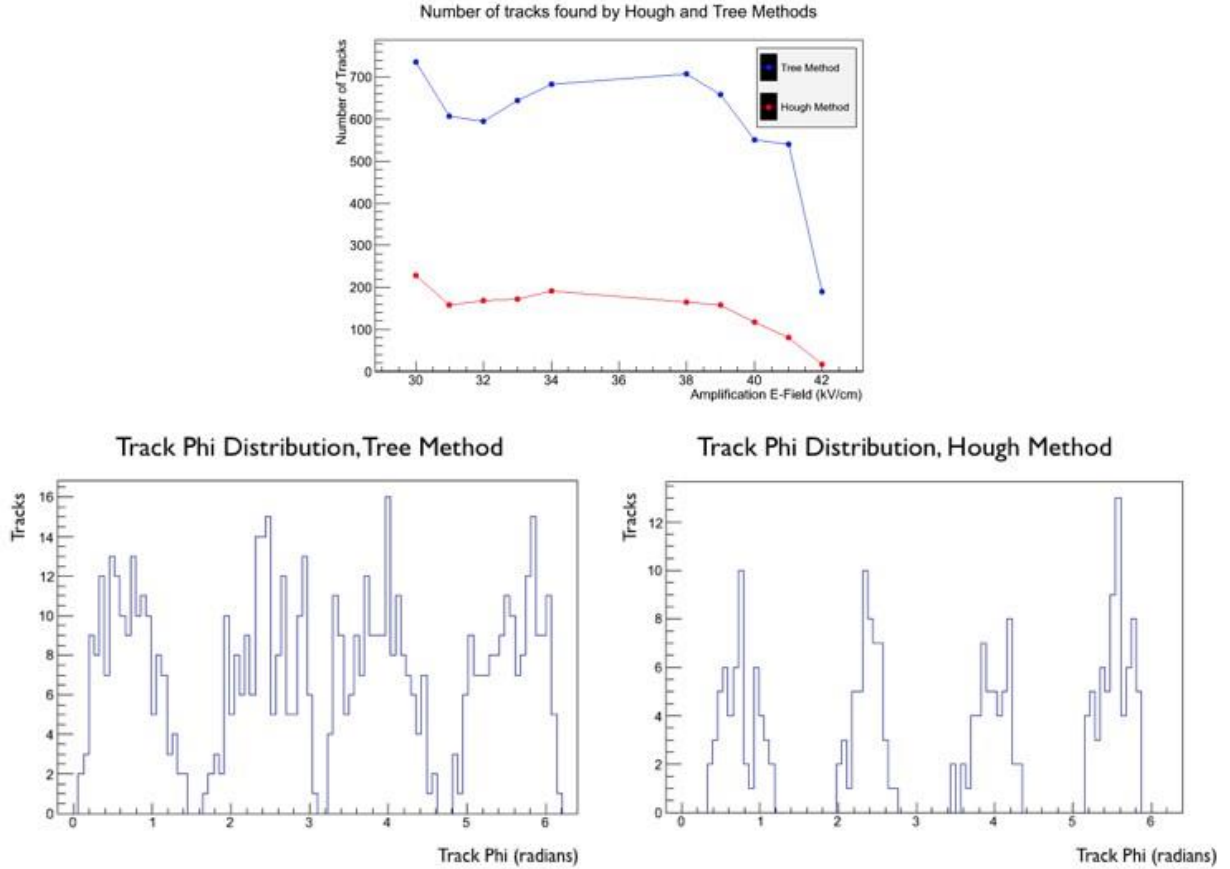


Figure 3.1: Top: numbers of good tracks found for the two track reconstruction algorithms. Bottom: Angular distributions of the tracks found by the two methods, showing the comparative weakness of the hough method near angles of  $\phi = \frac{n\pi}{2}$ .

This discrepancy can be partially attributed to the weakness of the hough transform to identify tracks that run nearly directly along either the x or y axis. In this case, there are many hits registered on one view, but only a few on the other. This lack of hits on a given view prevents a 3D track from being constructed. In the bottom of Figure 3.1, a comparison between the angular distribution of "good" tracks for both the hough and tree methods supports this claim.

Given that the tree method is generally more robust in its track finding capabilities, we decided to use it for gain calculations for the different LEMs.

### 3.2 FINAL GAIN CURVES

In this section, we present the results of the LEM testing. In the following plots, the LEMs are labeled LEM A, LEM B, LEM C, LEM D, and LEM E, according to the following table.

LEM	Hole Pattern	Manufacturer	Hole Diameter ( $\mu\text{m}$ )	Rim Width ( $\mu\text{m}$ )	Thickness (mm)
A	Square	CERN	500	80	0.8
B	Square	ELTOS	500	90	1
C	Hexagonal	CERN	500	40	1
D	Square	ELTOS	400	80	1



E	Square	ELTOS	500	40	1
---	--------	-------	-----	----	---

In this section, we compare the effects of hole pattern, hole diameter, and rim width on the gain of the LEMs. We present first for convenient reference all of the gain curves for our LEMs, in figure 3.2. The left image displays the gain as a function of the applied electric field, which is defined as the ratio of voltage difference applied between the top and bottom of the LEM and the thickness of the LEM hole. The right plot shows the gain as a function of the field at the center of each LEM, which was determined by computer simulations.

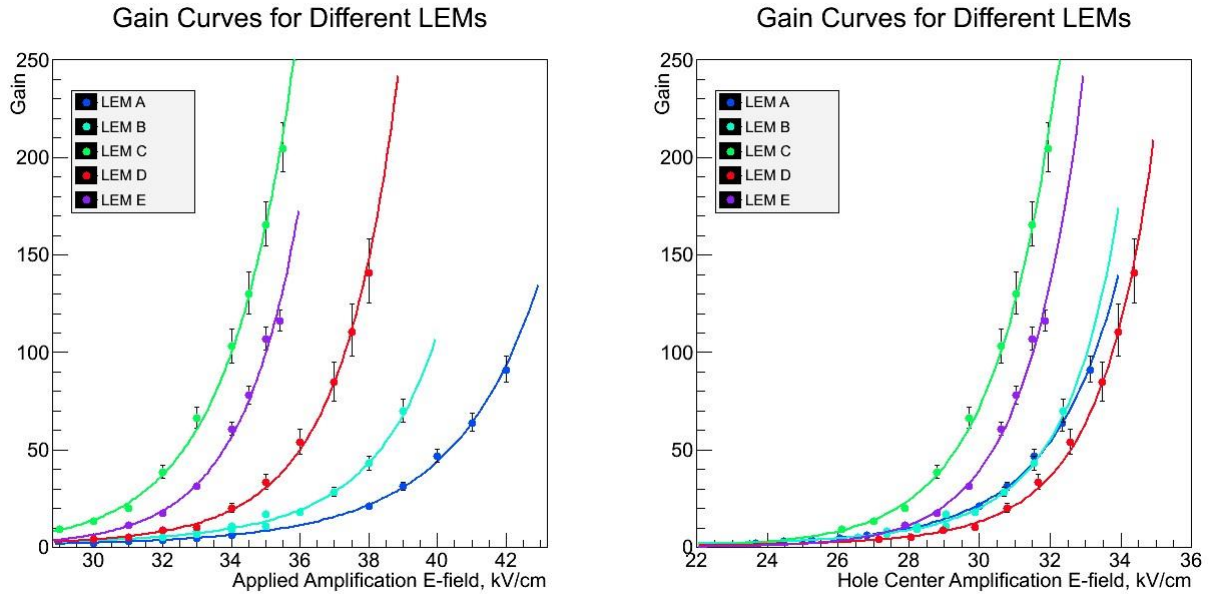


Figure 3.2: Left: Gain curves as a function of the electric field, assuming the field is  $\Delta V/\text{Thickness}$ . Right: Gain curves as a function of the true electric field at the center of the LEM hole.

### 3.2.1 HOLE PATTERN

Here, the hole pattern is the arrangement of the LEM holes on the LEM board. The two patterns used, visible in Figure 3.3, are a square pattern and a hexagonal or honeycomb pattern.

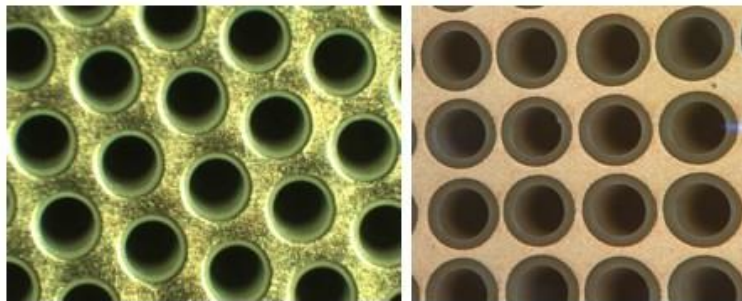


Figure 3.3: Left: Hexagonal or honeycomb pattern. Right: Square hole pattern.

To understand which gives an advantage, we examine LEM C and LEM E. From the plots, it is apparent that the hexagonal LEM pattern grants a larger gain than does the square pattern, for both

the applied and hole center E-fields. A possible explanation of this is in the behavior of the amplification field lines ending on the upper copper face of the LEM. These have a tendency to attract electrons emerging from the LEM away from the anode, reducing the electronic transparency of the LEM. It seems that a hexagonal geometry may reduce the influence of these edge fields relative to the square pattern, therefore increasing the LEM transparency and gain.

We also note that for the square pattern, we are generally able to reach a gain of about 100 for each LEM, regardless of the applied electric field. The exception would be LEM B, but we also note that this LEM might have been able to be pushed to slightly higher gains under further testing.

### 3.2.2 HOLE SIZE

The hole diameter's influence seems to be characterized by two conflicting phenomena. On the left in figure 3.2, one may see by comparing LEM D and LEM E that for a given amplification field, a smaller hole grants a larger gain. This may be because for a given applied voltage across the LEM, the density of field lines is greater inside a smaller hole, and therefore the E-field at the center of the hole, the field that governs the amplification strength, is larger. When one considers a constant hole center field, however, it appears that the larger hole size grants a greater gain. This may be due to the larger electron transparency given by a larger hole size.

### 3.2.3 RIM SIZE

From a comparison of LEM B and LEM E in Figure 3.2, it is evident that a smaller rim size grants a larger detector gain. However, from previous investigations into LEMs with a rim size of zero, we only found highest possible gains of around 30. This suggests that the optimal rim size is reached somewhere between 0  $\mu\text{m}$  and 90  $\mu\text{m}$ , and for the few tests that we have conducted, 40  $\mu\text{m}$  is the one that will give the highest gain.

## 4 CONCLUSIONS

From our first measurements, we conclude with some preliminary thoughts on the maximization of the detector gain. We first find that a hexagonal hole pattern is preferable to a square pattern. In spite of this, a square pattern yields gains of at least about 100, regardless of the LEM used or the E-field at which discharges were observed. We also find that higher gain for an applied E-field requires a smaller hole size, and that the rim size must be between 0  $\mu\text{m}$  and 90  $\mu\text{m}$ , with 40  $\mu\text{m}$  being the empirically determined peak.

To examine the LEMs' performances with respect to the signal-to-noise ratio, we provide figure 4.1. The sets of colored points correspond are the curves in Figure 3.2 with a logarithmic scale. The signal-to-noise ratio is found by dividing the lifetime-corrected amplitude of hits by the RMS of the signal. From the figure, it is evident that with the largest stable gain, we achieve a signal-to-noise ratio on the order of 1000. The advantage of these LEMs in double phase TPCs is apparent when this is compared with the signal-to-noise ratio of a single phase TPC, which is roughly 9.

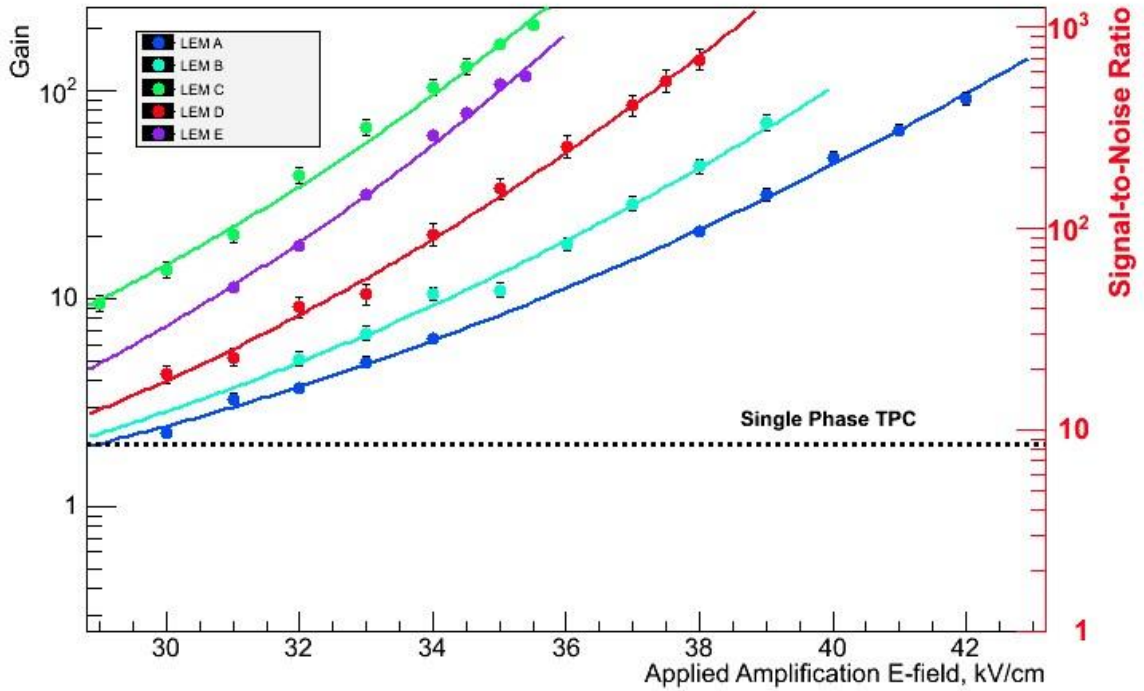


Figure 4.1: Gain vs. signal-to-noise ratio for the different LEMs and for single phase TPCs.

It is evident that these LEMs drastically improve the signal-to-noise ratio in LArTPCs, therefore facilitating event reconstruction and identification of particle interactions. A direct example of this high signal-to-noise ratio is shown in Figure 4.2, a cosmic muon event shown in Qscan's two views. The ratio between the hit amplitudes and signal RMS is on the order of 100, agreeing with the ratios given by Figure 4.1.

With our findings, future projects may be able to produce efficient larger LEM boards for use in large LArTPCs, where these signal-to-noise improvements will help bring progress to the search for understanding of neutrinos.

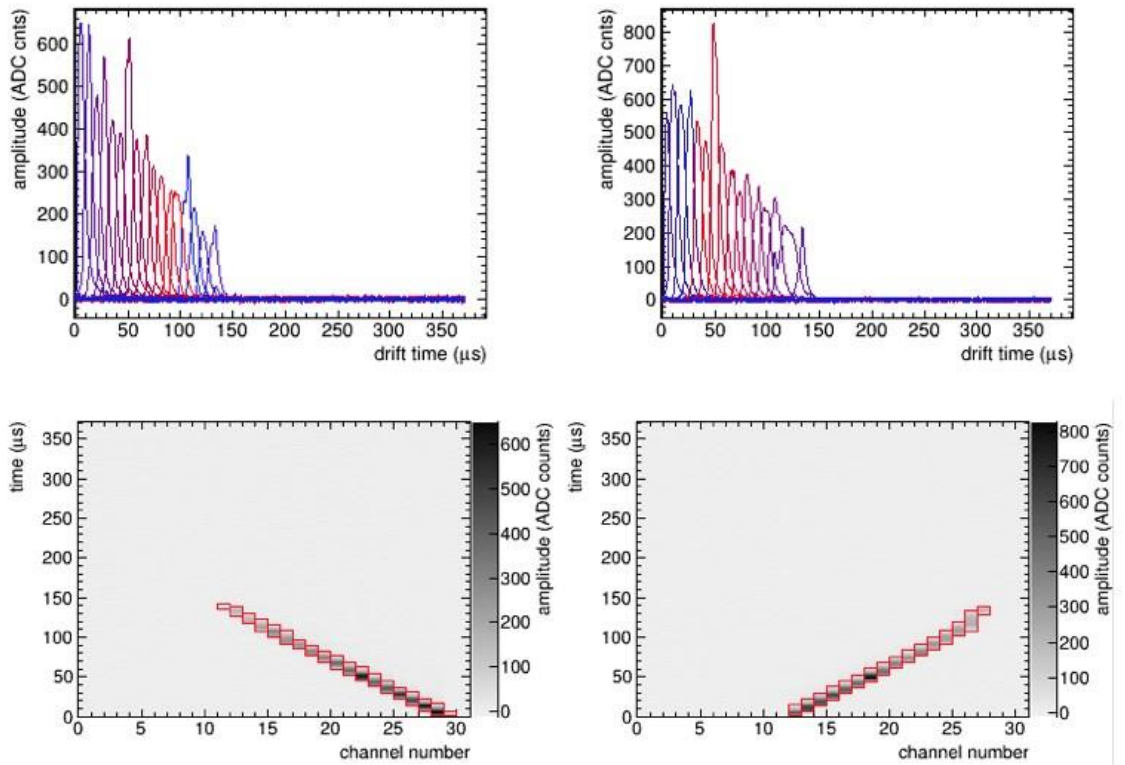


Figure 4.2: Top: event waveforms for a cosmic muon event's two views. Bottom: image plane showing the projection of the muon track onto the x-z and y-z planes.

#### REFERENCES

- [1] Resnati, Filippo. *Modeling, Design and First Operation of the Novel Double Phase LAr LEMTPC Detector*. Diss. ETH Zurich, 2012. N.p.: n.p., n.d. Web.
- [2] Lussi, Devis. *Study of the response of the novel LAr LEM-TPC detector exposed to cosmic rays and a charged particle beam*. Diss. ETH Zurich, 2013. N.p.: n.p., n.d. Web.



# Comparison of Dosimetry Methods for $^{131}\text{I}$ Treatment of Thyroid Cancer

Raymond P. Mumme<sup>1</sup>

Advisors: Thiago Lima<sup>2</sup>, Dr. Manjit Dosanjh<sup>2</sup>

<sup>1</sup>University of Notre Dame, South Bend, IN, 77450 USA

<sup>2</sup>European Organization for Nuclear Research CERN, CH-1211, Geneva 23, Switzerland

## ABSTRACT

Particle therapy is growing quickly in Europe as physicists and physicians develop new methods of cancer treatment. Simulations are utilized by both groups to predict the correct doses of radiation. In order to derive practical procedures for new and complex forms of therapy – such as light ions – the current dosimetry tools must be evaluated. In this semester project, a simple case of  $^{131}\text{I}$  therapy – a typical internal dosimetry procedure for thyroid cancer – was studied. PET images and CT scans were gathered from patients from the European Institute of Oncology to obtain the initial activity and geometries. Simulated dose maps were produced by both the Convolution Method – which assumes an infinite water medium – and the Monte Carlo Method – a FORTAN based program called FLUKA which takes into account materials in the body. These tools have been mostly developed to completion, yet there are still some issues in the coding. In the following months, the dose maps will be analyzed and converted to Dose Volume Histograms (DVHs) in order to optimize the parameters in FLUKA. The aim is an accurate and practical Monte Carlo method that can be applied to other forms of particle therapy.

## I. BACKGROUND

A SIGNIFICANT portion of time this semester was devoted to obtaining a broad understanding of the field of radiation

oncology. That background will be reviewed briefly here (See [2] for more details).

### A. TYPES OF RADIATION THERAPY

For internal treatment, there's brachytherapy – where a dose is ingested – and injection. The radiation eventually diminishes after days or hours and exits the body with the help of the kidneys.

With external therapy, a beam of particles is directed from outside the body and radiation is emitted as it travels through the patient. While X-rays (or gamma rays) are used very commonly, they are not able to deliver a high dose of radiation at an exact location. The Bragg peaks for protons and light ions, like carbon, are higher, meaning they are able to deliver radiation at a more specific penetration

depth. Therefore, there is less radiation before the tumor site is reached. (See figure 1.1).

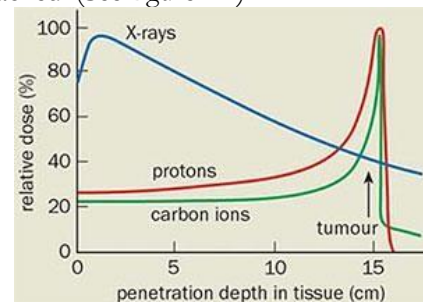


Fig. 1.1. Light ions and proton have a greater Bragg peak, or a curve shifted toward a greater penetration depth, than X-rays do.

### B. IMAGING

Gamma cameras are the basis for detecting the progress of the treatment. Gamma rays arrive from the patient, travel through the collimator, are collected by the photomultiplier tubes, and then sent to a computer, using analog to digital conversion. (See figure 1.2 below).

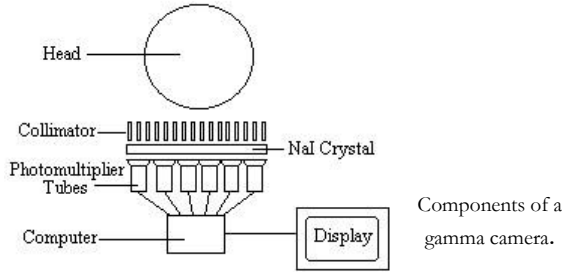


Fig. 1.2.  
basic

Gamma cameras make up several instruments, such as SPECT (single photon detection), PET (double photon detection from electron-positron annihilation), and CT (computed tomography, or 2D slices of a 3D volume). These cameras are placed on gantries, which are cranes that can move around the patient. In the case of CT, rotating gamma cameras are used to capture the slices. The main limitation of gamma cameras is the collimator, which stops much of the useful radiation and results in relatively poor images.

### C. HADRON THERAPY RESEARCH CENTERS

While the United States is mainly focusing on proton therapy, momentum for all forms of external beam therapy has been growing in Europe. ELIGHT, or the European Network of Light Ion Hadron Therapy, is working to combine all of the current knowledge on particle therapy treatment and is a collaboration between these main institutions: CERN, CNAO (Italy), Med-Austron (Austria), and HIT (Germany). Also of note: Japan is the leader of carbon ion therapy.

## II. INTRODUCTION

New cancer treatments are constantly being developed, especially in the field of particle therapy. While dose simulations are becoming increasingly accurate, the computing time is increasing as well [1]. In addition, hospitals do not have consistent technology among themselves and among the medical physicist community. Commonly used tools for dosimetry nowadays are Monte Carlo – for both internal and external dosimetry – and a Treatment Planning System (TPS), which is useful for external beam therapy.

In this project, several methods of dosimetry simulations are compared to determine the most practical tool. While the aim is to improve external therapy simulations, a basic, internal treatment will first be analyzed, with the results to be eventually utilized in external therapy. <sup>131</sup>Iodine Therapy is a common procedure for thyroid cancer [7]. The radiation is given by:

$^{131}\text{I} \rightarrow ^{131}\text{Xe} + e^- + \gamma$  (beta and gamma radiation) In order to estimate the effects of <sup>131</sup>iodine

without actually administering a dose, a trace amount of <sup>124</sup>iodine will be given to patients to obtain images, based on the methods in [7]. After analysis of the dosimetry simulations, the correct amount of <sup>131</sup>iodine will be given to the patients. To make the conversion between the activities of <sup>124</sup>I and <sup>131</sup>I, a simple exponential factor is used (see [7]).

$$A_{131}(x,y,z,t) = A_{124}(x,y,z,t) \cdot e^{\lambda_{124}t} \cdot e^{-\lambda_{131}t}$$

where  $A$  is the activity of the isotope (or the PET image), and  $\lambda$  is the decay rate, which is based on the half life from first-order kinetics.  $\lambda_{124} = \ln(2)/4.18$  days, and  $\lambda_{131} = \ln(2)/8.04$  days. This equation assumes that the biological half lives of the two isotopes are equal.

The simulation tools for this internal dosimetry will be Convolution and Monte Carlo, to be developed with images from patients already treated with <sup>131</sup>I. Once the tools are complete, they will be applied to images from patients who were imaged with <sup>124</sup>I. After analysis, the Monte Carlo Method will be optimized for practicality.

## III. METHODS AND MATERIALS

### A. THE MIRD METHOD

(See [2] for more details)

For internal radiation dosimetry, the widely accepted MIRD method – developed by the Medical Internal Radiation Dose Committee of the Society of Nuclear Medicine – has been used to calculate the radiation deposited to a target. While a classical method gives similar results, the absorbed fraction (more generally the MIRD) method is more accurate and versatile due to the ability to calculate the delivered dose from several source organs (areas with above average radioactivity concentrations) in the body.

The MIRD method involves three steps:

1) Calculation of the cumulated activity, or the activity (decays/second, or Bq) integrated over time. (Units in Bq s)

$$\tilde{A} \approx \int_0^{\infty} A(t) dt \quad \text{where} \quad A(t) = A_0 e^{-0.693t/T_p}$$

$$\frac{1}{T_e} = \frac{1}{T_p} + \frac{1}{T_b}$$

The activity is based on first order decay and the physical half life  $T_p$ , yet if the biological half life  $T_b$  becomes significant, than the effective half life is used.

2) Calculation of the emitted energy per cumulated activity from the source organ(s).

$$\Delta_i = N_i E_i \text{ (Gy kg /Bq s)}$$



$E_i$  is the average energy emission for every  $i$ th source of radiation, and  $N_i$  is the relative frequency of emissions per decay.  $\Delta_i$  is multiplied by the cumulated activity to obtain the total energy emitted (J or Gy kg)

3) Calculation of the fraction of energy emitted that is absorbed by the target organ. This total absorbed dose is given by

$$\tilde{A} \sum_i \phi_i(r_k \leftarrow r_h) \Delta_i$$

where  $\phi_i$  is the fraction for an  $i$ th source of radiation,  $r_k$  is the target organ, and  $r_h$  is the source organ. When the target organ is the source organ,  $\phi_i = 1$ .

The mean absorbed dose is (in Gy):

$$\bar{D}(r_k \leftarrow r_h) = \frac{\tilde{A}}{m_t} \sum_i \phi_i(r_k \leftarrow r_h) \Delta_i$$

where  $m_t$  is the mass of the target organ.

Often, the calculation is simplified by defining the S factor, or the mean absorbed dose per cumulated activity (in Gy/(Bq s))

$$S(r_k \leftarrow r_h) = \frac{1}{m_k} \sum_i \phi_i(r_k \leftarrow r_h) \Delta_i$$

This finally gives us the mean absorbed dose (in Gy):

$$\bar{D}(r_k \leftarrow r_h) = \tilde{A} \times S(r_k \leftarrow r_h)$$

These calculations are made with average anatomic sizes and shapes in mind. Step 3 depends on knowing the sizes and distances between organs, which varies from patient to patient. S factors assume average sizes of the human body, which doesn't lead to always accurate results. Step 1 is also difficult to calculate since the activity in different patients' organs varies due to variations in metabolism.

---

## B. THE CONVOLUTION METHOD (2D/3D)

---

(See [5] for more details)

Often when dosages are calculated by computers, the Convolution Method – a modification of the MIRD Method – is employed. The mean absorbed dose at a certain point in time can be represented by the convolution of the activity and the S factor integrated over volume (units in cGy/s):

$$\dot{D}(r) = \int_V A(r') \otimes K(r-r') \cdot dV' \quad (\text{in Gy/s})$$

which can be solved by the convolution theorem with Fast Fourier Transforms (FFT).

$$\dot{D}(r) = FFT^{-1}[FFT\{A(r)\} \cdot FFT\{K(r)\}]$$

$A$  is the activity matrix of the voxel, and  $K$  is the point dose kernel which is considered to be the S factor (the absorbed dose per decay at a distance from the source organ).

The point dose kernels were generated in an infinite water medium by Monte Carlo methods as by Furhang et al (1996) [3]. For this project, their fit parameters were inserted into the code to obtain the S factor:

$$K(r) = \sum_i^{i_{\max}} \left( \frac{a_{-2}}{r^2} + \frac{a_{-1}}{r} + a_0 + a_1 \cdot r + a_2 \cdot r^2 \right) e^{-m_i \cdot r}$$

(1.1)

where  $a_{-2}$ ,  $a_{-1}$ ,  $a_0$ ,  $a_1$ ,  $a_2$ , and  $m$  are parameters specific to an isotope  $i$ , and  $r$  is the distance. The units are cGy/(Bq s).

---

## C. MONTE CARLO METHOD

---

Monte Carlo techniques record the histories of particles and ions during simulations. It uses known probabilities and distributions to predict the resulting parameters of events within a 6D phase space ( $x, y, z, \theta, \varphi, E$ ). Although the technique has the greatest accuracy, it also has an immense processing time. However, employing the MC technique in clinics has become more affordable [1].

FLUKA is a software package developed by CERN and INFN with FORTRAN. The Monte Carlo Method uses FLUKA to generate events from particles interacting with matter, whether it is internal or external radiation. Geometries from CT scans, radioactivity concentrations from PET images, and user routines help build a simulated dosage. Flair is an easier-to-use interface for FLUKA, allowing simulation runs without the need to code every single line.

---

## D. TIME INTEGRATION AND KINETICS

---

Once these methods are developed for a volume of image slices at one point in time, a series of images at different time points can be integrated over time to trace the radiation in



the body, modeled by a simple curve from kinetics [2].

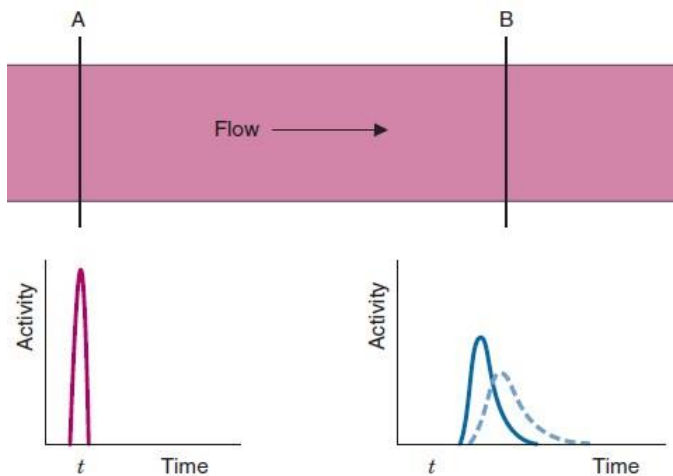


Fig. 3.1. The compartment model for kinetics. At point B, the activity curve is shown on the right. The solid line represents a greater flow than the dashed line.

---

### E. THE CODING PROCESS

---

Because our group already has a user routine for FLUKA, the convolution method needed to be developed. All of the following was done with Python 2.7.

a) Test Images: PET and CT scans (47 slices) of a water voxel simulating a body were obtained from Churchill Hospital, Oxford. The 256x256 pixel PET images, given in Bq/mL, represents the activity of 131-iodine. These DICOM images contain several bits of information about the scan, including slice location, slice thickness, pixel spacing, etc. Images were sorted by slice location (in mm) starting at the lowest slice (usually a negative value, closest to the feet of the body). The test images were mainly for viewing purposes: the body contained fake tumor sites in order to grasp the concept of volume activity as one scrolled through the slices.

b) Patient 1 Data: A set of ninety-three 256x256 PET (68Gallium tracer) and CT scans (each) of Patient 1 were obtained from the European Institute of Oncology, Milan. Once again, images were sorted by the slice location. After, a look-up table for the image pixels was created, giving their distances from the center of the image. Each x and y value was multiplied by the pixel spacing in order to obtain the distance in cm. For each pixel and its distance, the point dose kernel was generated using equation (1.1) and the parameters for 131-iodine in [3].

The PET activity matrices were modified. A DICOM correction factor was used to change the units of the PET images from Bq/ml to Bq. Finally, they were

convolved with the point dose kernels at each pixel using FFT to obtain the dose map for each slice. The 2D Convolution Method only computes the distances from the center of a slice (x and y) and then only considers the activity from surrounding pixels on that slice. The 3D Convolution method, however, computes the distances from the center of the slices (using the value for slice thickness also) and then considers the activity from all of the slices. The 3D method is the one used further in the analysis.

c) Patient 2 Data: Another set of three hundred and thirteen 256x256 PET (FDG, or fludeoxyglucose, tracer) and CT scans (each) were obtained from the European Institute of Oncology. The last set of images was only considering the dose from gamma radiation of 131-iodine. Next, the method must be corrected for the beta (or electron) radiation. The fit provided in [3] was solely for gamma kernels, so beta curves from Prestwich et al. (1989) were used (see [6]). Based on their data of distances and kernels, a fit was applied to obtain parameters like in function (1.1). The beta and gamma point kernel functions were added and then convolved with the modified activity matrices.

d) FLUKA: Header and material files were inserted as input, as well as the CT scans for the input geometry. The PET images provided the activity. Test simulations were performed with a group user routine, consisting of 140 million events collected over an average of 6 hours. Results for each pixel were in MeV/g/decay which was converted to Gy/decay (or J/kg/decay) by multiplying the data by a factor of  $1.6 \times 10^{-7}$ . Finally, all of the pixels were multiplied by the primaries, or the sum of the activity (decays/s) in all of the slices, leading to units of Gy/s.

---

### F. OPTIMIZATION

---

The last part of the project – once all of the methods start producing reliable results – involves optimizing the number of Hounsfield parameters in the user routine in order to reduce the computing time. These parameters are specific units derived from the radiodensity of materials and organs in the body. There are 21 parameters in the header input file. The plan is to reduce the number of parameters for a number of runs and witness the changes in dose-volume histograms (DVHs), which will be built to analyze the body dose distributions.

---

## IV. RESULTS AND DISCUSSION

---

### A. TEST IMAGES

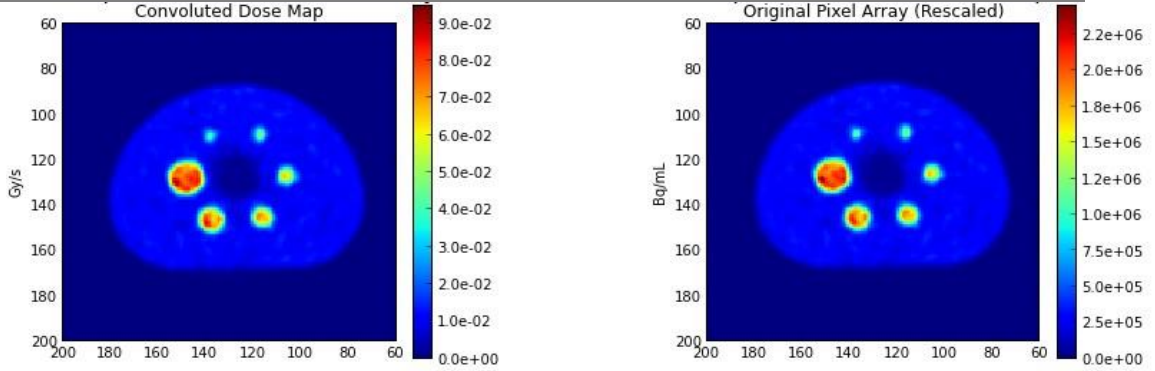


Fig. 4.1. Comparison between Original Pixel Array and Convolved Dose Map (Slice 23). Note that although the images don't appear to change much, the magnitudes have changed.

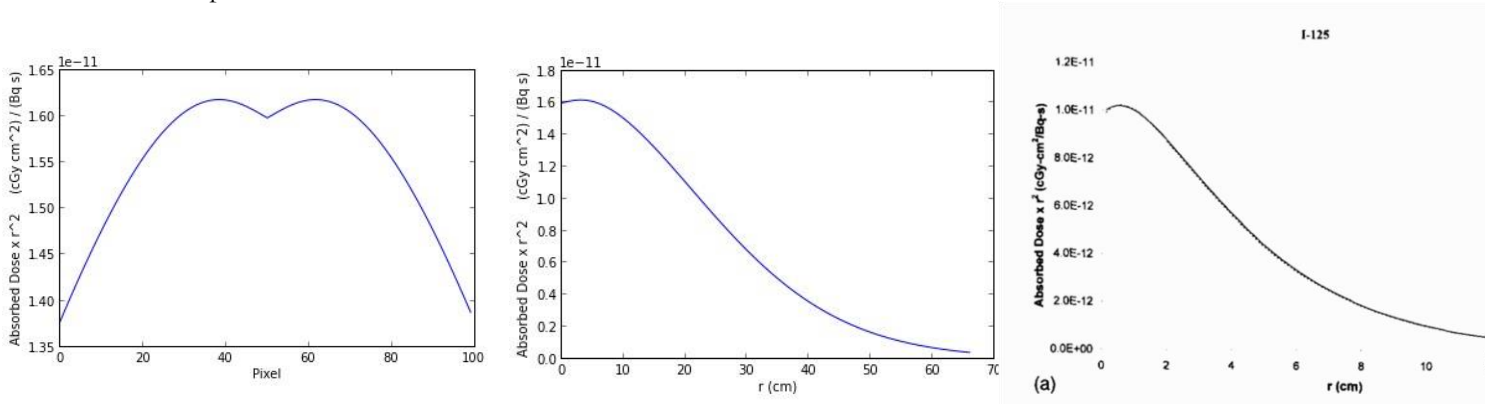
As mentioned in the Methods section, these images were mainly tests to develop the 2D Convolution Method. Clearly, there is a difference between the activity and dose deposited, though the “hot spots” of the image don't shift. The activity is basically smoothed out and distributed to the surrounding pixels. This is seen in the next section.

---

### B. PATIENT 1 DATA

---

After creating the gamma point dose kernels, they were multiplied by  $r^2$  and then plotted. This  $r^2$  provides a more visible curve of what is occurring: the dose at a single point is distributed to surrounding points. Without the  $r^2$ , there would be a spike at



the center showing the distribution is very local, which is the case.

Fig. 4.2. The graph to the left shows that at the center x pixel, the absorbed dose times  $r^2$  decreases in the y direction away from the center after a small increase in the beginning. The right graph is similar but uses distances in cm.

The center graph's shape in figure 2 matches that of the graphs in [3] (such as for 125-iodine in the right image). In the 3D Convolution Method, the modifications are made to include all of the slices. A kernel in the center of the image is below.

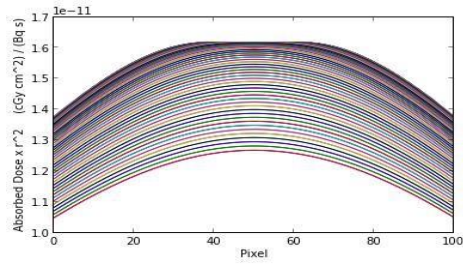


Fig. 4.3. The 3D dose kernel in the y and z directions.

The following series are examples of the images produced by the 2D Convolution Method, the 3D Convolution Method, and the Monte Carlo Method. They are selected from parts of the body between the shoulders and head, in slice order.

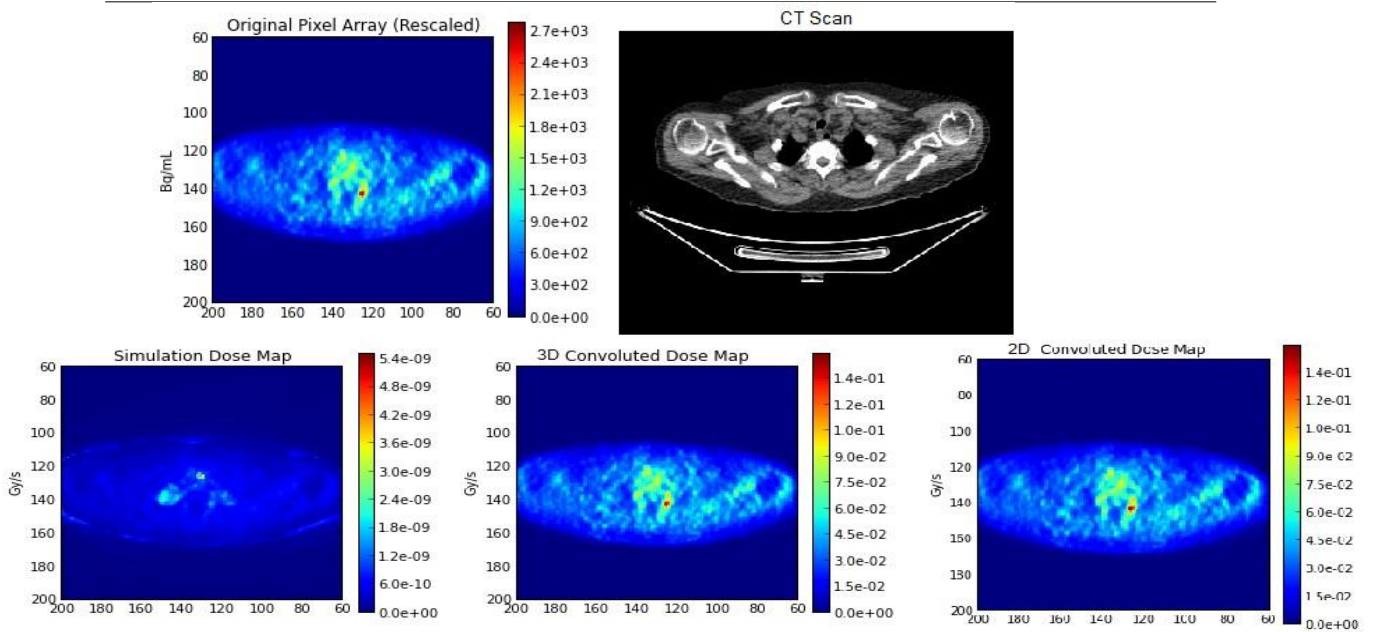
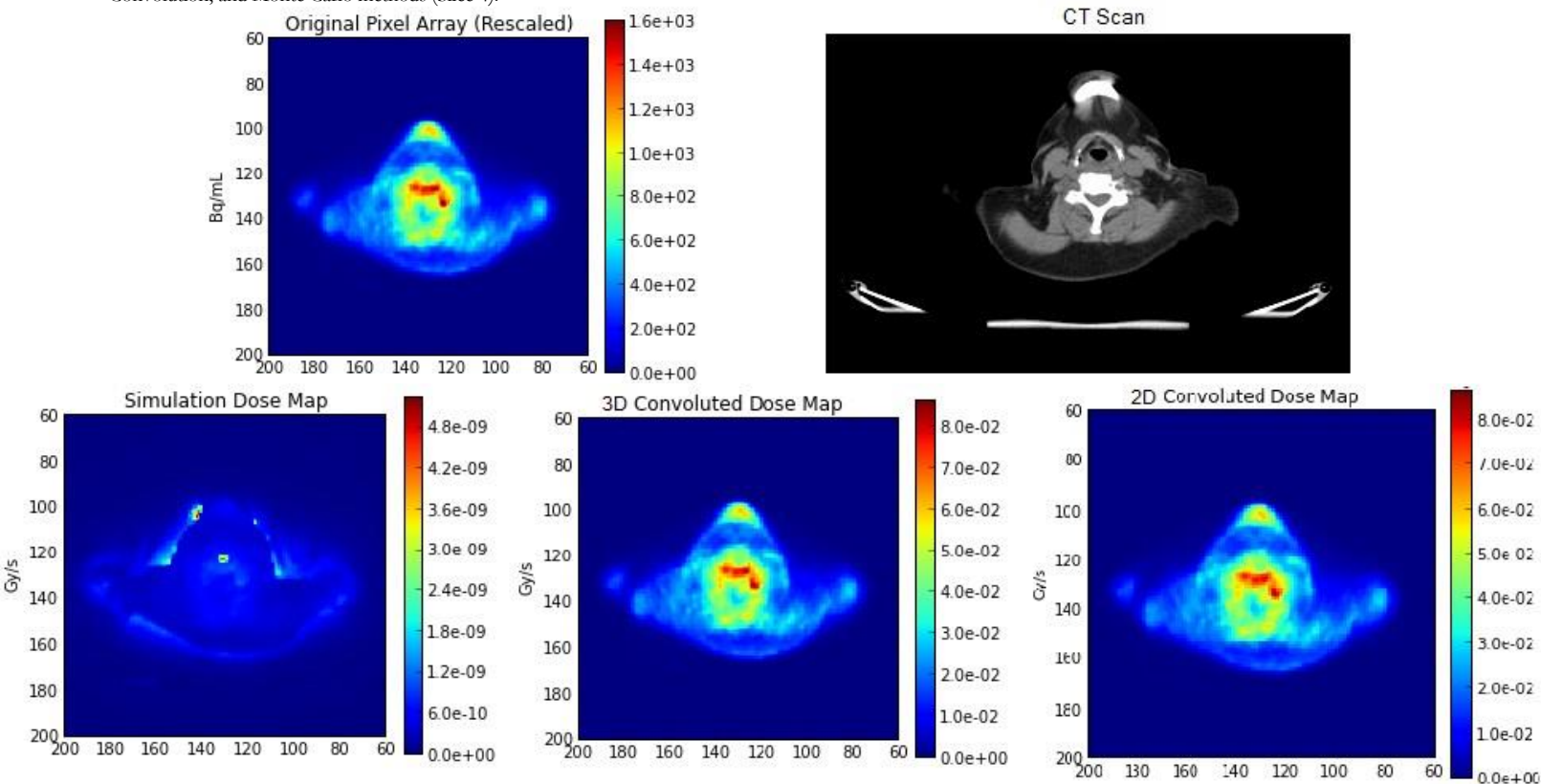


Fig. 4.4. Top two images: Original PET activity array and CT scan of the shoulders. Bottom three images: Comparison between 2D Convolution, 3D Convolution, and Monte Carlo methods (Slice 17).

Convolution, and Monte Carlo methods (Slice 4).



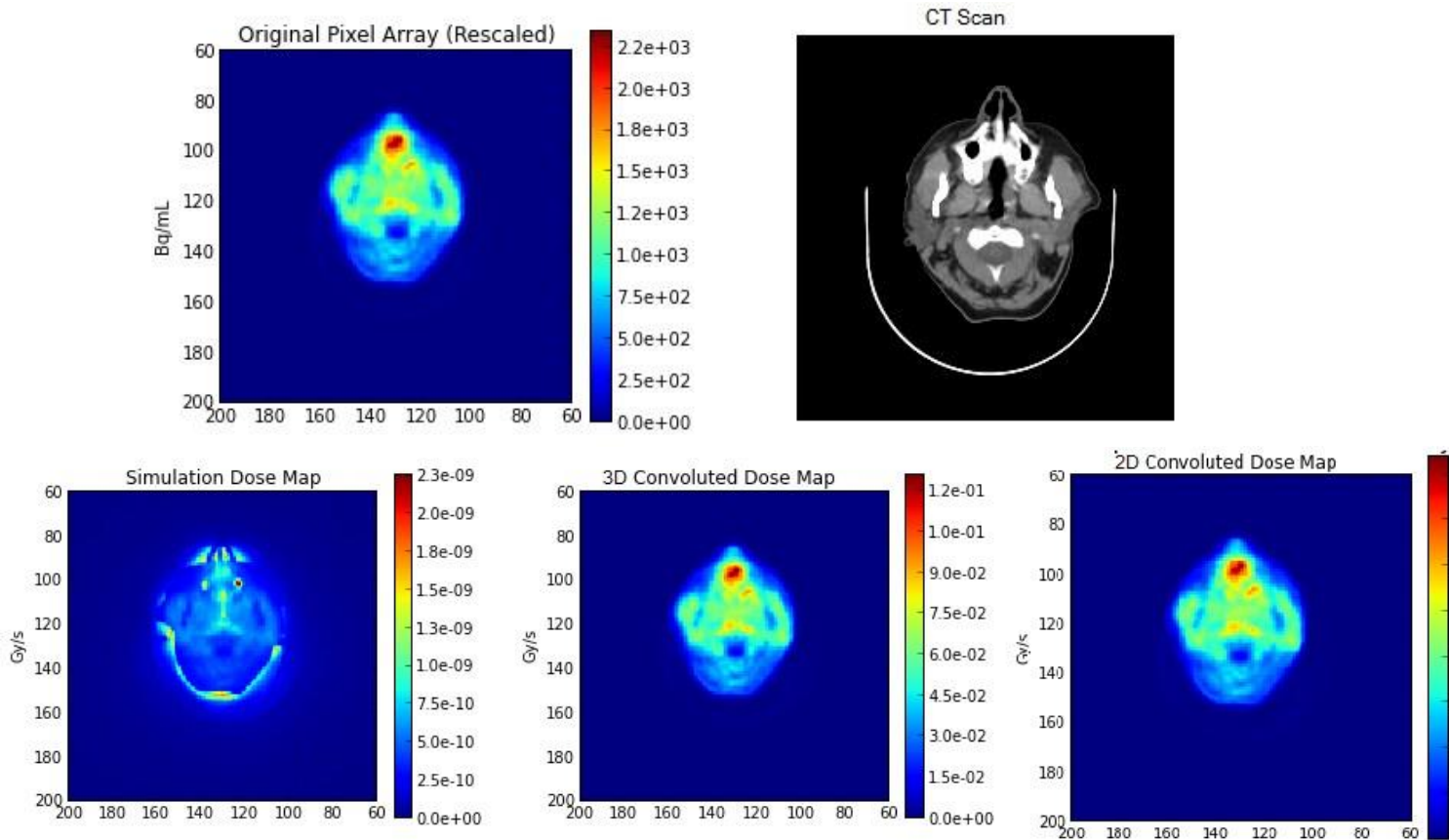


Fig. 4.6. Top two images: Original PET activity array and CT scan of the head. Bottom three images: Comparison between 2D Convolution, 3D Convolution, and Monte Carlo methods (Slice 36).



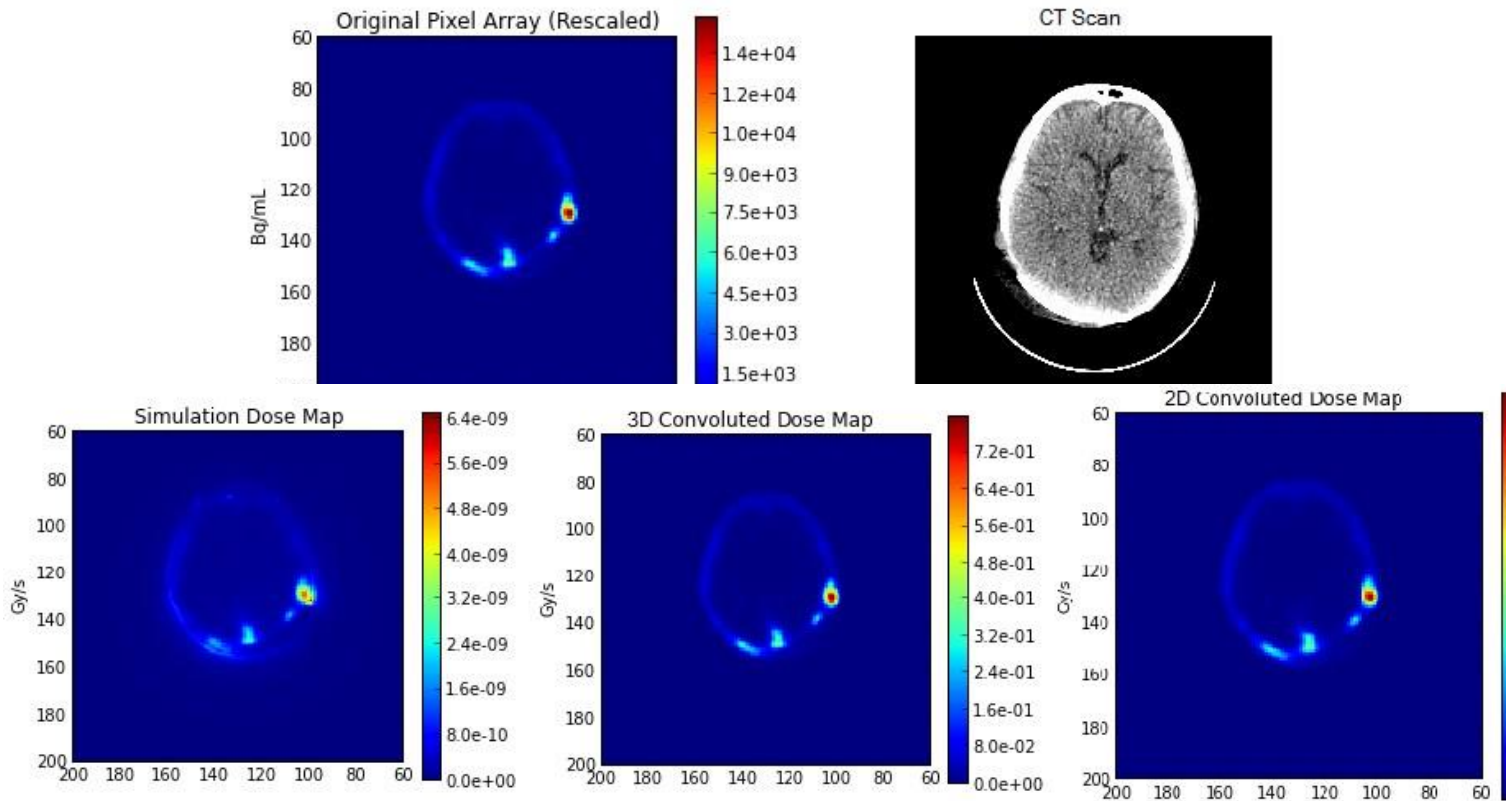


Fig. 4.7. Top two images: Original PET activity array and CT scan of the head. Bottom three images: Comparison between 2D Convolution, 3D Convolution, and Monte Carlo methods (Slice 58).

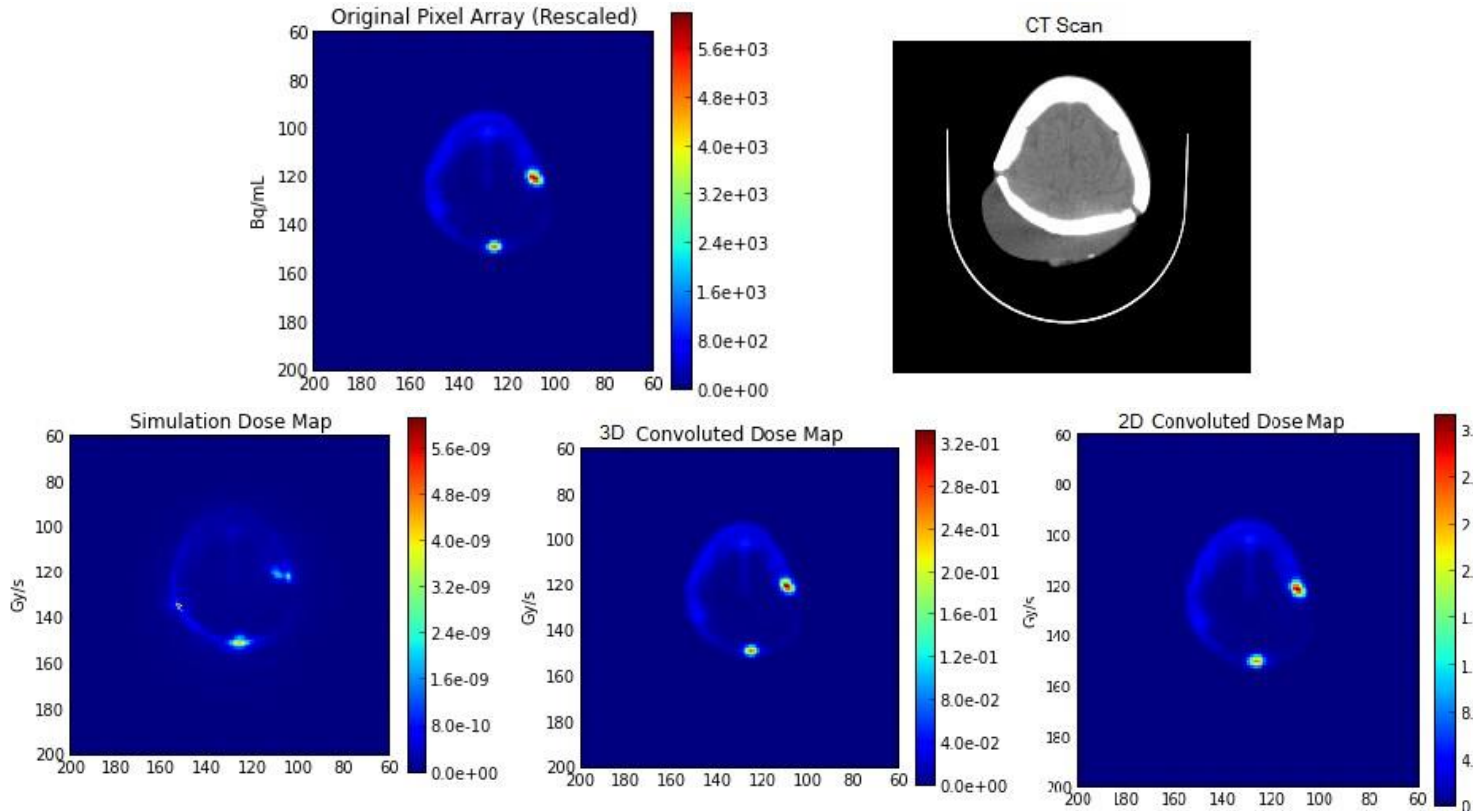


Fig. 8. Top two images: Original PET activity array and CT scan of the head. Bottom three images: Comparison between 2D Convolution, 3D Convolution, and Monte Carlo methods (Slice 74).

A full analysis has not been performed yet because these methods are still being developed. But some brief analyses will be discussed here. In many cases, the 2D and 3D convoluted dose maps are very similar – their magnitudes barely changing. However, there may be some differences, like the magnitudes in figure 4.7. Again, the convolution method smoothes out the activity, so there is not much difference from the original PET images. Yet, there may be errors in the addition of the z, or slice, component in the 3D convolution, which is currently undergoing evaluation.

There are certainly differences between the Monte Carlo and Convolution dose maps. Even though the units of Gy/s are the same, the values differ by 8 orders of magnitude! Several sources of error are being looked into. The user routine may be the issue. FLUKA produces results in GeV/g/decay. In order to convert to Gy/s or J/kg/s, the results must be multiplied by a factor of  $1.6E-7$  and then multiplied by the number of primaries, or decays/s, in all of the slices of the original image. However, these modifications have already been applied, yet the magnitudes are still not matching. The user routine will continue to be evaluated.

Further, the hot spots among the Monte Carlo and convoluted images differ. If one looks close enough, the lighter shades of the Monte Carlo image tend to match with the hot spots of the convoluted image. Yet, there seem to be extra, brighter shades in the Monte Carlo images. Much of this can be explained by the methods. The Convolution method assumes an infinite water medium, yet FLUKA includes the materials of the body, like bone and tissue. In this way, the FLUKA method is more accurate, yet it is also very time consuming. The Convolution method images will act more as a control variable to see how much the FLUKA images change after changing the number of Hounsfield parameters.

---

### C. PATIENT 2 DATA

---

Since there are 313 slices of a whole body scan for this patient, a section of 89 slices in the bladder area was chosen to reduce the volume, thus making the FLUKA results more accurate over a shorter time. Also, because the bladder contains liquid from the rest of the body, it's an interesting area for activity. With the PET and CT scans from Patient 2, the Convolution method was modified to include the beta radiation in addition to the gamma radiation already in place. Fitting the data points for 131iodine from Table 4 of [6] led to the parameters below, with a form similar to function (1.1).

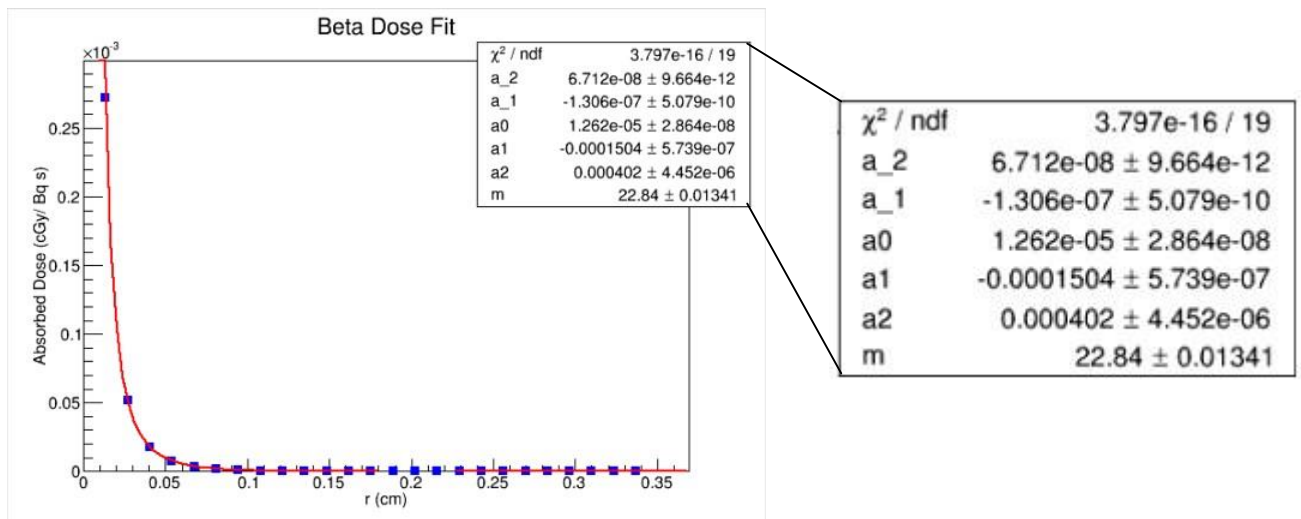


Fig. 9. The fit and parameters for the beta dose kernel.

An example of the images  $\phi$  different methods:



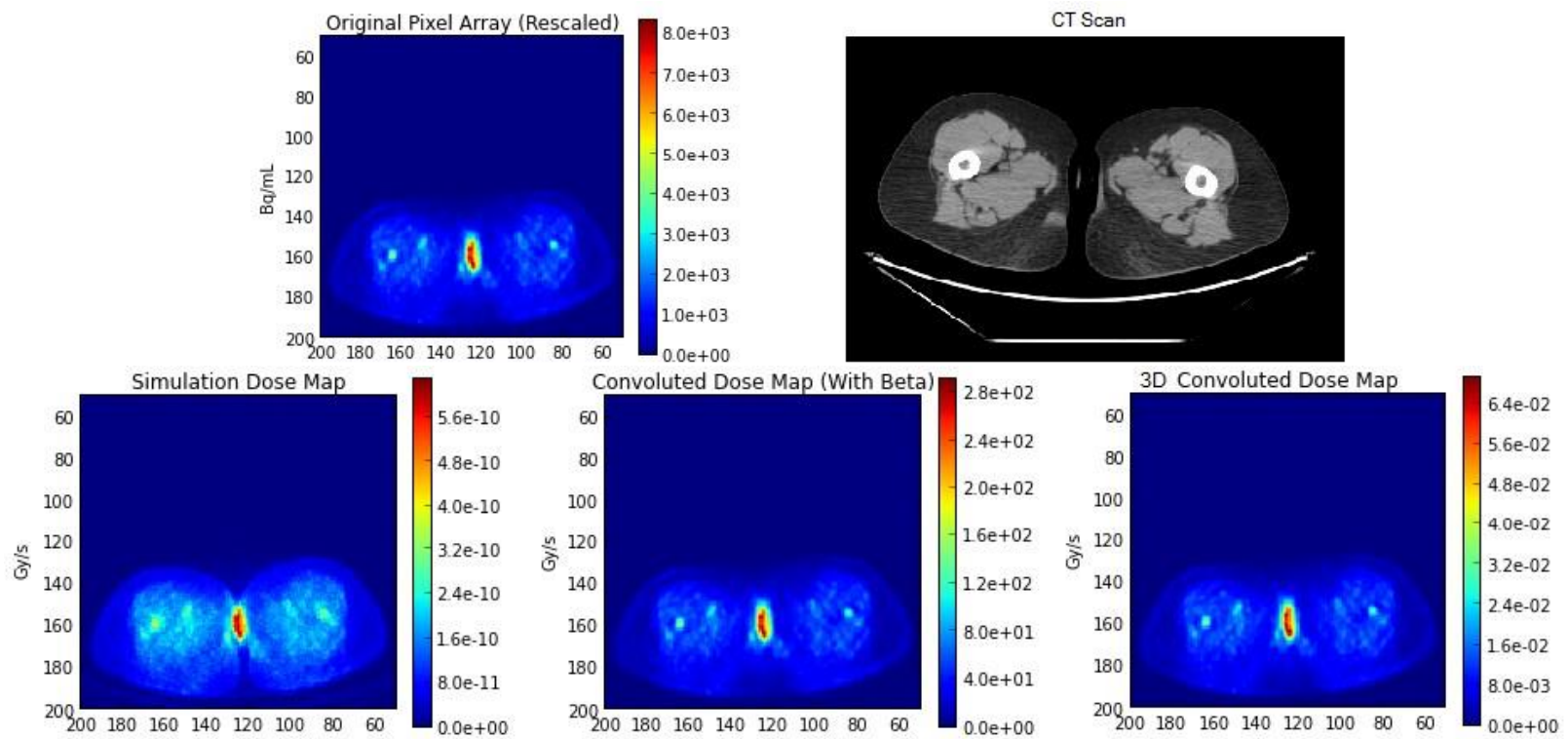


Fig. 10. Top two images: Original PET activity array and CT scan of the legs and bladder. Bottom three images: Comparison between 3D Convolution, 3D Convolution with the Beta Radiation, and Monte Carlo methods (Slice 29).

With the added beta dose, the convoluted image is now 12 orders of magnitude above the FLUKA image. Again, the user routine is probably a factor in why the magnitudes are so off. Yet the majority of the dose hot spots are pretty similar.

## V. FUTURE

This summer, the methods will be tested until they function properly. After these tools are completed, a rigorous analysis will be carried out. The plan is to gather a series of slices at different times for different patients. After obtaining the convoluted and Monte Carlo images, the results will be converted into Dose Volume Histograms over several tumor sites and then compared. This comparison will continue for each reduction of the Hounsfield parameters in the FLUKA user routine. We hope to

---

maintain the accuracy until a limit is approached, at which the computing time should be significantly faster.

## VI. PERSONAL STATEMENT

While this semester has been mostly background reading and coding, the summer will be full of analysis and paper writing. I have developed a basic knowledge of the field of radiation oncology and I have taken the first steps toward my career as a medical physicist and physician. I was able to start a project well aligned with my interests and now I will be able to carry out the rest of that project.

## ACKNOWLEDGMENT

I would like to thank the University of Notre Dame and Boston University for accepting me into this abroad program, Dr. Augusto Ceccucci for aiding me extensively in choosing this project, Dr. Manjit Dosanjh for allowing me to join her ENLIGHT team, and Thiago Lima, who is my mentor and has guided me through the work this semester. Finally, I would like to thank Notre Dame President's Circle alumni who are funding this work for the summer.

## REFERENCES

- [1] T.T. Böhlen, J. Bauer, M. Dosanjh, A. Ferrari, T. Haberer, K. Parodi, V. Patera, A. Mairani. "A Monte Carlo-based treatment-planning tool for ion beam therapy," *Journal of Radiation Research*, vol. 54, 201, 77-81
- [2] S.R. Cherry, J.A. Sorenson, and M.E. Phelps. *Physics in Nuclear Medicine*. Philadelphia: Elsevier Saunders, 4<sup>th</sup> ed, 2012.
- [3] E.E. Furhang, G. Sgouros, and C. Chui. "Radionuclide photon dose kernels for internal emitter dosimetry," *Medical Physics*, vol. 23, no. 5, 1996, 759-764.
- [4] K.S. Kolbert, G. Sgouros, A. M. Scott, J.E. Bronstein, R.A. Malane, J. Zhang, H. Kalaigian, S. McNamara, L. Schwartz, and S. M. Larson. "Implementation and evaluation of patient-specific three-dimensional internal dosimetry," *The Journal of Nuclear Medicine*, vol. 38, no. 2, 1997, 301-308.
- [5] J.S. Lampinen, H.K. Pohjonen, and S.E. Savolainen. "Calculating internal dose by convolution from SPECT/MR fusion images," *Annals of Nuclear Medicine*, vol. 12, no. 1, 1998, 1-5.
- [6] W.V. Prestwich, J. Nunes, and C.S.Kwok. "Beta dose point kernels for radionuclides of potential use in radioimmunotherapy," *The Journal of Nuclear Medicine*, vol. 30, no. 6, 1989, 1036-1046.
- [7] G. Sgouros, K.S. Kolbert, A. Sheikh, K. S. Pentlow, E.F. Mun, A. Barth, R.J. Robbins, and S.M. Larson. "Patient-Specific dosimetry for <sup>131</sup>I thyroid cancer therapy using <sup>124</sup>I PET and 3-dimensional-internal dosimetry (3D-ID) software," *The Journal of Nuclear Medicine*, vol. 45, no. 8, 2004, 13661372.

## **Report on Work at the ISOLDE Decay Station**

Guy Rosin

Supervisors: Elisa Rapisarda, Christophe Sotty.

### **Introduction**

The ISOLDE Decay Station is an experimental setup to study radioactive nuclear decay. The particular focus of the setup is to detect the products from different types of decays. As a result, we would be better able create more refined models of the atomic nucleus. Understanding of radioactive nuclei is applied for studying a large range of problems in nuclear, atomic, surface and solid state physics, nuclear medicine and astrophysics.

The Decay Station involves several detectors to measure the decay products of exotic isotopes. These isotopes are particularly unstable nuclei that have a half-life of seconds to picoseconds. Stable nuclei have a proton to neutron ratio of about 1:1 for small masses and about 2:3 for larger nuclei. An exotic nucleus has a very short half-life because of the overabundance of either neutrons or protons. A nucleus with an unstable configuration will quickly decay into a more energetically favourable daughter nucleus. The most common types of decay are alpha, beta and gamma decays. Alpha decay is when a helium nucleus, two protons and two neutrons, is emitted from the nucleus. Beta decay is when a neutron decays into a proton and a beta particle, or a proton decays into a neutron and a beta particle. In the first case, the beta particle is an electron, in the second case, it's a positron. Finally, a gamma decay is when the nucleoids go from an energetic state to the ground state and emit a gamma particle, high energy photons.

The apparatus in ISOLDE uses a proton beam from the Proton-Synchrotron Booster to create a beam of neutral radioactive ions. The proton beam from PSB is launched at the primary target, which is usually made up of heavy nuclei such as Uranium. The proton

beam hits the primary target and produces exotic nuclei through fission, fragmentation and spallation. The desired isotopes for the experiments are ionized through specific laser frequencies and extracted. The beam of radioactive nuclei is diverted to the detector setup, far from the primary target to avoid background radiation. The process is illustrated in Figure 1 below.

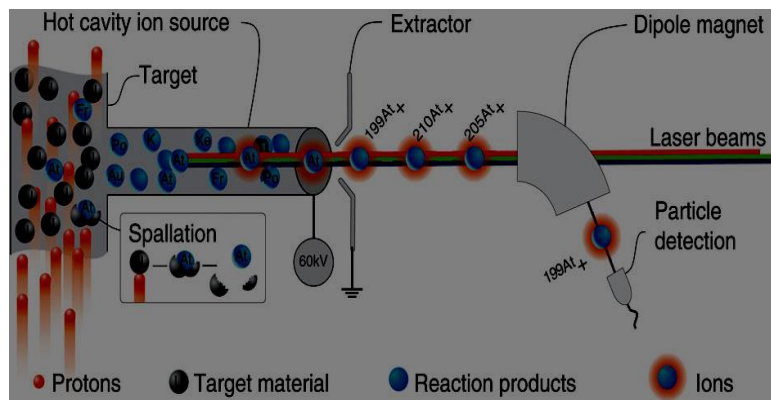


Figure 1: Isotope producing process

The principle detectors of the Decay station are the Germanium detectors, LaBr<sub>3</sub> Scintillators and plastic detectors. The Germanium detectors' main use is to detect gamma radiation. they do this by using the photoelectric effect, as gamma photons knock electrons, they create a current directly proportional to the energy of the gamma radiation. Germanium detectors have a high energy resolution, which reduces unwanted background noise. The scintillators, devices that fluoresces from radiation, are also used to measure gamma radiation. The scintillators have a higher response time than the Germanium detectors, so they can be used to measure faster decays, on the order of nanoseconds to picoseconds. Finally, the tape station setup in the IDS is used to collect radioactive decay products and move them to a lead containment, since the decay products can still give off radiation which can skew the detector readings.

Between the radioactive ion beam and the detector setup is the diagnostic box, which contains a faraday cup and collimator. A collimator is used to narrow the beam by excluding particles that have a relatively large transverse momentum. A faraday cup is a metallic cylinder that can measure how many charged ions go through it

## **Methods and Discussion**

My contribution to the project was to make a Computer-Aided (CAD) drawing of the experiment area in Isolde where the Decay Station setup is located. The process of making a CAD drawing involves designing several parts, putting those parts together in an assembly, and then putting these assemblies in a larger assembly. To make the drawing, I went to Isolde to take the measurements of the area, and used them to create drawings of the parts and the assembly, including technical drawings of the assembly that show the dimensions between all the components. I then went back to Isolde and measured the

---

dimensions to assess the degree of their accuracy. I repeated this process until the measured difference was less than five millimetres.

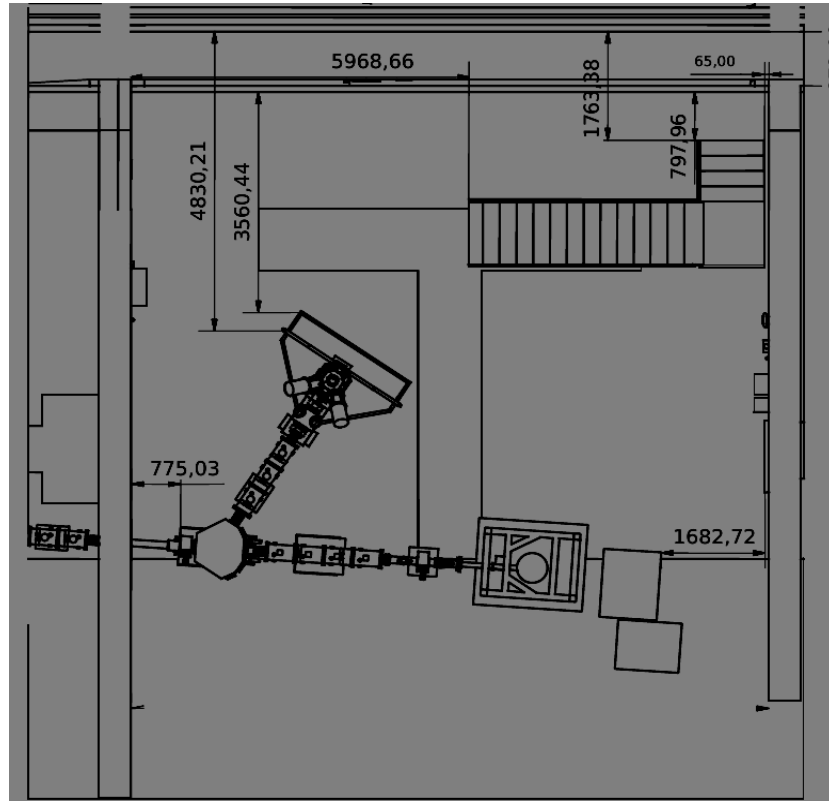
The model of the experiment area included the beam line separator, the decay station setup, the Nicole setup (a different experiment from ours) and various components around it including the extended beam line and the cooling apparatus. The other important details of the CAD model were the security concerns in the area such as the fire extinguisher, the grounded cable, and the electrical equipment. The drawing would be used to analyse the environment of the experiment area, to see how much space is there for the equipment we would want to use in the experiment. It would help the companies that manufacture equipment determine how large the set up needs to be. Additionally, the CAD will have shown the distance from the beam lines and the detectors to the electrical outlets and the grounding cables to determine where to place the equipment within reach. The drawing would be used to make sure that the area follows safety regulations, for example, the liquid nitrogen system has to be a certain distance from the electrical outlets in case of accidents.

My starting point was an outdated CAD drawing made before recent renovations. The first thing I did was to make the old CAD more modular by separating out the different components of the area: the walls, the ceiling, the stairs, the floor, and the Nicole boundaries. This makes it easier to adjust one of the parts without changing the whole structure. To make the different parts I recreated several versions of the drawing and extracted the only part I needed, the front wall, back wall, side walls, floor, ceiling and the sides of the experimental area. The parts were then reassembled in a new assembly with adjusted measurements.

I went around the experiment area in Isolde to measure the distances of the components in the area. The measurements included detailing of the new stairs; the new angle of the beam line, including the angle with respect to the vertical wall, the distance between the walls, the height of the roof and the safety equipment.

The beam line is the sets of electric and magnetic charges that redirect the ion beam coming from the primary target on the other side of Isolde to the detector setup. The beam

line for the planned experiment involved three focusing quadrupoles instead of the two that were already set up, so an additional focusing quadrupole was added. The beam line comes from the isotope separator, the hexagonal shape in the bottom right of Figure 2 below. The beam is redirected towards the detector setup, about 4800 millimeters from the wall.



---

Figure 2: View of The experimental area.

Since I was inexperienced with drawing computer models, making new stairs was the first exercise. My first attempt is seen below (Figure 3). It was aesthetically okay, but the measurements were significantly off. After the first sketch, I made technical drawings to show the dimensions of the stairs, the railings and the platform, and went back to check them in ISOLDE. After rechecking the dimensions, I edited the width of the stairs, which created contradicting dimensions elsewhere in the drawing. I split up the drawing to several parts and continued this process of refining the measurements of individual parts until the error was within about five millimetres.



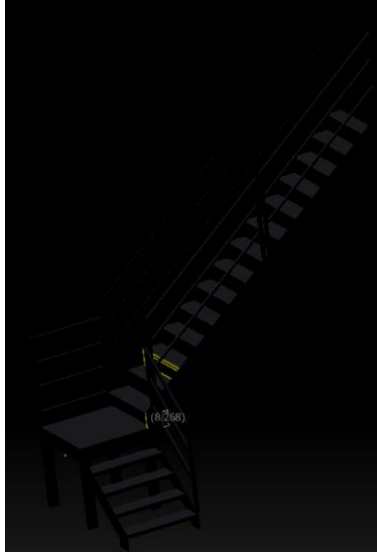


Figure 3: First model of staircase

I made models of the rest of the components of the experiment area; the emergency buttons, fire extinguisher, emergency telephone, radiation level detectors, grounding cables, electric box, the beam line and the decay station. The beam line was changed to be angled at .067 radians from the perpendicular and another focusing quadrupole was added for the experiment. Finally, I made technical drawings of all the parts to easily show the dimensions of the area for the future when/if the experiment is carried out. After the three dimensional models, I made technical drawings of each component of the experimental area. In a technical drawing it is possible to see all the dimensions of each component through different perspectives. It is very important for a dimensional drawing to be user-friendly, easily readable and follow conventions, for example, all the dimensions should be aligned, as shown in Figure 4 below.

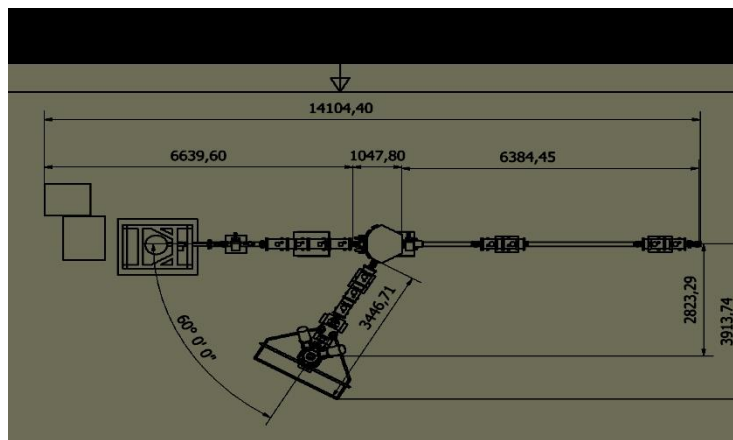


Figure 4: Technical drawing of the NICOLE area

## Conclusion

The technical drawings can be used as blue prints for future uses and to demonstrate that the area follows all safety procedures (Figure 5).

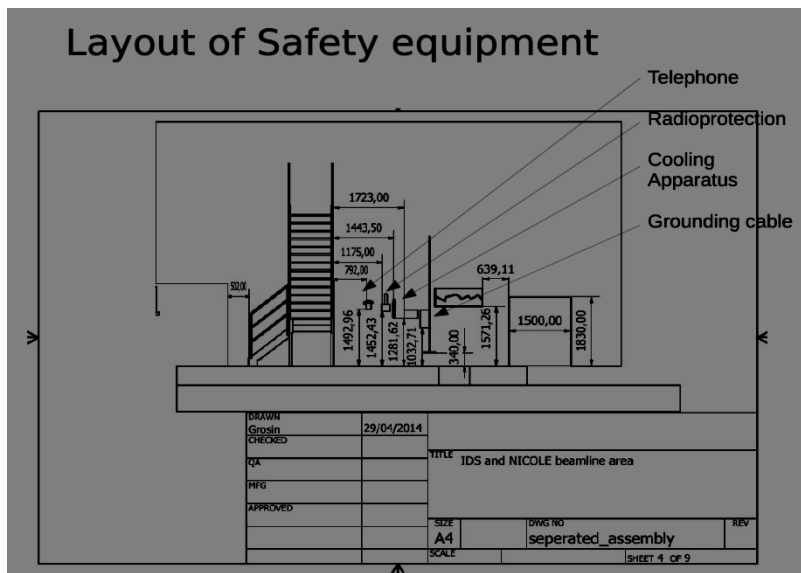


Figure 5: Safety equipment

Two examples of the model drawings are shown in Figure 6 and Figure 7 below. The first is showing where the experiment area is in Isolde, the second in a front view of the experimental setup drawing

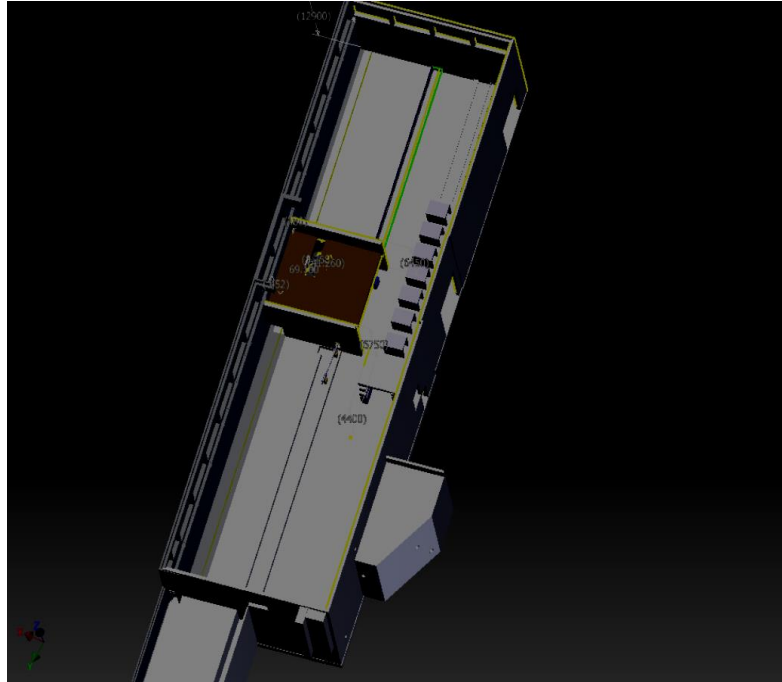
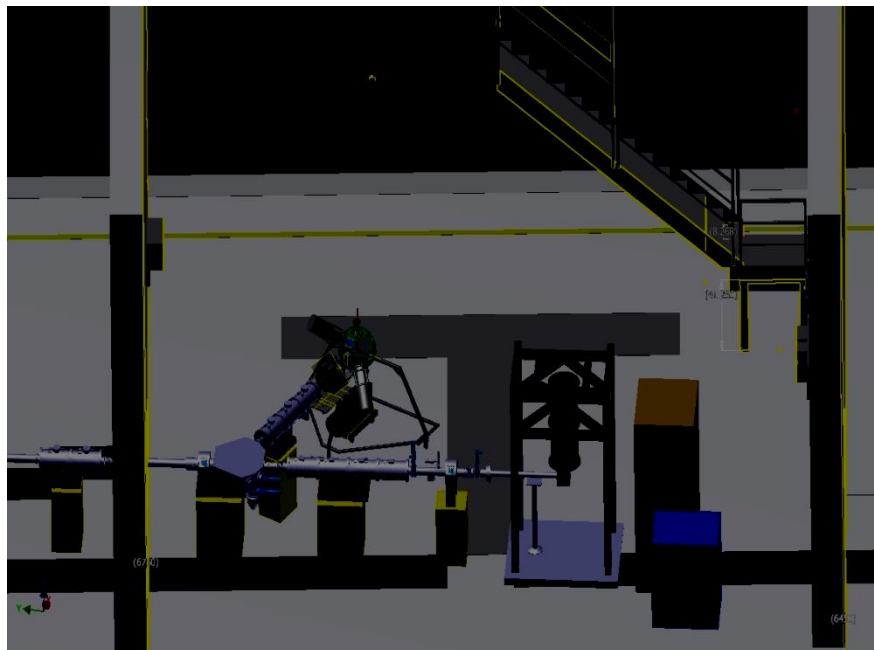


Figure 6. Model of ISOLDE

Below is the model of the experimental area which shows the Decay Station setup (in green) next to the beam line.



---

Figure 7: experimental area side view, beam line to detector setup

Before the experiment, the drawing could be used to do a stress test on the equipment to fine tune the detectors. The the updated CAD drawing would be useful for this experiment and future experiments in Isolde that wish to use the beam line, so my work may be useful to Isolde for several years down the line.

# Constraining track reconstruction of GTK with the target and beam-line elements in backward propagation

SMITH, Herbert Postyn      Mentor: PERRIN-TERRIN, Mathieu  
Program Mentor: CECCUCCI, Augusto

30 June 2014

---

## 1      EXPERIMENT OVERVIEW

---

The NA62 experiment at CERN is an ultra-rare charged kaon decay experiment studying the decay of  $K^+ \rightarrow \pi^+ \bar{s} \nu_s$ . The experiment will begin collecting data in the fall of 2014 aiming to observe approximately eighty events over a data taking period of two years. This decay is mediated by the flavor-changing weak decay of a top quark into a bottom quark and plans to extract a ten percent measurement on the  $|V_{td}|$  CKM matrix<sup>2</sup> parameter. This will either confirm theoretical predictions from the Standard Model in flavor-changing weak decays or could be a gateway into New Physics if the data refutes the theoretically proposed parameter.

---

## 2      PROJECT OVERVIEW

---

The Gigatracker (GTK) is comprised of three silicon micro-pixel stations that, in combination, measure the time, momentum, and angle of particles before they enter the decay region. The  $300 \mu m \times 300 \mu m$  pixel size of the detector constrains the ability of the GTK to reconstruct the particle tracks with complete accuracy. Given that the particles originated from the target and traversed all of the beam-line elements, the reconstructed tracks can be propagated back from GTK with the expectation that they will again pass through all of the beam-line elements along their path ending at the target. By comparing reconstructed Monte Carlo tracks with true Monte Carlo tracks, we can measure the discrepancy of the GTK reconstructions with the true tracks. Furthermore, simultaneous hits on different pixels at each station of the GTK allow for multiple possible reconstruction tracks. Constraining the reconstructed tracks to have traversed the beam-line elements and originated from the target will also eliminate these falsely reconstructed tracks.

1

## 3      RESEARCH FINDINGS

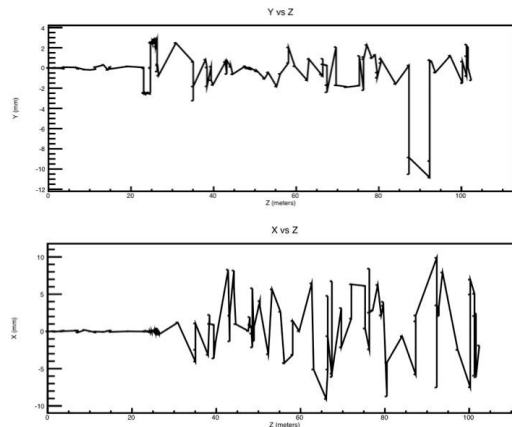
---

<sup>2</sup> Cabibbo-Kobayashi-Maskawa matrix

## 3.1 TRACING THE BEAM LINE

The NA62 experiment uses TURTLE<sup>3</sup> to simulate the transport of charged particles. In this modified version of TURTLE, the program takes datacards as an input file with initial conditions of a particle's positions in x and y, momentum in x, y, and z, and angular divergence in x and y and runs this particle through the elements of the beam line where each line of the datacard describes an element or a part of an element (drift space, quadruple, collimator, dimensions of a bending magnet, etc.). Previous to this study, TURTLE and the datacards had only propagated the particles forwards through the experiment. Therefore, to gain an understanding of how the tracks are propagated and ensure that TURTLE with the datacards was simulating the particle tracks correctly, I wrote a script to run a particle forwards and backwards through the beam-line elements. If the particles were being simulated correctly, the plots both forwards and backwards would be identical.

Initially (Figure 1), TURTLE contained conditions to simulate random material interaction as particles pass through the elements. I removed those interactions because I wanted to first study the ideal case of no interaction in the propagation forward. There will also never be interaction in the backward propagation because the particle is not actually passing through the elements again. Instead, I am tracing the paths of the particles for the Monte Carlo GTK reconstructions



and Monte Carlo truth simulations backwards.

Figure 2a shows the forward and back-

ward tracing for a particle in Y vs. Z with

no initial displacement, momentum, and angular divergence in x and y for a particle with initial momentum of 75 GeV in z. Upon close examination, there is a difference between the forward and backward propagation because TURTLE limits the beam parameter inputs to 8 decimal places. These differences at  $10^{-9}$  are then propagated over all of the beam-line elements.

Figure 2b shows the forward and backward tracing for a particle with small initial deviations from the nominal track in position and angular divergence.

Figure 1: TURTLE with material interaction. Vertical axis in millimeters and horizontal axis in meters

<sup>3</sup> Trace Unlimited Rays Through Lumped Elements

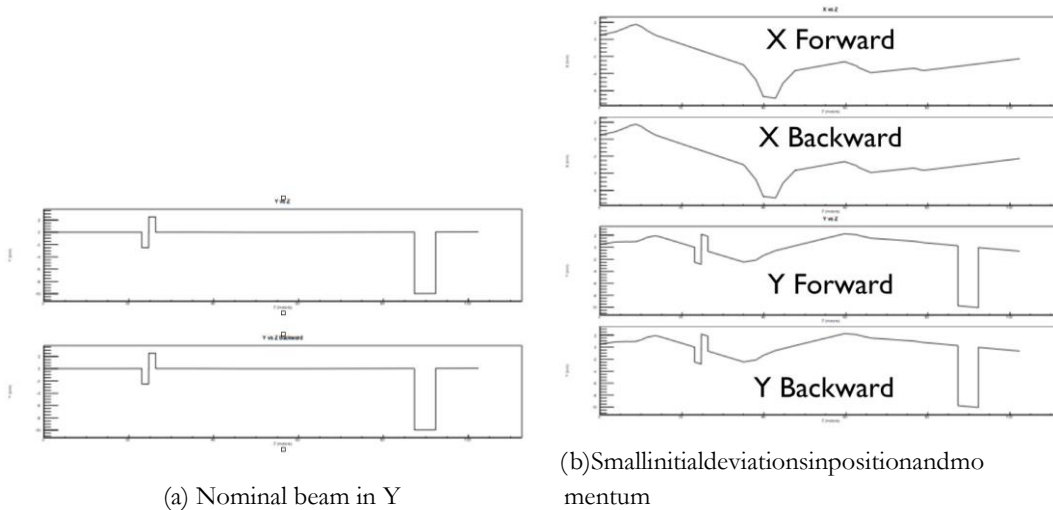


Figure 2: Forward and backward propagation of tracks with the vertical axis in millimeters and the horizontal axis in meters

Overall, the figures confirm that TURTLE with the appropriate data cards correctly traces the track of the particle both forwards and backwards. The inverted datacard for tracing particles going backwards reflect the opposite shift of the beam at the GTK stations and the acromats and to move quadrupole conditions in front of the appropriate quadrupoles. This is in contrast to the originally inverted datacards that essentially reversed the order of all of the elements.

### 3.2 FINDING MOST CONSTRAINING BEAM-LINE ELEMENTS

For this section of the analysis, Monte Carlo truth tracks and Monte Carlo reconstructed tracks were propagated backwards from GTK1.<sup>4</sup> If GTK reconstructed the tracks perfectly, there would be no discrepancy between the size of the beam spot or the number of tracks stopped in elements when propagated backwards. Since this is not the case, the elements in the beam line where the reconstruction differs the most from the true tracks can be used to create a least <sup>2</sup> fit to improve the resolution of the GTK.

Approximately 20,000 Monte Carlo reconstructed and Monte Carlo truth tracks were propagated backwards and examined at each element along the beam line. The root mean square in x and y was calculated at each position. If a particle was stopped in an element, it was propagated no further backwards.

---

<sup>4</sup> Initially, we propagated the truth tracks back from GTK1 and the reconstruction tracks back from GTK3, but we hypothesize that there is a discrepancy between how GEANT4 simulates the tracks going forward to GTK3 that we then used for the input of the reconstructed tracks and how TURTLE simulates them going back.

3.2.1 NO INTERACTION

No interaction refers a simulated absence of interaction from the CEDAR<sup>5</sup>. This allows for a best case scenario study of the tracks.

The first step was implementing a script that examined the RMS of the beam spot for both the reconstructed and truth tracks at each element and counted the number of tracks stopped at each element. Figure 4 plots the RMS of the beam spot in X and Y (mm) versus Z position (m). This shape is expected because: when a quadrupole focuses on one axis it defocuses the other axis; the focus points are at the target, TAXs, and collimators; the beam runs parallel through the CEDAR.

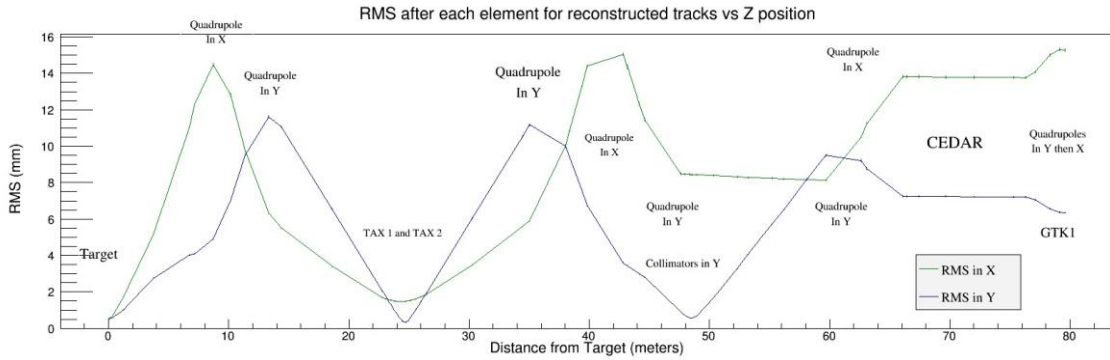


Figure 3: RMS (mm) in X and Y vs Z position(m)

If the reconstructed and truth tracks had the same accuracy, a ratio of the RMSs would be one, but as Figure 5 shows, there are peaks where the ratio of reconstructed RMS over truth RMS differs the most. The two main peaks are at the target and TAXs. This demonstrates the inefficiency of the GTK, but in terms of implementing a fit, the more significant the difference between the two allows for a stronger fit.

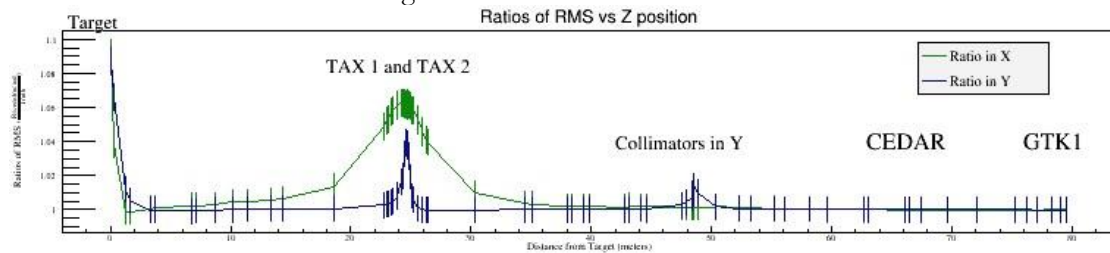


Figure 4: RMS ratio ( $\frac{Reconstructed}{Truth}$ )

For visual reference, Figures 6 and 7 show the shape of the beam spot at the TAXs and the target. The difference between the RMSs is noticeable by visually inspection.

<sup>5</sup> Cherenkov Differential counter with Acromatic Ring Focus - This proceeds the GTK in the beam line and identifies particles using Cherenkov radiation



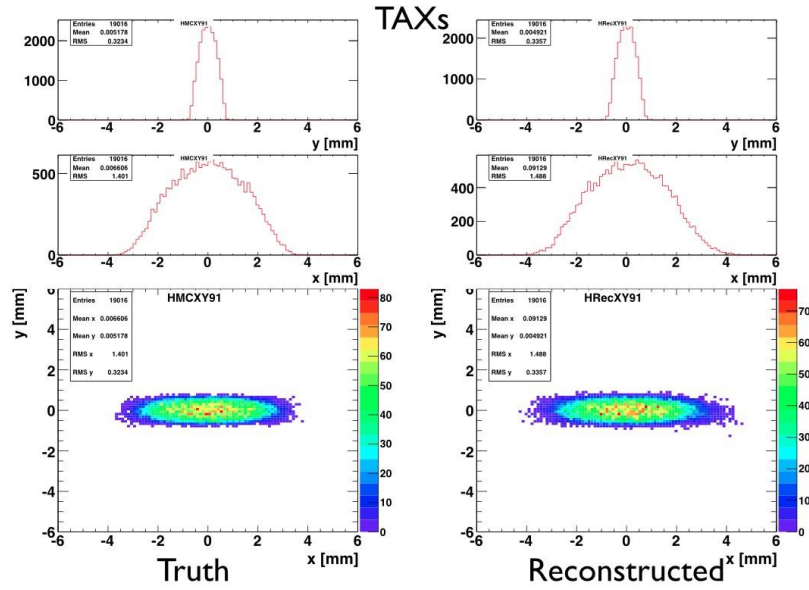


Figure 5: RMS histograms at the TAXs (Profile in Y, Profile in X, Profile in X and Y)

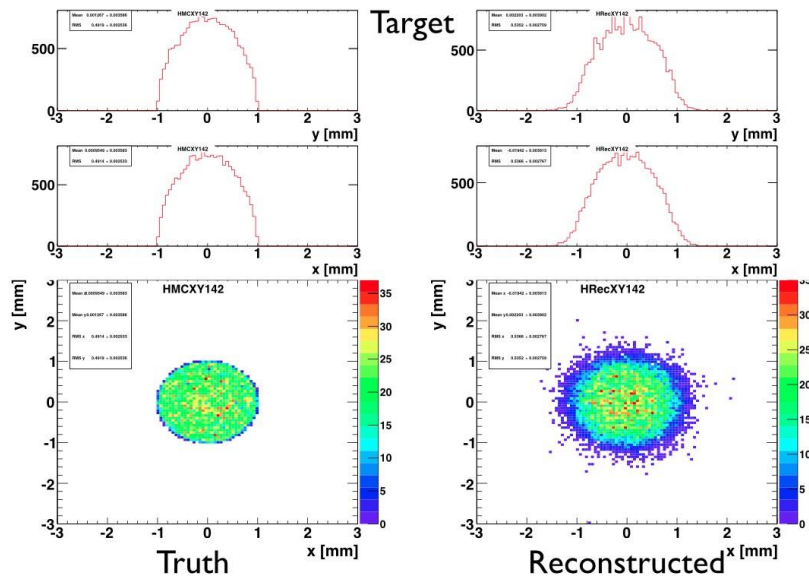


Figure 6: RMS histograms at the target (Profile in Y, Profile in X, Profile in X and Y)

3.2.2 *Enlarged elements*

As we studied the ratio plot, we noticed that the ratio continues to increase until the focal point of the quadrupoles. Given that there are multiple collimators before and after each focal point, the furthest outlying tracks were being stopped and eliminated from the analysis based on our previous conditions. To regain this information, all of the elements were opened to a half-width size of two meters.

In comparing the standard and enlarged ratios, the GTK inefficiencies become more apparent at both the TAXs and the target. Figure 8 shows how the ratios of reconstructed over truth compare in both X and Y for the standard and opened elements.

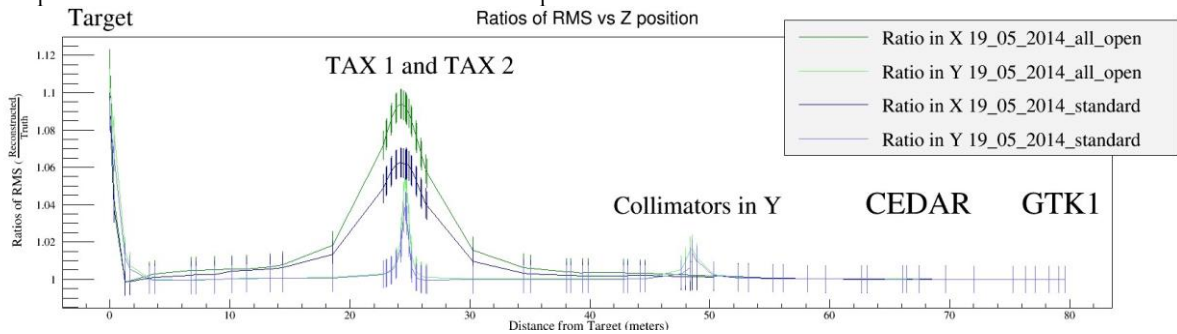


Figure 7: RMS ratio  $\left(\frac{Reconstructed}{Truth}\right)$  for standard and opened beam-line elements

3.3 N<sub>2</sub> VS H<sub>2</sub> IN CEDAR

To study the difference between N<sub>2</sub> and H<sub>2</sub> in the CEDAR, we implemented a smearing of 36 micro-radians and 11 micro-radians, respectively. Mathieu had already studied the effects of a 22 micro-radian smearing for N<sub>2</sub> in comparison to H<sub>2</sub> at the target. This study expanded on those finding at all of the elements with a smearing more appropriate for N<sub>2</sub>.

Figure 9 shows the comparison of ratios between N<sub>2</sub> and H<sub>2</sub> where ratio of the tracks is larger for H<sub>2</sub>. Therefore, although the H<sub>2</sub> interacts less with the particles than the N<sub>2</sub>, the difference between the reconstructed and truth tracks is larger.

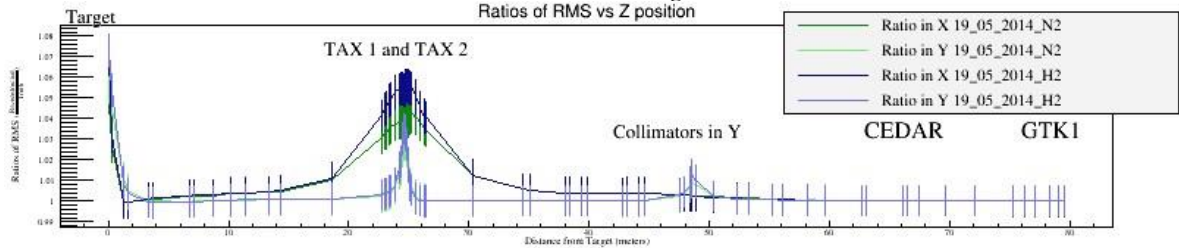


Figure 8: RMS ratio  $\left(\frac{Reconstructed}{Truth}\right)$  for N<sub>2</sub> vs H<sub>2</sub> in the CEDAR

The results in Table 1 are expected. More reconstructed tracks are stopped than true tracks. With no interaction, very few tracks are stopped (and for the truth tracks essentially none). N<sub>2</sub> stops more tracks than H<sub>2</sub>.

	Truth	Reconstructed		
No Interaction	0.06 ± 0.02	3.3 ± 0.1		
H <sub>2</sub> (11 micro-radians)	4.9 ± 0.2	6.2 ± 0.2		
N <sub>2</sub> (33 micro-radians)	10.9 ± 0.2	12.6 ± 0.3		
N <sub>2</sub> (22 micro-radians)	6.7 ± 0.2	9.5 ± 0.2	±	±

Table 1: Percent of tracks stopped through backward propagation to the target

### 3.4 PILE-UP STUDY N<sub>2</sub> VS H<sub>2</sub> IN CEDAR

In examining the most constraining collimators and the differences between H<sub>2</sub> and N<sub>2</sub>, we also looked at the ability to eliminate fake tracks based on the medium in the CEDER. The GTK reconstruction creates fake tracks from simultaneous hits on different pixels. The reconstruction traces tracks for all given simultaneous hits on each GTK station.

Thus, a track with 3 simultaneous hits on GTK1, 2 simultaneous hits on GTK2 and GTK3 has 24 (3!2!2!) possible reconstructed tracks. Only one of these is the actual track and therefore, we would to remove these fake tracks.

Analyzing at the target, table 2 shows that although N<sub>2</sub> stops more real tracks than H<sub>2</sub>, there is little difference between the number of fake tracks stopped by N<sub>2</sub> and H<sub>2</sub>.

		N <sub>2</sub> (36) <sup>6</sup>	H <sub>2</sub> (11)		
TAXs <sup>7</sup>	Real	9.8 ± 0.2	3.8 ± 0.2		
	Fake	89.8 ± 0.4	89.7 ± 0.4		
Target	Real	12.6 ± 0.2	6.2 ± 0.2	±	±
	Fake	91.7 ± 0.4	91.7 ± 0.4		

Table 2: Percent of N<sub>2</sub>

stopped

vs H<sub>2</sub> pile-up tracks

<sup>6</sup> The percentages for the real tracks stopped for N<sub>2</sub> did not come from the script that ran the pile-up study. The percentages from that script were considerably lower.

<sup>7</sup> The values after card 90 from the datacards starting at GTK1 were used for the TAXs' values.

### 3.5 IMPLEMENTING A FIT

Given the time constraints for my research, we decided to begin the process of implementing a least <sup>2</sup> fit using the three GTK stations and adding the target because the previous analysis showed that the target is the most constraining point in track recreation.

My first goal was to find a linear, analytic equation for particles traveling through GTK, which for the considerations of the analytic equation is comprised of drift spaces and bending magnets. Using the diagrams attached at the end, I worked out the geometry of the displacements to find the total displacement in the x and y direction given a incident particle with an initial angle,  $\alpha$ .

Variable definitions:

$\alpha$  incident angle of the particle

$l$  length of bending magnet

$R$  radius of particle's curve in magnet, dependent on  $p_{Total}$  and B-field

$\Delta\theta$  change in angle due to magnet ( $\pm\alpha$ )

$\Delta y_{Mag}, \Delta y_{Drift}$  displacement in y (or x) due to magnet or drift

$\Delta y_{ij}$  displacement in y (or x) between GTK $i$ /GTK $j$

General

equations:

$$\alpha = \arcsin\left(\frac{l + R \sin \theta}{R}\right) - \theta$$

$$\phi = \arcsin\left(\frac{l + R \sin \theta}{R}\right) - \theta$$

$$\delta_{Mag} = \begin{cases} R \cos \theta + \sqrt{R^2 - (l - R \sin \theta)^2} & \text{Bending magnets 1 and 2} \\ R \cos \theta - \sqrt{R^2 - (l + R \sin \theta)^2} & \text{Bending magnets 3 and 4} \\ \text{otherwise} & \end{cases}$$

<sup>8</sup> The drawings associated with the following equations are attached to the end of the document.

$$\delta_{Drift} = \begin{cases} \Delta \tan \theta & \text{(in x)} \\ \Delta \tan(\alpha + \theta) & \text{(in y)} \\ \Delta & \text{(in z)} \end{cases} \quad \text{between bending magnets 1 and 2 (in y), TRIM}$$

For y direction:  $\tan(\sqrt{\quad})$  between bending magnets 3 and 4 (in y)

$$\delta_{12} = \theta(\Delta + \Delta_s) \frac{l}{R}(l + \Delta_s)$$

$$\delta_{23} = \theta(\Delta - \Delta_s) \frac{l}{R}(l - \Delta_s)$$

$$\delta_{13} = \delta_{12} + \delta_{23}$$

$$\delta_{13} = \theta(\Delta_{12} + \Delta_{23}) \frac{2l^2}{R}$$

4 FURTHER WORK

For x direction:

$2l = \Delta_s \tan \sqrt{\quad}$  Note:  $\Delta_s, \Delta_s \sqrt{\quad}, etc.$  are different from y direction values

$$\delta_{23} = \theta(\Delta + \Delta_s) \frac{l}{R} \left( \Delta_s - \frac{l}{2} \right)$$

$$\delta_{13} = \theta(\Delta_{12} + \Delta_{23} + \Delta_s) \frac{l}{R} \left( \Delta_s - \frac{l}{2} \right) = \theta \Delta_{Total} \frac{l}{R} \left( \Delta_s - \frac{l}{2} \right)$$

This produced similar results to the reconstruction code currently used. Due to time limitations, this is where I finished working.

## 4 FURTHER WORK

### 4.1 FURTHER INVESTIGATION OF TURTLE

Considering the tracing of the particle tracks forwards and backwards was not exactly the same, a more rigorous study and deeper understanding of how the eight floating point limit on TURTLE beam inputs affects the results of track propagation and stopping tracks would allow for a more accurate analysis.

### 4.2 N<sub>2</sub> PILE-UP PERCENTAGES

As footnote 7 indicates, the N<sub>2</sub> pile-up percentages for real tracks was not taken from the same script that ran the pile-up study. Since we know the real percentages from the non pile-up studies we used those figures for comparison. This error in the script should be resolved so that the percentage of real and fake tracks stopped can be analyzed from the same script.

### 4.3 FINISH FIT

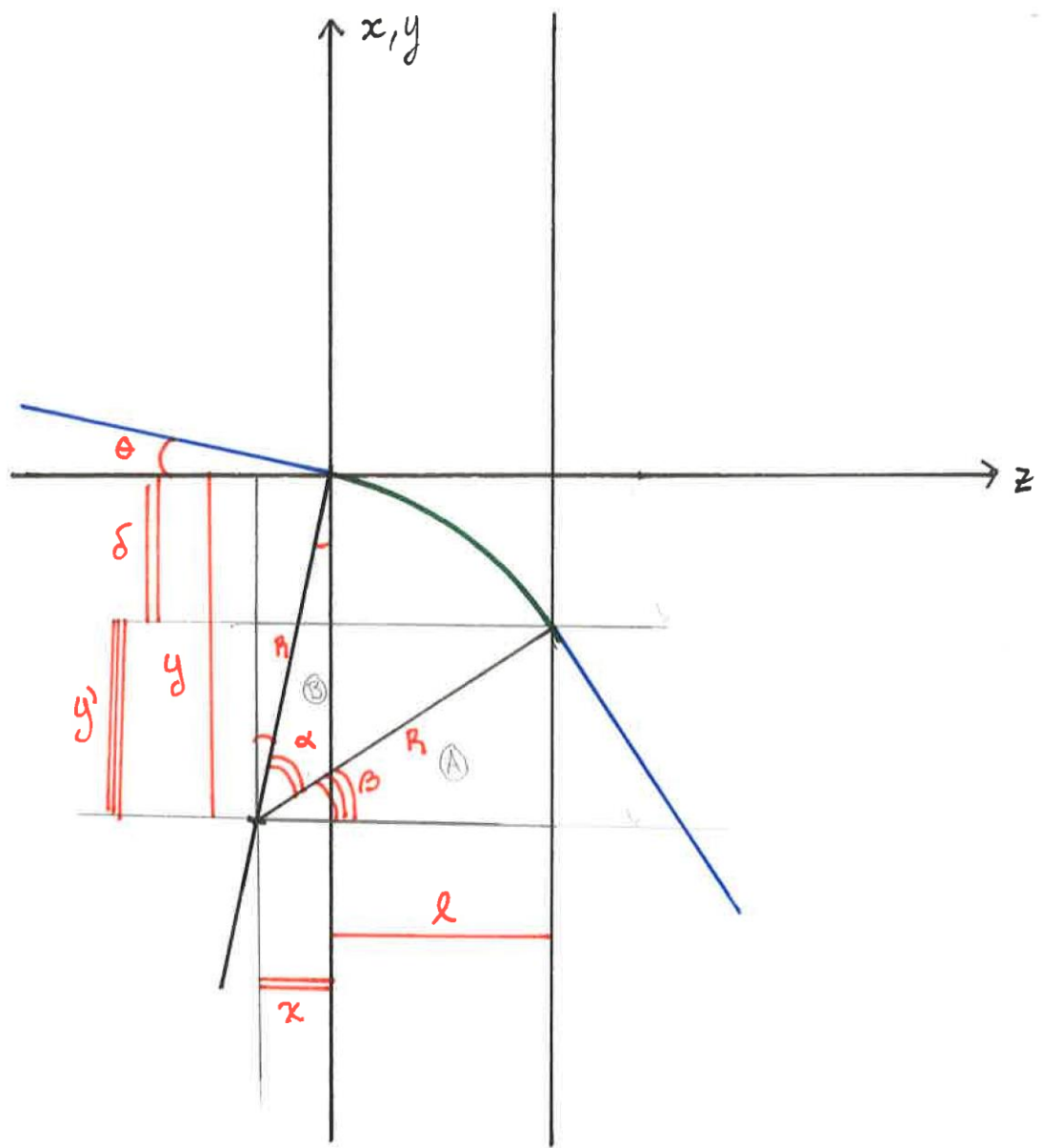
My research period was not long enough for me to finish a least <sup>2</sup> fit from GTK3 back to the target. Using TRANSPORT matrices from Lau and the analytic equations through the GTK, one

could now implement the least <sup>2</sup> fit for tracks from  $GTK3 > Target$ . Then, a full Kalman filter could be implemented to have be able to analyze the data on a track by track basis.

(A)

13/6/2014

$$\theta = \frac{P_A}{P_z} < 0$$



Look at triangle (A),  
By the Pythagorean theorem,

$$R^2 = (l+x)^2 + (y-\delta)^2$$

Solve for  $\delta$ ,

$$y-\delta = \sqrt{R^2 - (l+x)^2}$$

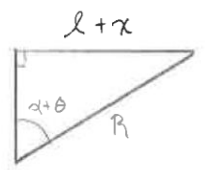
$$\delta = y - \sqrt{R^2 - (l+x)^2}$$

$$y = R \cos(\theta), \quad x = R \sin(\theta)$$

$$\delta = -R \cos(\theta) + \sqrt{R^2 - (l - R \sin(\theta))^2}$$

Looking at triangle (B),

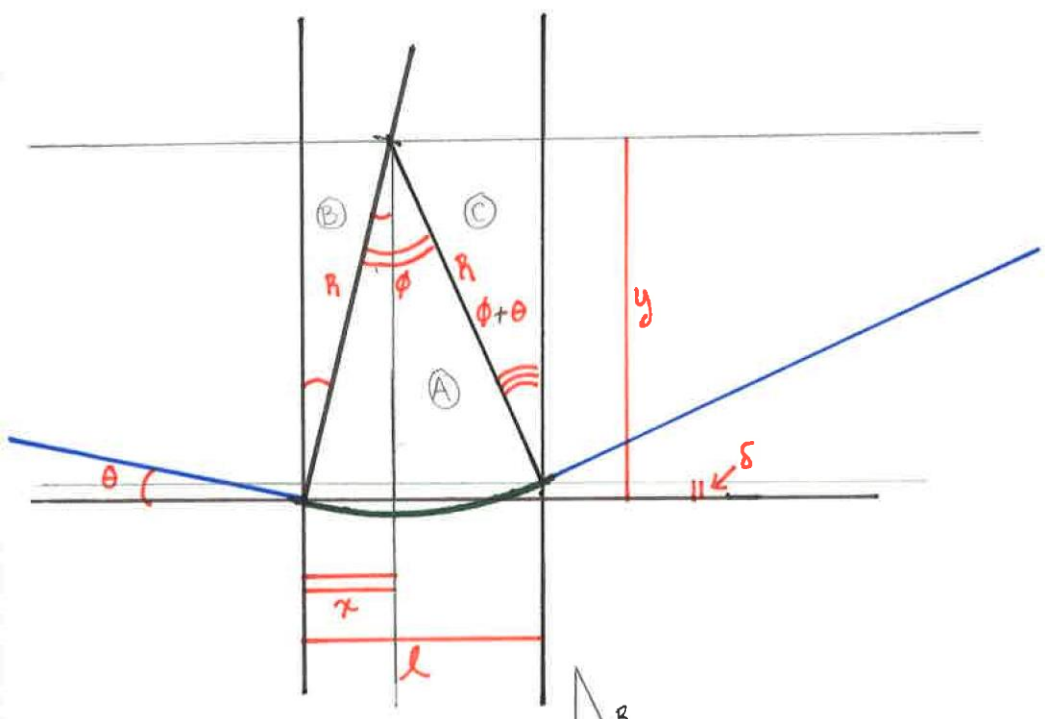
$$\sin(\alpha + \theta) = -\frac{l+x}{R}$$



$$\alpha = \text{Arccsin}\left(-\frac{l+x}{R}\right) - \theta$$

$$\alpha = \text{Arccsin}\left(-\frac{l - R \sin(\theta)}{R}\right) - \theta$$

$1/|1-\epsilon|$



$$\theta < 0$$

$$\phi > 0$$

$$|\phi| > |\theta|$$

Looking at triangle (A)  $y-\delta$

By the Pythagorean theorem,

$$R^2 = (l-x)^2 + (y-\delta)^2$$

so,

$$\delta = y - \sqrt{R^2 - (l-x)^2}$$

$$x = R \sin(\theta), \quad y = R \cos(\theta)$$

$$\delta = R \cos(\theta) - \sqrt{R^2 - (l + R \sin(\theta))^2}$$

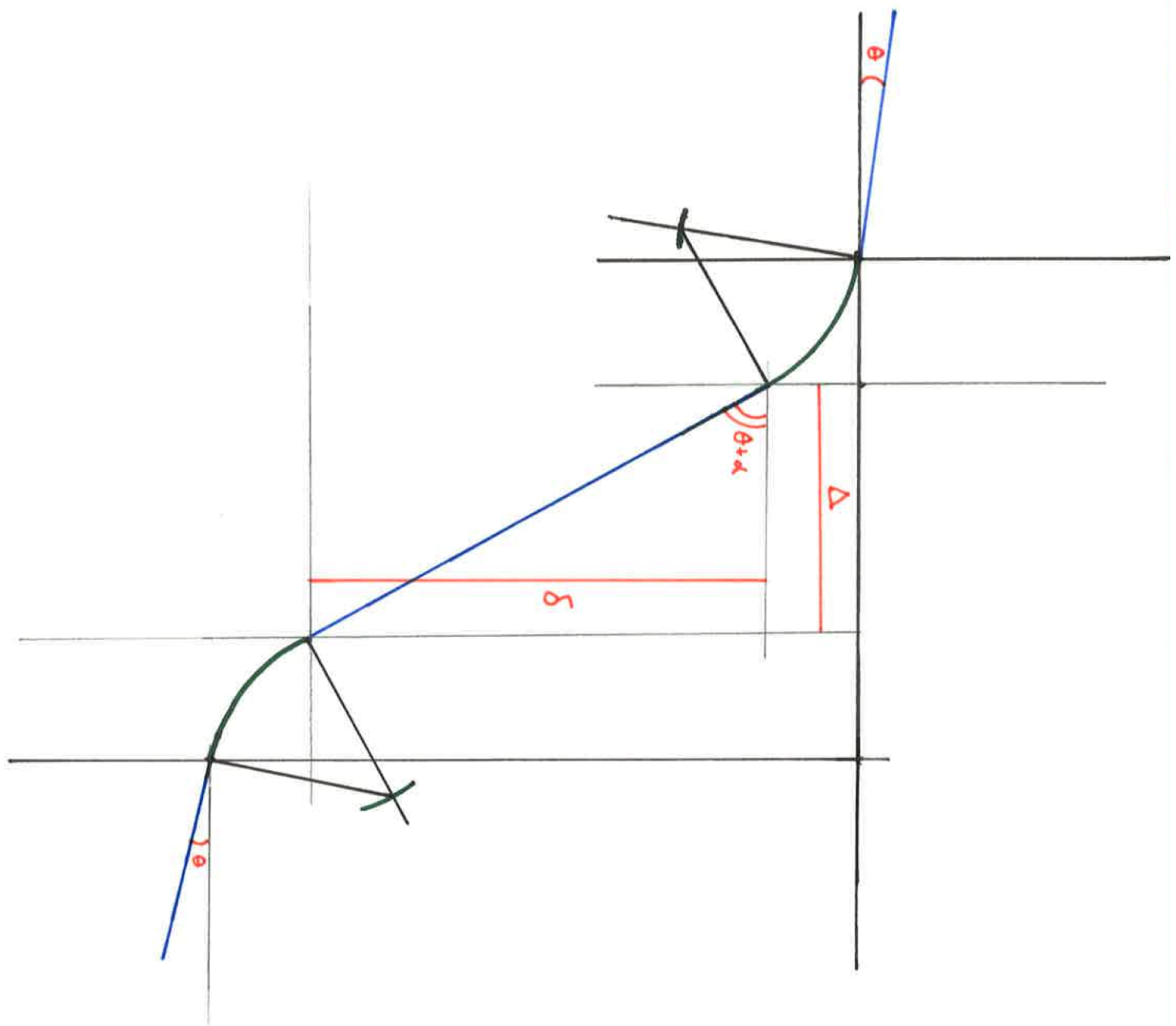
Looking at triangles (B) + (C),

$$l = R \sin(\theta) + R \sin(\phi + \theta)$$

so,

$$\phi = \text{Arcsin} \left[ \frac{l + R \sin(\theta)}{R} \right] - \theta$$





$$\tan(\theta + \alpha) = \frac{\delta}{\Delta}$$

$$\delta = \Delta \tan(\theta + \alpha)$$

$$\delta = \frac{1}{\sigma^2}$$

$$\delta_1 = \Delta_1 \tan(\theta)$$

$$\delta_2 = -R \cos(\theta) + \sqrt{R^2 - (L - R \sin(\theta))^2}$$

$$\alpha = \text{Arccos} \left[ \frac{L - R \sin(\theta)}{R} \right] - \theta$$

$$\delta_3 = \Delta_3 \tan(\alpha + \theta)$$

$$\delta_4 = \delta_2$$

$$\sum_{i=5}^7 \delta_i = \Delta_i \tan(\theta)$$

$$\delta_8 = \Delta_8 \tan(\theta)$$

$$\delta_9 = R \cos(\theta) - \sqrt{R^2 - (L + R \sin(\theta))^2}$$

$$\phi = \text{Arccos} \left[ \frac{L + R \sin(\theta)}{R} \right] - \theta$$

$$\delta_{10} = \Delta_{10} \tan(\phi - \theta)$$

$$\delta_{11} = \delta_9$$

$$\delta_{12} = \Delta_{12} \tan(\theta)$$

$$\delta_{13,14} = \Delta_{13,14} \tan(\theta)$$

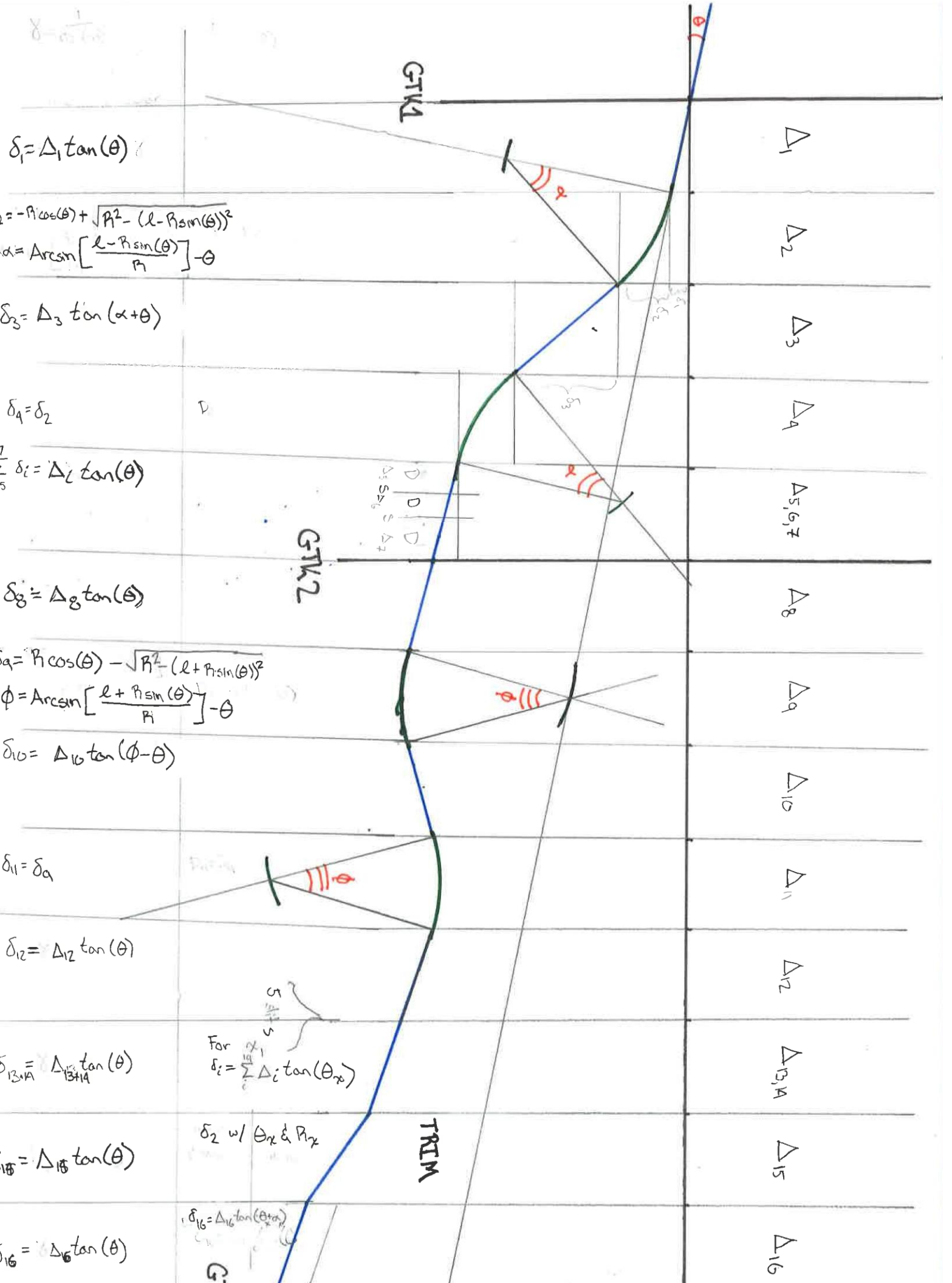
For  $\delta_i = \sum \Delta_i \tan(\theta_x)$

$\delta_2$  w/  $\theta_x$  &  $R_x$

TRIM

$$\delta_{16} = \Delta_{16} \tan(\theta)$$

$$\delta_{16} = \Delta_{16} \tan(\theta_x)$$



$\Delta_1$

$\Delta_2$

$\Delta_3$

$\Delta_4$

$\Delta_5, 6, 7$

$\Delta_8$

$\Delta_9$

$\Delta_{10}$

$\Delta_{11}$

$\Delta_{12}$

$\Delta_{13,14}$

$\Delta_{15}$

$\Delta_{16}$

GTWL

GWL

D

$\Delta_5 \Delta_6 \Delta_7$

$R_x$

$\theta_x$

For

$\delta_2$

G

GTK 1  $\rightarrow$  GTK 2 (Trying to emulate Mathieu)

$$\begin{aligned} \delta_{12} &= \Delta \tan(\theta) + \Delta_s \tan(\theta + \alpha) + 2 \delta_{mag} \\ &= \Delta \theta + \Delta_s (\theta + \alpha) + 2 \left[ -R \cos(\theta) + \sqrt{R^2 - (l - R \sin(\theta))^2} \right] \\ &= \theta(\Delta + \Delta_s) + \alpha \Delta_s + 2R \left[ -1 + \sqrt{1 - \left(\frac{l}{R} - \theta\right)^2} \right] \end{aligned}$$

$$= \theta(\Delta + \Delta_s) + \alpha \Delta_s + 2R \left[ -1 + \sqrt{1 - \frac{l^2}{R^2} + 2\frac{l\theta}{R} - \theta^2} \right]$$

$$\frac{l^2}{R^2} \sim O(10^{-4})$$

$$= \theta(\Delta + \Delta_s) + \alpha \Delta_s + 2R \left[ -1 + \sqrt{1 - \left(\frac{l}{R}\right)^2} \right]$$

$$\frac{2l\theta}{R} \sim O(10^{-6})$$

$$= \theta(\Delta + \Delta_s) + \alpha \Delta_s + 2R \left[ -1 + 1 - \frac{1}{2} \left(\frac{l}{R}\right)^2 \right]$$

$$\theta^2 \sim O(10^{-8})$$

$$= \theta(\Delta + \Delta_s) + \alpha \Delta_s + \cancel{\dots} - \frac{l^2}{R}$$

$$= \theta(\Delta + \Delta_s) - \frac{l}{R} \Delta_s + \cancel{\dots} - \frac{l^2}{R}$$

$$\delta_{12} = \theta(\Delta + \Delta_s) - \frac{l}{R} (\Delta_s + l)$$

so, in your notation:  $\delta_{12} = y'(d + d_s) - \frac{l}{R}(d_s + l)$   $\left[ \begin{array}{l} \alpha = \text{Arcsin} \left( -\frac{l - R \sin \theta}{R} \right) - \theta \\ \alpha \approx \frac{-l + R \theta}{R} - \theta \\ \alpha \approx -\frac{l}{R} \end{array} \right.$

or  $R[\delta_{12} - \theta(\Delta + \Delta_s)] = -l(\Delta_s + l)$

$$R = \frac{-l(\Delta_s + l)}{\delta_{12} - \theta(\Delta + \Delta_s)}$$

I think you made a mistake in here to end up getting the 3y'ds term.

GTK2 → GTK3

$$\delta_{23} = \Delta \tan(\theta) + \Delta_s \tan(\phi - \theta) + 2 \cdot \delta_{\text{Mag}}$$

Same as  $\delta_{12}$  derivation except for  $\phi$  (should check  $\delta_{\text{Mag}}$ )

~~For  $\delta_{12}$  derivation,~~

$$\delta_{\text{Mag}} = R \cos(\theta) - \sqrt{R^2 - (l + R \sin \theta)^2}$$

$$\phi = \text{Arcsin} \left[ \frac{l + R \sin(\theta)}{R} \right] - \theta$$

$$\phi \approx \frac{l}{R} + \theta - \theta$$

$$\delta_{\text{Mag}} \approx R - \sqrt{R^2 - (l + R \theta)^2}$$

$$\phi \approx \frac{l}{R}$$

$$\approx R \left[ 1 - \sqrt{1 - \left( \frac{l}{R} + \theta \right)^2} \right]$$

$$\approx R \left[ 1 - \sqrt{1 - \frac{l^2}{R^2} - \frac{2l\theta}{R} - \theta^2} \right]$$

$$\approx R \left[ 1 - \sqrt{1 - \left( \frac{l}{R} \right)^2} \right] \xrightarrow{\text{small}} \text{some as other}$$

$$\approx -\frac{l^2}{R}$$

$$\delta_{23} \approx \Delta \theta + \Delta_s \phi - \Delta_s \theta - \frac{l^2}{R}$$

$$\delta_{23} \approx \theta (\Delta - \Delta_s) + \frac{l}{R} \Delta_s - \frac{l^2}{R}$$

$$\delta_{23} \approx \theta (\Delta - \Delta_s) + \frac{l}{R} (\Delta_s - l)$$

in your notation,

$$\delta_{23} \approx y' (d - d_s) - \frac{l}{R} (l - d_s)$$

Solve for  $R$ ,

~~$$R [\delta_{23} + \frac{l}{R} (l - d_s)] = y' (d - d_s)$$~~

~~$$R = \frac{y' (d - d_s)}{\delta_{23} + \frac{l}{R} (l - d_s)}$$~~

$$R [\delta_{23} - y' (d - d_s)] = -l (l - d_s)$$

$$R = \frac{-l (l - d_s)}{\delta_{23} - y' (d - d_s)}$$

If I add  $GTK1 \rightarrow GTK2 + GTK2 \rightarrow GTK3$

$$\delta_{12} = \theta(\Delta + \Delta_s) - \frac{l}{R}(\Delta_s + l) \quad \delta_{23} = \theta(\Delta - \Delta_s) + \frac{l}{R}(\Delta_s - l)$$

$\Delta_s$  is the same in both (1.1 meters)

$l$  is the same (2.5 meters)

$\theta$  same

$$\Delta \text{ in } \delta_{12} \Rightarrow \Delta_{12} = 13.2 \text{ m} - 5 \text{ m} = 8.2 \text{ m}$$

$$\Delta \text{ in } \delta_{23} \Rightarrow \Delta_{23} = 9.7 \text{ m} - 5 \text{ m} = 4.7 \text{ m}$$

( $R$  should be the same in both)

$\hookrightarrow$  I assume it is

$$\delta_{13} = \delta_{12} + \delta_{23}$$

$$\delta_{13} \approx \theta(\Delta_{12} + \Delta_s) - \frac{l}{R}(\Delta_s + l) + \theta(\Delta_{23} - \Delta_s) + \frac{l}{R}(\Delta_s - l)$$

$$\delta_{13} \approx \theta(\Delta_{12} + \Delta_{23}) - \frac{2l^2}{R}$$

Solve for  $R$

$$\frac{2l^2}{R} = \theta(\Delta_{12} + \Delta_{23}) - \delta_{13}$$

$$R = \frac{2l^2}{\theta(\Delta_{12} + \Delta_{23}) - \delta_{13}}$$

## For X-axis

$$\delta_{12} = \Delta_y \tan(\theta) \quad \text{keep in mind} \\ \text{-values for } \Delta \text{ \& } \theta \text{ different than for y-axis}$$

$$\delta_{12} = \Delta \theta$$

$$\delta_{23} = \Delta \tan(\theta) + \delta_{Mag} + \Delta_s \tan(\theta + \theta) \quad \text{(Same as GTK1} \rightarrow \text{GTK2} \\ \text{except for factor of 2} \\ \text{before } \delta_{Mag}$$

$$\delta_{23} \approx \theta (\Delta + \Delta_s) - \frac{l}{R} \Delta_s - \frac{l^2}{2R}$$

$$\delta_{23} \approx \theta (\Delta + \Delta_s) - \frac{l}{R} (\Delta_s - \frac{l}{2})$$

$$\text{so, } \frac{l}{R} (\Delta_s - \frac{l}{2}) = \theta (\Delta + \Delta_s) - \delta_{23}$$

$$R = \frac{l (\Delta_s - \frac{l}{2})}{\theta (\Delta + \Delta_s) - \delta_{23}}$$

$$\delta_{13} = \delta_{12} + \delta_{23}$$

$$\delta_{13} = \Delta \theta + \theta (\Delta_{23} + \Delta_s) - \frac{l}{R} (\Delta_s - \frac{l}{2})$$

$$\delta_{13} = \theta (2\Delta + \Delta_s) - \frac{l}{R} (\Delta_s - \frac{l}{2})$$

$$\frac{\delta_{12}}{\theta} = \frac{\delta_{23}}{\theta}$$

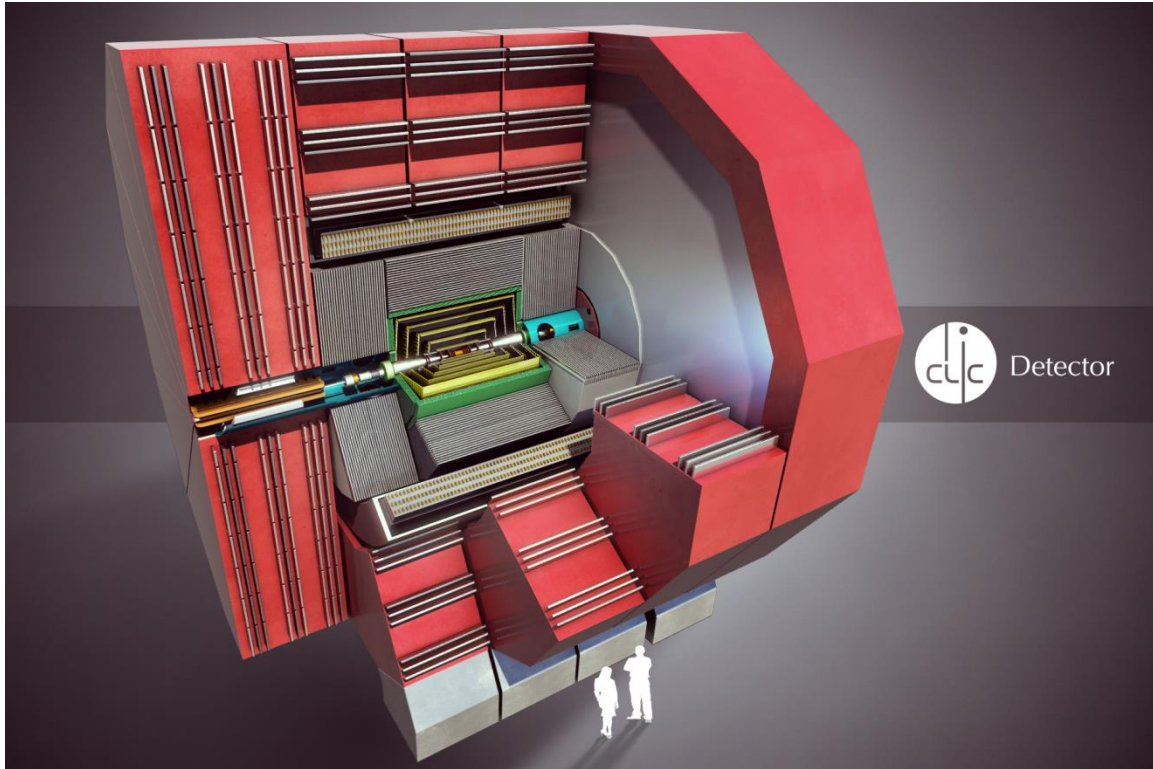
$$\theta = \theta$$

$$\Delta \neq \Delta \rightarrow \Delta_{12} = 22.0 \text{ meters}$$

$$\Delta \rightarrow \Delta_{23} = 0.4 \text{ meters}$$

$$\delta_{13} = \theta (\Delta_{12} + \Delta_{23} + \Delta_s) - \frac{l}{R} (\Delta_s - \frac{l}{2})$$





The CLIC-Vertex Detector  
-Kyle Spindelman

The Compact Linear Collider (CLIC) is a proposal to be one of CERN's next generation particle accelerators. The accelerator as opposed to the current Large Hadron Collider would collide electrons and positrons at high energies of about 3TeV. In order to avoid synchrotron radiation it would have to be linear. There are a few advantages with these differences.

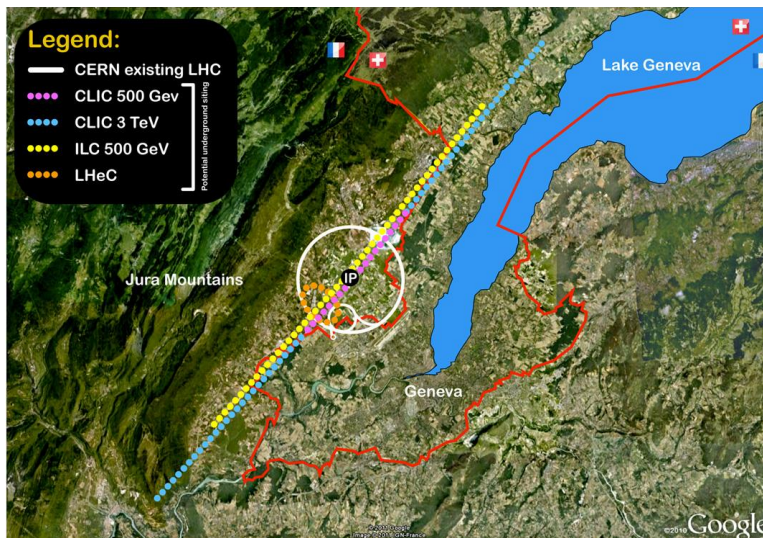


Figure 1: Proposed location of the CLIC Accelerator

The first advantage is that electrons are fundamental particles while the protons of the LHC are compound particles. They are made up of smaller fundamental particles such as quarks and gluons.

This means that the proton initial conditions are not well defined. On the other hand electron and positron initial conditions are very well defined and measurements become more precise. The other main advantage for lepton collisions is lower radiation. Due to the lower radiation air cooling is being researched for the inner detector.

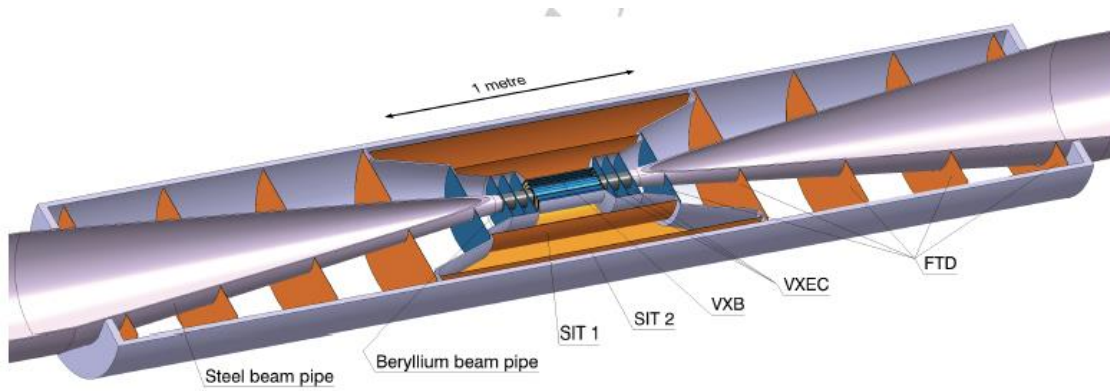


Figure 2: The CLIC Vertex Detector

The name of the innermost detector is the CLIC-Vertex detector. The average velocity for the proposed air cooling would be about 5.2m/s. The main requirement for the CLIC-Vertex detector is a low material budget. We would like a 0.2% radiation length per layer in the main barrel. This means low mass supports for the detectors. The air cooling strategy also minimizes on material. The conventional use of liquid cooling not only increases the material budget through the liquid itself but also the pipes carrying it. This is why air cooling seems optimal.

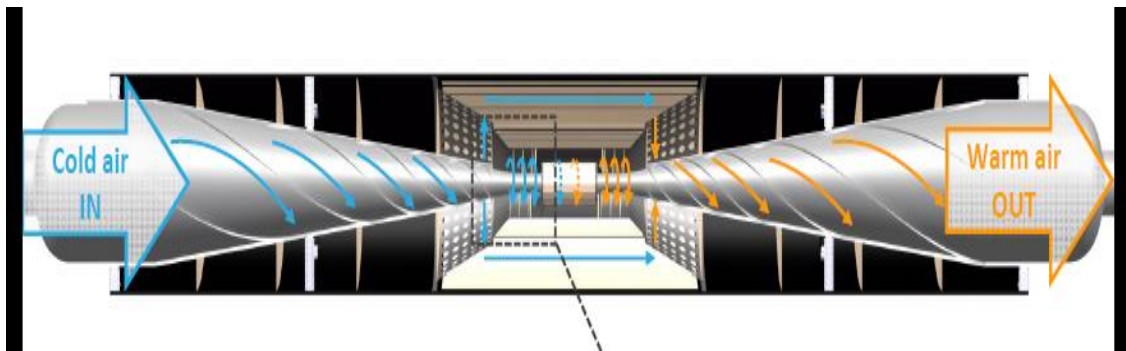


Figure 3: Forced air cooling of the inner barrel

We are currently researching lightweight stave prototypes (support structures). Many different tests were done to look at a variety of properties. Our stave supports are sandwiches of carbon fiber with a core of some material. Two main prototypes were tested each having a different core. The Rohacell type has a Styrofoam like core of a material called rohacell. The Nomex has a honeycomb shaped core made of nomex and carbone. Our test setup consisted of a glass box with a fan at one end. This acted as our wind chamber. The channel height of the box can also be adjusted to simulate conditions of the eventual barrel geometry. We can change the wind speed of the fan as well. A circular plate can be removed from the box in which the stave is attached. The orientation of this plate can be changed. This is to orient the stave to different flow directions. Another feature is that the box has several holes to insert a variety of sensors.





Figure 4: Nomex core



Figure 5: Rohacell core

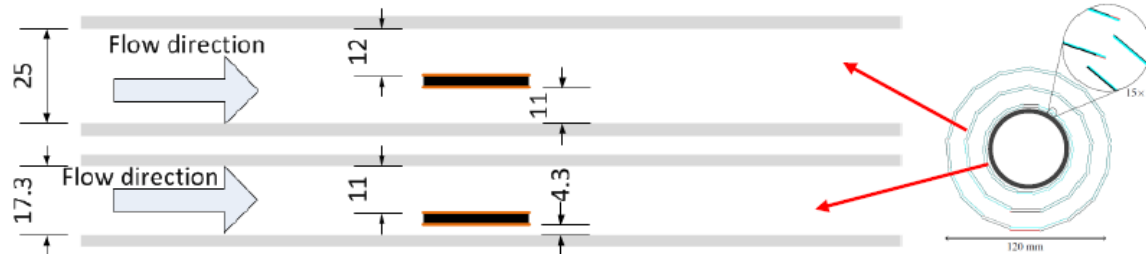


Figure 6: Thermal test setup

The first tests done were thermal tests. The reasons for these tests are to characterize the stave's properties under forced air cooling and to corroborate the results with finite element analysis simulations (FEA Simulations done in Ansys software). The stave is affixed with a highly resistive circuit to simulate the heat generated from the eventual pixel detectors. Small temperature sensors are also affixed to the stave as well as a sensor at both ends of the box. The fan is turned on and a current is applied to the circuit. We have four ammeters to measure the wind speed however only one is necessary for this setup. Tests were done to compare the sensors and all function regularly. One ammeter is placed before the stave in the chamber through a hole. The fan voltage is then changed until a desired speed. After we have a desired wind speed the ammeter is removed. If the ammeter were to stay in during the temperature measurements the air flow would change in ways not desired. The temperature is measured for three minutes and an average is taken. The temperature should remain constant over these three minutes. The temperature is measured through a labview program. The wind speed, the current, and the orientation of the stave are varied. The results are shown below:

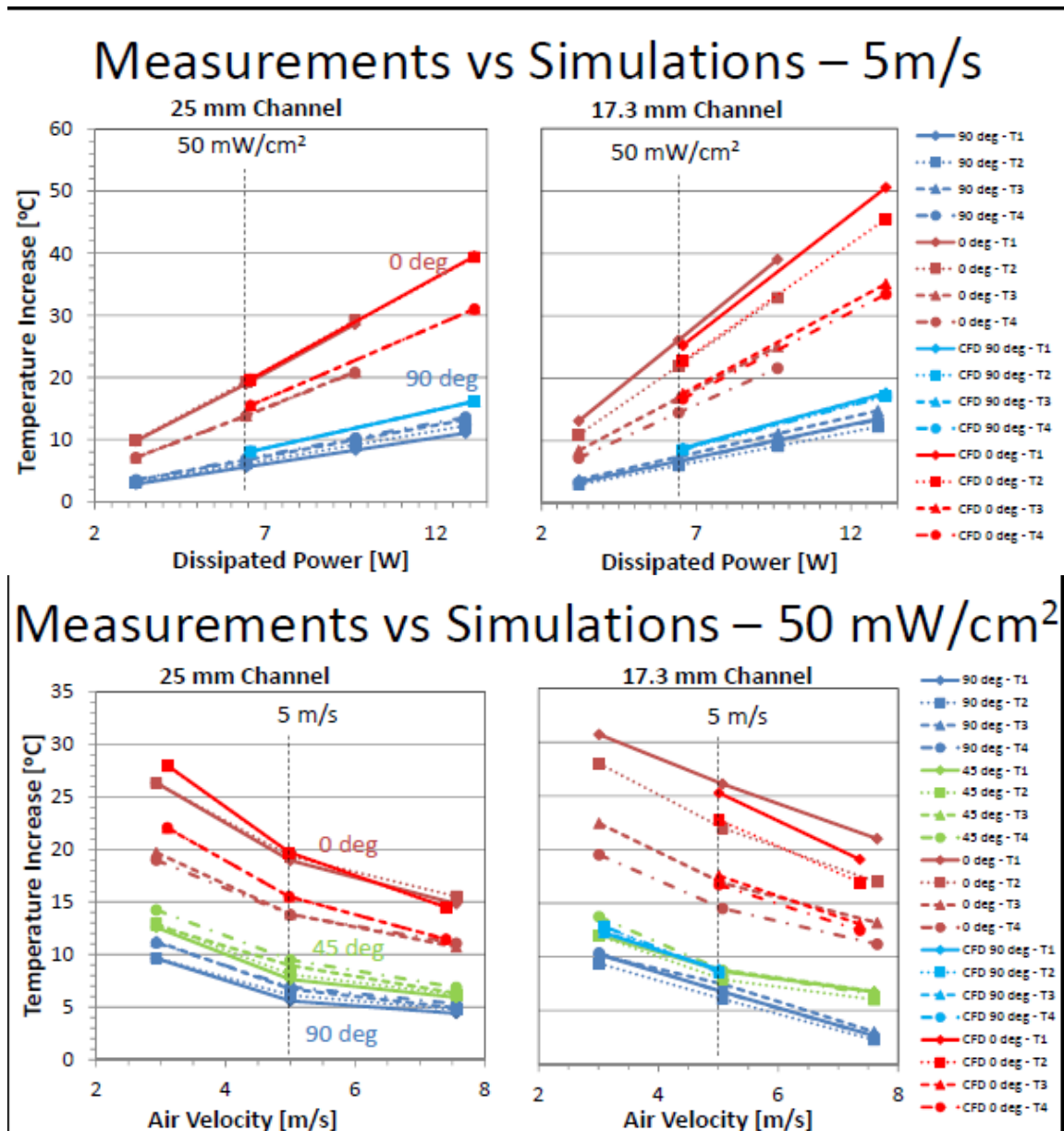


Figure 7: Results of thermal tests (CFD lines are the simulations)

As can be seen the simulated temperatures closely match the measured temperatures. It is good to validate the simulations because this means the methodology of the simulations seem to be correct. More complex geometries other than the ones we tested can be simulated with better confidence. Another result from the thermal tests is the similarity between the two types of staves:

# Nomex vs Rohacell core

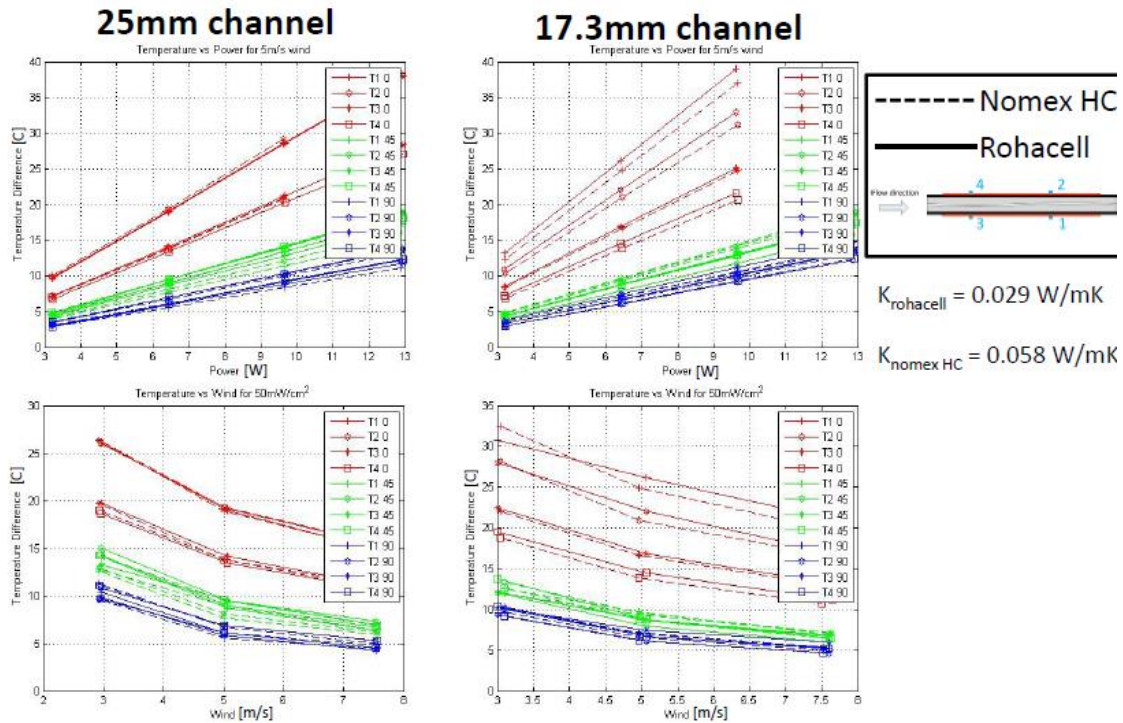


Figure 8: Nomex vs. Rohacell temperature properties

There is little difference between the two staves in all conditions. The temperatures are very similar for both cores. To get these graphs we did data analyses with custom Matlab scripts. The labview results were saved as excel files. These were then opened with Matlab to then average the temperature measurements over three minutes and then save the average temperature in a different summary file. This file was then graphed with Matlab to compare rohacell and nomex measurements.

After temperature measurements were made we moved on to vibration measurements. The reason we make vibration measurements is to try and find the natural frequencies and the resonant frequencies where stave is excited. We also want to find the RMS values of the amplitudes. We used a laser sensor to measure the vibrations of the stave. The sensor shoots a laser at the stave which is then reflected back. The sensor has a resolution of about .15 microns. The laser sensor is supported by a 3D printed plastic support. Measurements were made before along the length of the stave however there was a desire to measure across the width. At first the solution to this problem was to put a plate under the old support that allowed it to slide along the width. However screws could not be found short enough to accomplish this. The laser sensor only has a certain range in which it can measure limiting the plate's thickness. A new sensor support was to be designed. CATIA software was used to design the new part. CAD files of the setup were available to figure out necessary geometries and other information such as sensor distance to the stave. This allowed us to find problems with the part before we printed it.





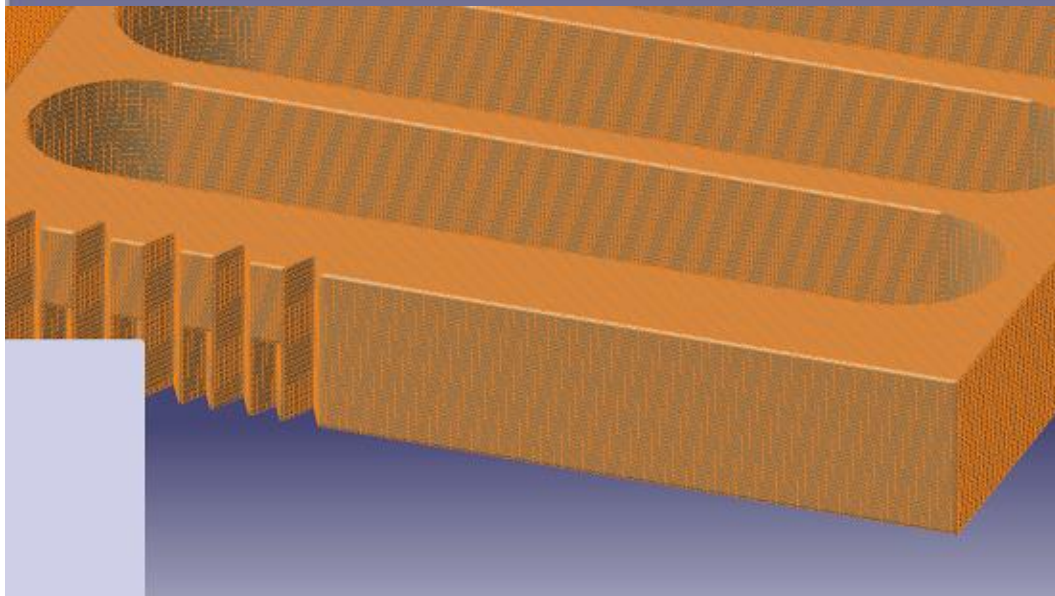
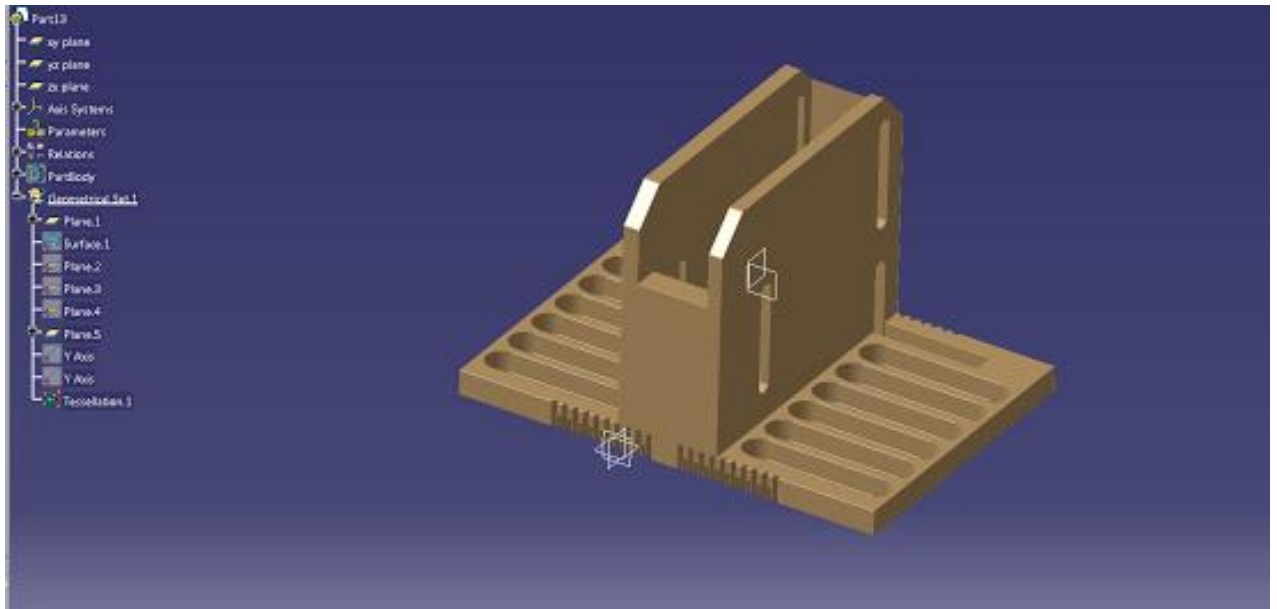


*Figure 10: Eventual laser support and tessellation of file*

Eventually the final design of the part was finalized. In order to 3D print it the file must be converted into a .stl file type. In order to do this the part in CATIA must be split up into many triangles. This is what an STL file is. From there the STL file is processed by software to split it into layers. This information is then given to the printer and it prints the part layer by layer. In order to prevent cantilever structures there is support material that dissolves away once the part is done. The location of this support material is also calculated by the printing software.

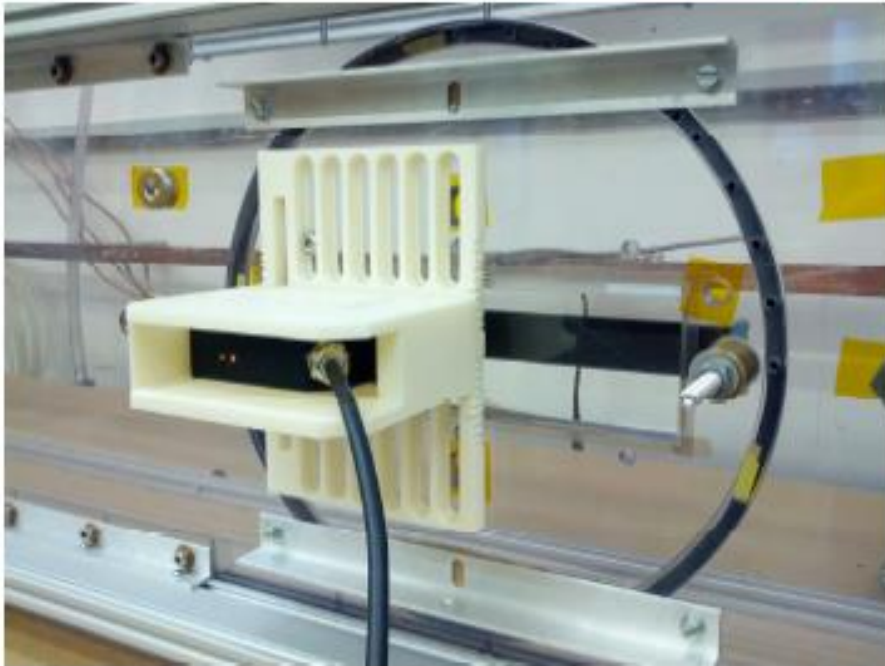
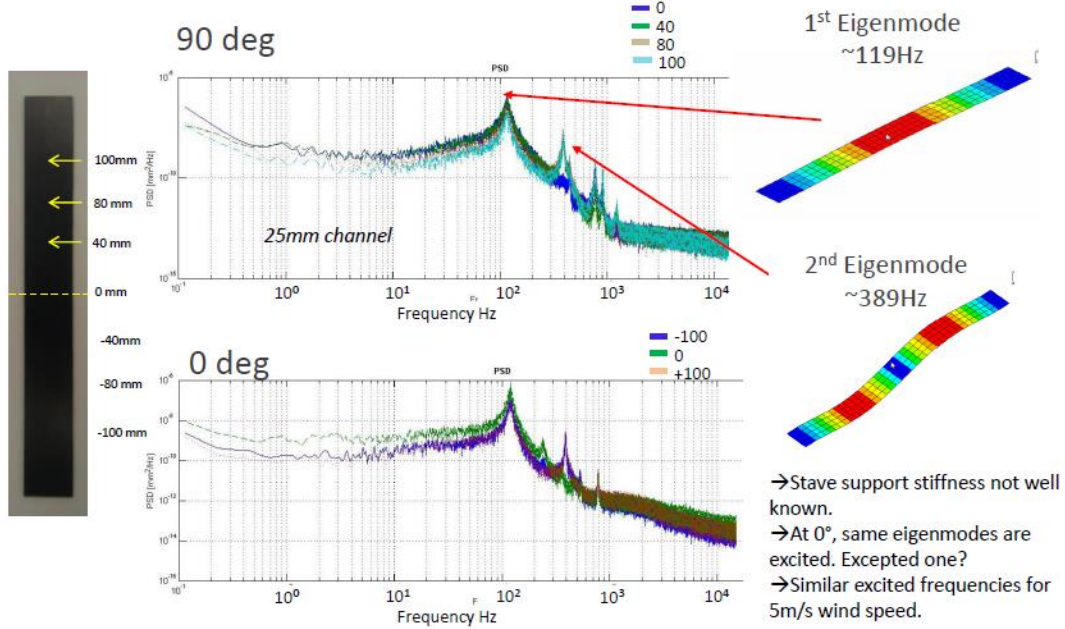


*Figure 11: Eventual 3D printed part and setup*

After the part was printed measurements began. The vibration test procedures were similar to the thermal tests'. We varied the wind speed, stave angle, and channel height. Measurements of thirty seconds were made at different intervals along the stave. The measurements are taken by software that arrived with the laser sensor. The time spectrum data is then saved as a .csv file. This file can then be analyzed with matlab scripts. To look at the frequency spectrum we took the Fourier transform of the file. It was then further cleaned up by finding the power spectral density. Instead of showing the types of frequencies present in the time domain a power spectral density shows the power distributed over the frequencies. From these graphs we could see the modes excited by the wind. The simulations showed similar frequencies to what we measured. Early on when we were making these measurements we were seeing very low frequencies being excited. They were too low to be from the stave. They were ultimately from the setup itself. At first the laser support was vibrating due to it being slightly cantilevered at some points along the stave. Eventually two aluminium bars were added to further fix the support. The low frequencies disappeared after this. However the small plastic supports that fix the stave to the plate is to be redesigned to further reduce unwanted vibrations.



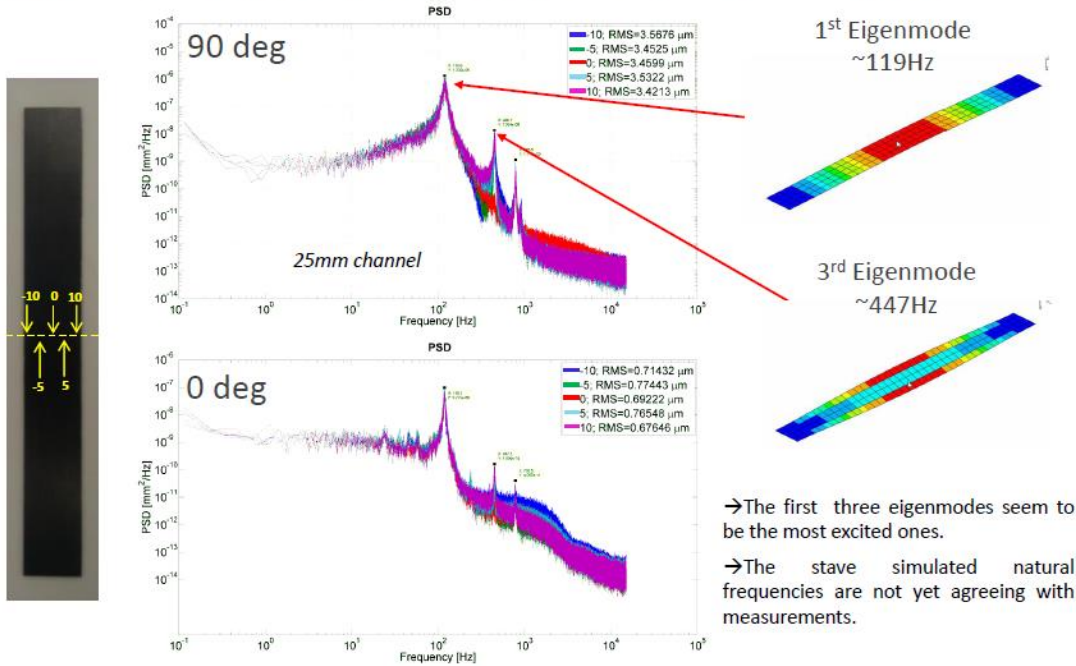
# Sweep along length (Nomex HC – 7.6m/s)



21



# Sweep along width (Nomex HC – 7.6m/s)



22

Figure 12: Power Spectral Density graphs along the length and width showing excited modes of vibrations

Besides the frequencies we also want to look at the RMS values of the amplitude. Using the time domain file we can use a matlab script to calculate this as well. The RMS graphs are then plotted comparing a variety of cases. The maximum RMS at the highest wind speed is about 3.5 microns. Air cooling of the inner barrel will be around 5m/s. At most the RMS here is about 2.5 microns. These amplitudes are acceptable.

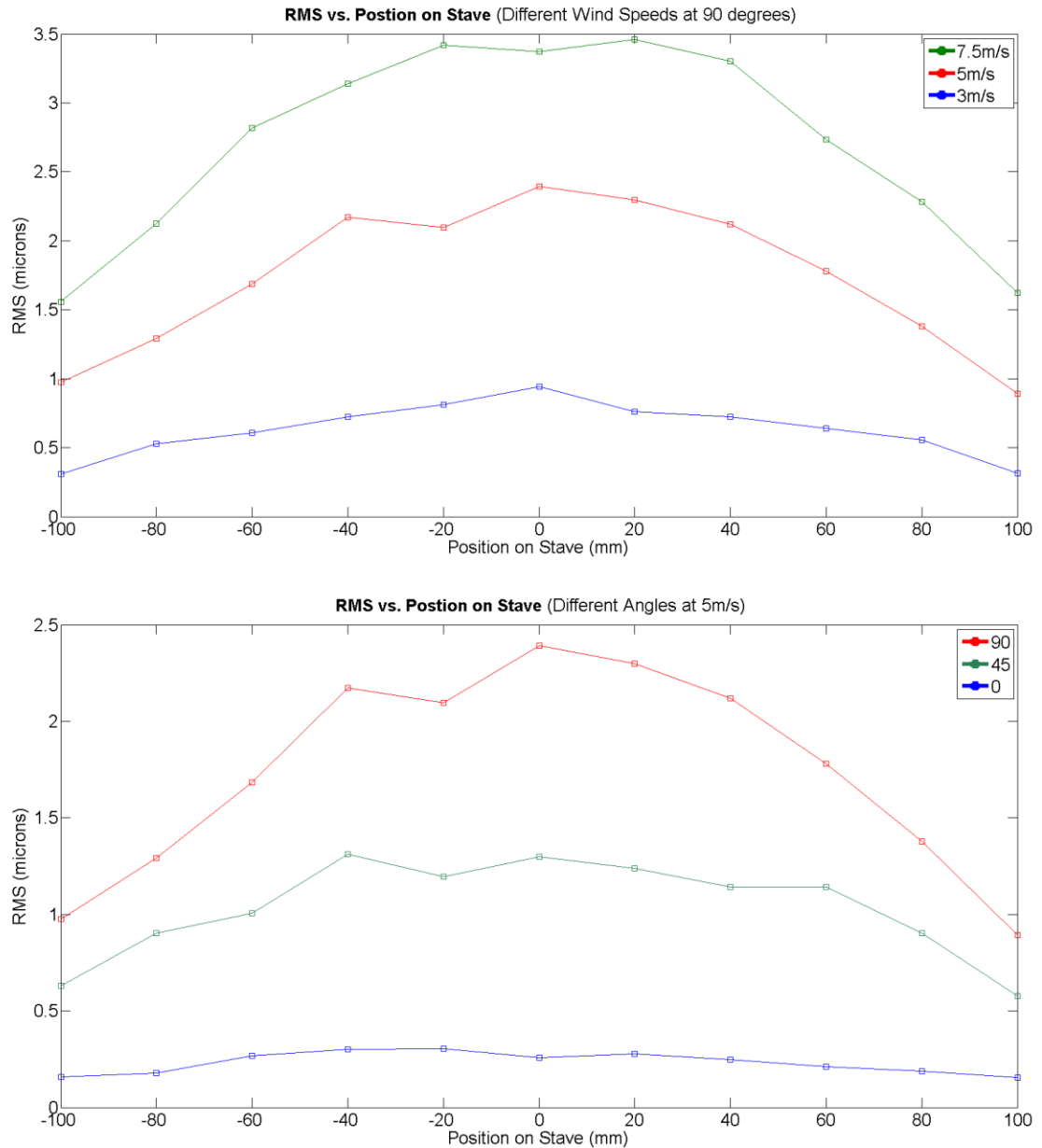


Figure 13: RMS graphs along the length of the stave

Currently new stave prototypes have arrived. These use higher modulus carbon fibers. Not only are these new prototypes lighter but they also should have lower RMS amplitudes due to the higher modulus fibers. Three point bending tests have already been done to try and find the flexural stiffness of the staves. The next tests to be made are radiation length tests. Currently we have a



Cd109 source (Cadmium 109). However in order to achieve a better certainty the current setup needs to be changed. As of now the source is too far from the x-ray counter. We are currently designing a part to be 3D printed.

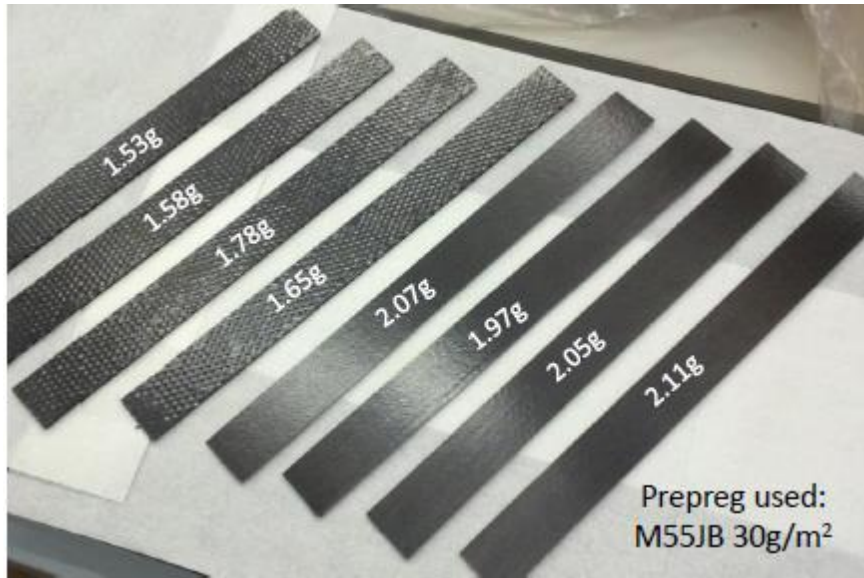


Figure 14: New stave prototypes

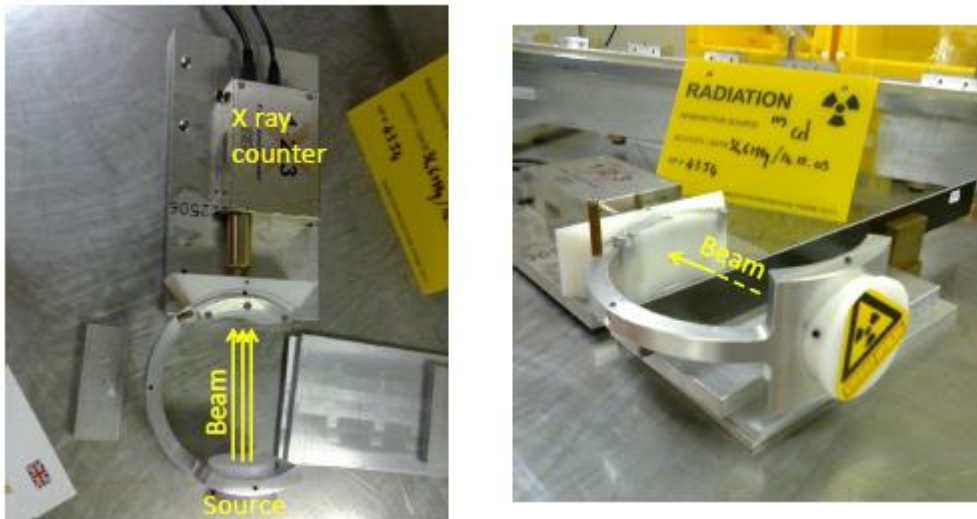


Figure 15: Current radiation length measurement setup

We will be repeating the vibration tests on the new prototypes. More thermal tests do not seem to be necessary at the moment as the behavior of the new prototypes should not have changed by much. Eventually a different wind chamber will be designed to further reflect the actual barrel geometry. Currently the staves are made by an outside company. There is further research in creating them at CERN.

## Works Cited

Linssen, Lucie. "CLIC Detector Studies." Web.

<<http://indico.cern.ch/event/301263/material/slides/0.pdf>>.

Nuiry, François - Xavier. "Optimisation Studies and Tests of Low - Mass Support Structures for the CLIC Vertex Detector." Web.

<[https://twiki.cern.ch/twiki/pub/CLIC/FTDM/Vertex\\_Nury.pdf](https://twiki.cern.ch/twiki/pub/CLIC/FTDM/Vertex_Nury.pdf)>.

Duarte Ramos, F., F.X. Nuiry, W. Klempt, and K. Spindelman. "Update on Mechanics and Cooling Studies." *Indico.cern.ch*. CERN, 24 Apr. 2014. Web. 5 May 2014.

<<https://indico.cern.ch/event/310253/contribution/0/material/slides/0.pdf>>.

